

An All-Digital Up-Conversion Architecture for Low Power Transmitters

Sirmayanti Sirmayanti

B.Eng (Telecommunications), M.Eng (Electrical and Electronics)

COLLEGE OF ENGINEERING AND SCIENCE
VICTORIA UNIVERSITY

SUBMITTED IN FULFILLMENT OF THE
REQUIREMENTS OF THE DEGREE OF
DOCTOR OF PHILOSOPHY

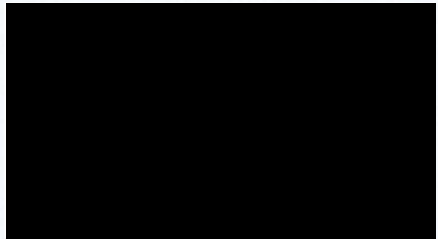
JULY 2014

**© Copyright by Sirmayanti 2014
All Rights Reserved**

To my family.

Doctor of Philosophy Declaration

“I, Sirmayanti Sirmayanti, declare that the PhD thesis entitled ‘An all-digital up-conversion architecture for low power transmitters’ is no more than 100,000 words in lengths including quotes and exclusive of tables, figures, appendices, bibliography, references and footnotes. This thesis contains no material that has been submitted previously, in whole or in part, for the award of any other academic degree or diploma. Except where otherwise indicated, this thesis is my own work.”



Sirmayanti Sirmayanti
Date: July, 2014

Abstract

A sigma-delta ($\Sigma\Delta$) based technique is used to embed a complex modulation scheme such as orthogonal frequency division multiplexing (OFDM) into a single ON-OFF bit stream operating at the carrier frequency. The amplitude of the signal is related to the pulse widths and the phase is related to the pulse positions. The pulse edges are time quantised to align with the system clock. The work is based on a Cartesian $\Sigma\Delta$ scheme which uses Cartesian filters and a polar quantiser to move quantisation noise away from the band of interest.

The first contribution of this thesis is the introduction of an improved odd quantisation and joint quantisation process. Odd quantisation uses pulse widths constrained to an odd number of clock periods compared to the more traditional even quantisation with an even number of clock periods. Joint quantisation uses pulses of unrestricted widths. It is shown that the odd quantisation scheme outperforms the even quantisation scheme by about 2 dB in terms of signal-to-noise ratio and the joint quantisation scheme enhances this by a further 3 dB. The improvement comes at the expense of complexity. A joint quantiser requires a two dimensional (2D) quantisation process, which for an oversampling ratio (OSR_{RF}) of 8 involves 197 operations. A method that simplifies this to 44 operations is proposed.

The second contribution involves the development of a new frequency tuning method. It involves phase rotators before and after the quantiser rotating at an intermediate frequency. Tuning spectrally shifts both the signal and noise null together, but the final phase conversion process generates an image and distortion products of both the noise and signal, resulting in a higher than expected noise floor and unwanted spurious signals. A deliberate choice of intermediate frequency (f_{IF}) equal to or greater than the transmission bandwidth plus half of a channel bandwidth, will move all distortion products out of band. Unfortunately there is a deterioration in the in-band noise null compared to the non-shifted condition of about 8 dB and this worsens as the intermediate frequency increases.

A mathematical derivation has been developed to predict the size and position of the unwanted images. The signal image can be removed by pre-distorting the input signal. A method for reducing noise enhancement caused by frequency tuning has also been developed. It involves distorting the feedback signal in the $\Sigma\Delta$ converter. The above improvements will enhance the use of all-digital $\Sigma\Delta$ based transmitters in future wireless communication system.

Acknowledgements

In the name of Allah SWT, Most Gracious, Most Merciful.

The first most grateful acknowledgement I say to Allah SWT. I could never have finished this thesis without His guidance, help, and blessing.

This thesis would not be completed without support and guidance from those to whom I deliver these acknowledgements.

I express my greatest gratitude to Prof Mike Faulkner for the amazing supervisory process and his incredible patience in dealing with my research work, his ideas, guidance and knowledge support over the years.

I am also deeply grateful to Dr Horace King for his critique and feedback that meant forcing my progress with great improvement. I also appreciate the big support from Dr Vandana Bassoo for a great mentor and with her valuable knowledge in the relation to the concept.

I would like to thank past CTME and current TEPS post-docs including Dr Ajay Tikka and Dr Shabbir Ahmed for their advice during of this work. I am thankful to the administrative staff, namely, Shukonya Benka.

Moreover, I would also like to express my gratitude to the fantastic ladies at the Postgraduate Research Officer and the Student Advice Officer (Research & Graduates Studies) particularly Liz Smith, Lesley Birch, Sue and Davies. A big thank you to all staff

from International Student Officer especially Sue Oulton and the most patience assistance from English Learning Support (ELS) particularly from Angela Rojter.

I would like to many thank all my past CTME and present TEPS colleagues. They made my PhD journey at Victoria University a very exciting and entertaining one. Daily tea-time and lunch break have always been a loud and happy occasion. So a big thank you to Hafizah, Hojjat, Nithila, Geordie, Behailu, Robabeh, Reheleh, Reza, Poonhe, Marziyeh, Badra, Sara, Lance, Shahryar, Rizwan, Mustafa, Waqas, and Venkat.

I am grateful to my friends and neighbours in ‘kampung Indonesia’ Footscray, all friends in ‘Komunitas Anging Mammiri’, and all Victoria University Indonesian Student Association VUISAers for all the sharing of the experiences with full of laughter and happiness.

My great appreciation goes to the Indonesian government and Direktorat Jenderal Pendidikan Tinggi (DIKTI) which provided a scholarship for me to study and learn about a different academic environment overseas. I would like to many thank the Director and staff of the State Polytechnic of Ujung Pandang.

Finally, I would like to thank my family. I am very blessed to have such a fantastic support. I wish to express my heartfelt gratitude to my husband Nur Adil and my beloved kids Siti Uswatun Hasanah, Muhammad Aqilralia Adil, and Ahmad Faqih Khairy Adil. I am grateful to my sisters Sri Anita and Fitriahwanti for their encouragement. Lastly, I would like to thank both my parents, Drs. H. Siradjuddin AK and Dra. Hj. Marlaela Syam, for their endless love and prayers for their encouragements and for being inspiring role-models.

Thank you so much for all your support.

Contents

Doctor of Philosophy Declaration	v
Abstract	vii
Acknowledgements.....	viii
Contents.....	x
List of Figures	xiv
List of Tables.....	xix
List of Abbreviations.....	xx
List of Symbols	xxiii
1 Introduction	1
1.1 Indoor Wireless Transmitter	3
1.2 All-Digital Wireless Transmitter	4
1.3 Wireless Transmitter Challenges	6
1.4 Research Objective	9
1.5 Thesis Contribution.....	9
1.6 List of Publications	10
1.7 Thesis Organisation	11
2 Literature Review.....	13
2.1 Introduction.....	13
2.2 Traditional PAs Architecture	14
2.2.1 Non-switching Amplifiers	14

2.2.2	The Doherty PA Architecture.....	15
2.2.3	Envelope Elimination and Restoration (EER) and Envelope Tracking (ET)	16
2.3	Switched-Mode RF Power Amplifiers (RF-SMPAs)	17
2.3.1	Class-D Amplifier	18
2.3.2	Class-S Amplifier	19
2.3.3	Class-E Amplifier	20
2.3.4	Class-F Amplifier	21
2.3.5	Bridge Structure.....	21
2.4	$\Sigma\Delta$ Modulators	22
2.4.1	Basic $\Sigma\Delta$ Modulation.....	22
2.4.2	Linear $\Sigma\Delta$ Modulator Model.....	24
2.4.3	Signal Transfer Function (STF) and Noise Transfer Function (NTF)	25
2.4.4	NTF Low-pass $\Sigma\Delta$ Modulator: Poles and Zeros.....	29
2.4.5	Band-pass $\Sigma\Delta$ Modulator.....	32
2.5	Interpolation and Decimation for $\Sigma\Delta$ Modulators.....	33
2.6	Coding Efficiency	35
2.7	Modulation Techniques for Switched PA's	36
2.7.1	Burst-Mode Modulation	36
2.7.2	Cycle-Mode Modulation	38
2.8	$\Sigma\Delta$ Modulator Architecture.....	40
2.8.1	Band-pass $\Sigma\Delta$ Architecture.....	41
2.8.2	Polar $\Sigma\Delta$ Architecture	44
2.8.3	Cartesian $\Sigma\Delta$ Architecture	47
2.9	RF Tuning	50
2.10	Summary	51
3	Proposed Polar Quantisation Scheme	52
3.1	Introduction.....	52
3.2	Cartesian $\Sigma\Delta$ upconverters	54
3.3	Odd Quantisation and Even Quantisation.....	57
3.3.1	Polar to PWM/PPM Block	65

3.3.2 Complexity, Sample Rate and Bandwidth.....	67
3.4 Joint Quantisation Scheme.....	68
3.4.1 Exhaustive Search	69
3.4.2 Combined Odd+Even Search	70
3.4.3 Complexity Comparison.....	72
3.5 Baseband RF Tuning.....	72
3.6 Simulation Results	73
3.6.1 Spectrum Analysis with SSB signal	73
3.6.2 Spectrum Analysis with OFDM input signal	77
3.6.2.1 Comparison of Joint, Odd, and Even Quantisation Noise Level.....	79
3.6.2.2 Adjacent Channel Powers (ACPs) Characteristics of Odd quantisation and Even quantisation	80
3.7 Experimental Setup and Measurement Results.....	83
3.8 Summary	86
4 Proposed Baseband and IF Tuning	88
4.1 Introduction.....	88
4.2 Baseband Tuning for $\Sigma\Delta$ Upconverter	89
4.3 Interference Distortion	91
4.4 Spurious Removal using IF Tuning	92
4.5 Summary	96
5 Proposed Image and Noise Cancellation.....	97
5.1 Introduction.....	97
5.2 Unwanted Spectral Components.....	98
5.3 Mathematical Analysis of Harmonic Distortion.....	101
5.3.1 The Reference Carrier Signal $\tilde{S}_k(f)$	105
5.3.2 The Gate Signal $\tilde{G}_k(f)$	106
5.3.3 The Convolution of $\tilde{S}_k(f)$ and $\tilde{G}_k(f)$	108
5.4 Image Cancellation in a Multi-carrier Environment.....	114
5.4.1 Derivation of Pre-distortion Coefficients	116

5.4.2 Simulation Results.....	117
5.4.2.1 Image Cancellation for Baseband Tuning.....	117
5.4.3.2 Image Cancellation for IF Tuning.....	118
5.4.3 Measurement Results.....	121
5.5 Noise Cancellation in a Multi-carrier Environment.....	123
5.5.1 Simulation Results.....	126
5.5.2 Measurement Results.....	128
5.5.3 Correction at Higher OSR	129
5.6 Summary	130
6 Conclusion and Further Research.....	132
6.1 Conclusion	132
6.2 Further Research	134
6.2.1 Third Harmonic Cancellation	134
6.2.2 FPGA Implementation.....	135
6.2.3 Increased Power Outputs.....	135
References	136

List of Figures

Figure		Page
1.1	The mobile network capacity gap keeps widening with minimal anticipated increases in spectrum and efficiency [3]	2
1.2	Sigma-Delta ($\Sigma\Delta$) structure can potentially replace the analog components of the traditional wireless architecture (top). A potential future wireless transmitter architecture (bottom)	5
1.3	PWM/PPM RF signal is generated from the polar baseband signal.....	8
2.1	An envelope elimination and restoration (EER) architecture. The envelope tracking (ET) architecture is similar with the EER but without <i>limiter</i>	16
2.2	(a) Voltage-mode [50] and (b) current-mode [48] of a Class-D PA	18
2.3	Schematic of Class-S PA [36, 55]	19
2.4	Schematic of a Class-E PA	20
2.5	Generation of a three-level waveform with bridge structure	21
2.6	(a) 1 st order $\Sigma\Delta$ modulator (MOD1) and (b) quantisation noise power spectral density vs. frequency for conventional and $\Sigma\Delta$ converters. f_s is the $\Sigma\Delta$ sample rate [31]	22
2.7	A $\Sigma\Delta$ modulator as an A/D converter (top) and D/A converter (bottom) ...	23
2.8	Linear z -domain of $\Sigma\Delta$ modulator (MOD1) of Figure 2.5(a) structure.....	24
2.9	Linear model in z -domain of the <i>basic</i> MOD1 (top) and MOD2 (bottom) ..	26
2.10	NTF for MOD1 and MOD2	28
2.11	(a) The NTF poles MOD1 and (b) the NTF poles MOD1 based on the <i>Lee criterion</i>	30

2.12	The <i>Lee criterion</i> based MOD1 $\Sigma\Delta$ modulator	31
2.13	A linear z -domain of a band-pass $\Sigma\Delta$ modulator	32
2.14	Poles-zeros diagram in z -plane of the (a) NTF of low-pass MOD1 and (b) band-pass MOD1	33
2.15	Interpolation system (left) and decimation system (right) [62]	34
2.16	Coding efficiency measurement for band-pass $\Sigma\Delta$ modulator with class-D amplifier [71]	35
2.17	Burst-mode operation [72]	37
2.18	PWM of RF carrier, with supply modulation included (circle) [29].....	39
2.19	Band-pass $\Sigma\Delta$ architecture in [78].....	41
2.20	BPF for RF PWM/PPM output.....	41
2.21	The band-pass $\Sigma\Delta$ (2 nd order) architecture proposed in [81].....	42
2.22	The band-pass $\Sigma\Delta$ (two low-pass $\Sigma\Delta$ s) architecture proposed in [61].....	43
2.23	The polar $\Sigma\Delta$ based burst-mode architecture proposed in [77].....	44
2.24	The polar $\Sigma\Delta$ architecture proposed in [86].....	45
2.25	Polar $\Sigma\Delta$ Architecture proposed in [87].....	46
2.26	(a) Normalized spectrum of OFDM and (b) ACP for Cartesian $\Sigma\Delta$ and polar $\Sigma\Delta$ modulator [76].....	48
2.27	Cartesian $\Sigma\Delta$ Architecture [79]. $\Sigma\Delta$ filtering is in Cartesian with quantisation in polar.....	49
2.28	SSB output spectrum from a Cartesian $\Sigma\Delta$ with the distortions from the PWM/PPM with image and 3 rd harmonic (right) [79], and the conjugate quantisation noise folding in the frequency domain (left) [90]	50
3.1	Cartesian $\Sigma\Delta$ with polar quantisation showing signals at different points. The two quantised sinusoidal amplitudes and pulse widths are shown top right	55
3.2	The PWM/PPM output for $OSR_{RF} = 8$. Note, a two level signal version would set the negative pulses to zero.....	56
3.3	Quantised amplitude of the RC carrier $\hat{v}_r(\alpha)$ for even and odd pulse widths ($OSR_{RF} = 8$). α_E, α_o define the pulse width and p_p defines the pulse	

position.....	58
3.4 The polar quantisation points in the I - Q plane, ‘even’ (top) and ‘odd’ (bottom), $OSR_{RF} = 8$, $N_{A_{even}} = N_{A_{odd}} = 3$, $N_P = 8$	61
3.5 Quantisation steps used by Q_R , (Figure 3.1), $OSR_{RF}=8$	65
3.6 Odd PWM generation, $OSR_{RF} = 8$	66
3.7 Phase plane for optimum joint odd-even quantisation ($OSR_{RF} = 8$).....	69
3.8 Proposed reduced complexity quantiser using separate odd and even quantisers followed by a minimum error selection. An example $OSR_{RF} = 8$ of joint polar plane is described.....	70
3.9 The input baseband signal is offset by $\exp(j\omega_{offset}n)$	73
3.10 Output spectrum of ‘Polar to PWM/PPM’ block, $OSR_{RF} = 32$	74
3.11 Zoom-in of sizes of unwanted signals against 64 MHz of offset frequency ($f_c=1024$ MHz, $OSR_{RF} = 32$), dB relative to carrier.....	75
3.12 The I - Q signal OFDM input to Cartesian $\Sigma\Delta$ upconverters with an offset carrier of N_{offset} frequency bins.....	78
3.13 An offset OFDM signal with 10 MHz bandwidth, $OSR_{RF} = 32$. ‘Odd’, ‘even’, and ‘joint’ quantisation are compared.....	80
3.14 Spectrum of odd quantisation and even quantisation with offset OFDM signal ($OSR_{RF}= 32$, $f_c=1024$ MHz, and offset=20 MHz/Channel)	81
3.15 Cartesian $\Sigma\Delta$ with the odd quantisation and even quantisation schemes (ACP in adjacent channel versus input signal-to-noise level). $OSR_{RF}=32$, $f_c=1024$ MHz, and offset=20 MHz/Channel.....	82
3.16 Experimental setup for measurement.....	84
3.17 Measurement result. The comparison of joint vs. odd quantisation schemes (left) and joint vs. even quantisation scheme (right), $OSR_{RF} = 32$.	86
4.1 Cartesian $\Sigma\Delta$ scheme, joint quantisation is applied for baseband tuning scenario.....	90
4.2 Simulated output spectrum for different channel position. $OSR_{RF}= 32$, Quantisation = ‘joint’.....	92
4.3 Simulated output spectrum at $f_{IF} = 75$ MHz. The distortion products are	

	moved away from the band of interest and would be filtered out by the RF band-pass filter. $OSR_{RF}= 32$, Quantisation = ‘joint’	94
4.4	Proposed Cartesian $\Sigma\Delta$ upconverters with applied phase rotation & derotation in Cartesian format	95
4.5	Proposed Cartesian $\Sigma\Delta$ upconverters with applied phase rotation & derotation in Polar format	95
5.1	Phase shift waveform when the pulse change in a position [79].....	99
5.2	Phase shifted oscillators generate a SSB signal [79]	101
5.3	SSB generation for mathematical analysis [79]	103
5.4	The gate signal generation. (a) in time domain, (b) in frequency domain, (i) input signal, (ii) sampling function, (iii) sample image, (iv) $\tilde{G}_0(f)$ output signal.....	107
5.5	The convolution of $\tilde{S}_k(f)$ and $\tilde{G}_k(f)$ gives $\tilde{Y}_k(f)$. $\tilde{S}_k(f)$, (b) zoom of $\tilde{S}_k(f)$ with $OSR_{RF}= 8$ and $\alpha = 2$, (c) Summation of $\tilde{G}_k(f - nfc)$ that form $\tilde{Y}(f)$	109
5.6	The proposed Cartesian $\Sigma\Delta$ architecture with the pre-distortion (top) and the pre-distortion coefficients for image cancellation (bottom).....	115
5.7	Image cancellation using baseband tuning with $OSR_{RF}= 16$. (a) Spectrum at the pre-distortion unit. (b) Spectrum at $V_{IQ}(f)$, $\hat{V}_{R\theta}(f)$ and $W(f)$	118
5.8	Pre-distortion for IF tuned Cartesian $\Sigma\Delta$ architecture (top). The pre-distorter architecture for image cancellation (bottom).....	119
5.9	Spectrum at the pre-distortion unit for IF tuning with $OSR_{RF}= 16$. Three different f_{offset} and f_{IF} scenarios are compared.....	120
5.10	Image Cancellation for IF tuning with $OSR_{RF}= 16$. The three different f_{offset} and f_{IF} scenarios are shown for comparison.....	121
5.11	The desired signal (USB) and the image (LSB). Image cancellation, before (left) and after (right). $f_{offset} = 30$, $OSR_{RF}= 16$	122
5.12	The desired signal (LSB) and the image (USB). Image cancellation, before (left) and after (right). $f_{offset} = -30$, $OSR_{RF}= 16$	122
5.13	Noise floor problem around the band of interest for $OSR_{RF}= 4$	124

5.14	The proposed IF tuning with the post -distortion (top) and the post-distortion coefficients for noise cancellation (bottom).....	125
5.15	Noise cancellation for IF tuning for $OSR_{RF}=4$.The original spectrum before noise cancellation (left) and the spectrum after noise cancellation (right). The image is increased when the noise floor is cancelled (right black)	126
5.16	Image and Noise cancellation for IF tuning. Post-distortion for noise cancellation and pre-distortion for image cancellation.....	127
5.17	Spectrum of the image and noise cancellation for $OSR_{RF}=4$	128
5.18	Measurement results of noise cancellation for IF tuning. $OSR_{RF} = 4$. The marker is at the nominal carrier frequency, f_c	129
5.19	The spectrum with after and before noise cancellation (NC) for $OSR_{RF}= 8$	130

List of Tables

Table		Page
3.1	Values of quantised amplitude, \hat{v}_r , for different OSR_{RF} and pulse width (α_E or α_o). There are OSR_{RF} clock periods in one cycle of the nominal RF carrier.....	63
3.2	The number of arithmetic operations to implement the quantiser.....	71
3.3	Simulation parameters for spectrum analysis with SSB signal.....	74
3.4	Comparison of the SNR for odd quantisation and even quantisation schemes.....	76
3.5	Simulation parameters for OFDM signal.....	79
3.6	Parameter set for AWG input.....	85
5.1	Comparison between simulation and calculation of the harmonics size. ($K = 1$, $f_{ssb} = 64$ MHz, $OSR_{RF} = 32$, $f_c = 1024$ MHz).....	113

List of Abbreviations

$\Sigma\Delta$	Sigma-Delta
1D	One dimension
2D	Two dimension
3G	3 rd Generation
4G	4 th Generation
5G	5 th Generation
ACP	Adjacent Channel Power
A/D	Analog-to-Digital
ADC	Analog-to-Digital Converter
AM	Amplitude Modulation
ALTE	Advanced Long Term Evolution
ASIC	Application Specific Integrated Circuit
AWG	Arbitrary Waveform Generator
BB	Baseband
BPF	Band-pass Filter
BS	Base Station
C2P	Cartesian-to-Polar
CD	Compact Disc
CDMA	Code Division Multiple Access
CMOS	Complementary Metal Oxide Semiconductor
D/A	Digital-to-analog
DAC	Digital-to-Analog Converter
DB	Decibel

DC	Direct Current
DSL	Digital Subscriber Line
DSP	Digital Signal Processing
DTG	Data Timing Generator
EER	Envelope Elimination and Restoration
ET	Envelope Trucking
EVM	Error Vector magnitude
FIR	Finite Impulse Response
FPGA	Field-Programmable Gate Array
GaN	<i>Gallium Nitride</i>
GHz	Gigahertz
IF	Intermediate Frequency
IIR	Infinite Impulse Response
LO	Local Oscillator
LPF	Low-pass Filter
LSB	Lower Side Band
LUT	Look-up-table
LTE	Long Term Evolution
MHz	Megahertz
MOD1	First-order Modulator
MOD2	Second-order Modulator
MQAM	M-ary Quadrature Amplitude Modulation
NTF	Noise Transfer Function
OFDM	Orthogonal Frequency Division Multiplexing
OSR	Oversampling ratio
P2C	Polar-to-Cartesian
PA	Power Amplifier
PAPR	Peak-to-Average Power Ratio
PM	Phase Modulation
PPM	Pulse Position Modulation

PSD	Power Spectral Density
PWM	Pulse Width Modulation
QPSK	Quadrature Phase Shift Keying
RBS	Radio Base Station
RF	Radio Frequency
RMS	Root Mean Square
SDR	Software-defined Radio
SMPA	Switch Mode Power Amplifier
SSB	Single Side Band
STF	Signal Transfer Function
USB	Upper Side Band
VCO	Voltage-Controlled Oscillator
WCDMA	Wideband Code Division Multiple Access
WLAN	Wireless Local Area Network

List of Symbols

$()^*$	Complex conjugate
\otimes	Convolution
α	Pulse width in number of clock periods
α_E	Pulse width in even number of clock periods
α_O	Pulse width in odd number of clock periods
γ	Amplitude of pulse waveform
$a, a', b, b', c, c', d, d'$	Notation for the pre-distortion transfer point
A	Active tone OFDM
$A(f)$	Spectrum of conjugated input signal $U(f)$ at point a
$A'(f)$	Spectrum of the delay conjugated input signal $U(f)$ at point a'
b	Bin number in FFT
$B(f)$	Spectrum of rotated input signal $U(f)$ at point b
$B'(f)$	Spectrum of derotated input signal $U(f)$ at point b'
B_{ofdm}	OFDM bandwidth

B_w	Signal bandwidth
BW_b	Bandwidth baseband
BW_{ch}	Bandwidth channel
$C(f)$	Spectrum of the conjugated input signal $U(f)$ after rotation at point c
$C'(f)$	Spectrum of the conjugated input signal $U(f)$ before rotation at point c'
δ	Rotation frequency
$-\delta$	Derotation frequency
δ_b	Duty cycle in Burst-mode
D	Data information
$D(f)$	Spectrum of the quantised conjugated input signal $U(f)$ at point d
$D'(f)$	Spectrum of the delay quantised conjugated input signal $U(f)$ at point d'
Δf	Bin frequency space between the active tone of subcarrier
F	Fourier transfer
F^{-1}	Inverse Fourier transfer
f_b	Burst repetition frequency
f_B	Maximum signal bandwidth
f_c	Carrier frequency
f_{clock}	System digital clock frequency
f_{IF}	Intermediate frequency

f_{offset}	Offset frequency
f_s	Sample rate of $\Sigma\Delta$ filter
f_{ssb}	Frequency of single side band tone
g_1	Feedback loop gain on the pre-distortion transfer function unit
g_2	Delay gain on the pre-distortion transfer function unit
$g_k(t)$	Signal output from the phase gate
$\tilde{G}_k(f)$	Spectrum of gate signal
i	Positive integer
\hat{I}	Cartesian in-phase feedback to $\Sigma\Delta$ filters
I	In-phase of amplitude component of the Cartesian $\Sigma\Delta$ filtered signal
k	Number of delay periods
K	Number of updated carrier periods between each output sample of $\Sigma\Delta$ modulator
L_θ	Threshold for quantised phase
L_R	Threshold for quantised amplitude
nL_θ	Number of threshold levels for quantised phase
nL_R	Number of threshold levels for quantised amplitude
n	Sample number in f_c
N	Number of subcarriers of the channel bandwidth
N_A	Number of amplitude and pulse width quantisation levels
$N_{A_{even}}$	Amplitude quantisation levels in even number of clock periods

$N_{A_{odd}}$	Amplitude quantisation levels in odd number of clock periods
N_{FFT}	FFT size
N_{offset}	The offset frequency measured in bin frequencies
N_p	Number of phase increments & pulse position quantisation levels
$N_{Q_{even}}$	Number of quantisation points of even-quantisation
$N_{Q_{odd}}$	Number of quantisation points of odd-quantisation
$N_{Q_{joint}}$	Number of quantisation points of joint odd-even quantisation
m	Sample number in f_{ssb}
OSR_{BB}	Oversampling ratio of the baseband
OSR_{RF}	Oversampling ratio of $\Sigma\Delta$ filters
p	Sample number of f_s
P	Quantisation point
p_p	Pulse position delay in clock periods
$Q(\cdot)$	Quantisation function
Q	Quadrature of phase component of the Cartesian $\Sigma\Delta$ filtered signal
\hat{Q}	Cartesian quadrature feedback to $\Sigma\Delta$ filters
Q_E	Even quantisation co-ordinate
Q_O	Odd quantisation co-ordinate
Q_θ	Phase quantisation block
Q_R	Amplitude quantisation block

r	Maximum distance at the unit circle z -plane
R	Amplitude component of the Polar $\Sigma\Delta$ filtered signal
\hat{R}	Quantised Amplitude
\hat{R}_{PW1}	The first pulse width range of the quantised amplitude
\hat{R}_{PW2}	The second pulse width range of the quantised amplitude
s	Input baseband signal
s_i	Cartesian in-phase of input baseband signal
s_q	Cartesian quadrature of input baseband signal
$s_k(t)$	Signal output from the phase shifted oscillators
$\tilde{s}_k(f)$	Spectrum of oscillator signals
θ	Phase component of the Polar $\Sigma\Delta$ filtered signal
$\hat{\theta}$	Quantised Phase
θ_{ref}	Phase reference
$\Delta\theta$	Quantisation step size
T_b	ON period time in Burst-mode
T_c	Time period carrier
T_{clk}	Time period digital clock
T_{on}	The ON time period
T_{ssb}	Time period of the single side band tone
T_g	Time period of the pulse train

u	Input signal to $\Sigma\Delta$ filters or output of Frequency offset
u_i	Cartesian in-phase of input signal Cartesian $\Sigma\Delta$ upconverter
u_i'	Cartesian in-phase of input pre-distorted signal Cartesian $\Sigma\Delta$ upconverter
u_q	Cartesian quadrature of input signal Cartesian $\Sigma\Delta$ upconverter
u_q'	Cartesian quadrature of input pre-distorted signal Cartesian $\Sigma\Delta$ upconverter
u_{rms}	Input signal of the true RMS value
v_θ	Phase component of the Polar $\Sigma\Delta$ filtered signal
\hat{v}_θ	Quantised phase in Polar co-ordinate
\hat{v}_{θ_o}	Quantised phase in Polar co-ordinate for odd-quantisation
\hat{v}_{θ_e}	Quantised phase in Polar co-ordinate for even-quantisation
v_i	Cartesian in-phase component of $\Sigma\Delta$ filter output
\hat{v}_i	Cartesian in-phase feedback to $\Sigma\Delta$ filters
\hat{v}_{i_e}	Cartesian in-phase feedback to $\Sigma\Delta$ filters for even-quantisation
\hat{v}_{i_o}	Cartesian in-phase feedback to $\Sigma\Delta$ filters for odd-quantisation
v_q	Cartesian quadrature component of output $\Sigma\Delta$ filters
\hat{v}_q	Cartesian quadrature feedback to $\Sigma\Delta$ filters
\hat{v}_{q_o}	Cartesian quadrature feedback to $\Sigma\Delta$ filters for odd-quantisation
\hat{v}_{q_e}	Cartesian quadrature feedback to $\Sigma\Delta$ filters for even-quantisation
v_r	Amplitude component of the Polar $\Sigma\Delta$ filtered signal

\hat{v}_r	Quantised Amplitude in Polar co-ordinate
\hat{v}_{r_e}	Quantised Amplitude in Polar co-ordinate for even-quantisation
\hat{v}_{r_o}	Quantised Amplitude in Polar co-ordinate for odd-quantisation
v_δ	Polar quadrature of phase component of rotation frequency output
\hat{v}_δ	Quantised derotation of phase component in Polar co-ordinate
w_n	Waveform PWM/PPM
x_i	Cartesian in-phase of rotation frequency output
x_q	Cartesian quadrature of rotation frequency output
X	Rotation phase
\hat{y}_i	Cartesian in-phase of output amplitude quantiser
\hat{y}'_i	Cartesian in-phase of output pre-distorted amplitude quantiser
\hat{y}_q	Cartesian quadrature of output phase quantiser
\hat{y}'_q	Cartesian quadrature of output pre-distorted amplitude quantiser
$y(t)$	Total output phase pulse width
$\tilde{Y}(f)$	Convolution of spectrum of oscillator signal and gate signal
z^{-1}	Unit delay of low-pass $\Sigma\Delta$ filter
z^{-2}	Unit delay of band-pass $\Sigma\Delta$ filter
z_c	Zero crossing of the <i>sinc</i> function

Chapter 1

Introduction

Research in green communications is addressing the energy efficiency of the telecommunications sector, to reduce the cost of emissions and the world's carbon footprint. The relationship between energy consumption and the typical transmission components of a Radio Base Station (RBS) is highlighted in [1]. The Radio Frequency (RF) components, including upconverters and Power Amplifier (PA) units, account for 70% of RBS power consumption. It is estimated that the Base Station (BS) component alone accounts for 55% of the total electricity budget for a typical radio operator (such as *Vodafone*, *Telstra*, and *Optus*) [2]. Combining the two figures indicates that almost 40% of all operators' entire energy cost is tied up in the RF component transmission and receiving mobile phone signals. Energy consumption is now an important driving factor in the design of RF transmitters, and motivates this thesis.

Connectivity through wireless devices continues to play an important role in most people's daily lives. The key challenge is to satisfy the customer demand for an

increasing number of smart phones, tablets and other (portable) mobile devices. Figure 1.1 shows the anticipated growth in mobile communication over the next few years (until 2016) [3]. This growth can be obtained by improving the spectrum efficiency (in bits per Hertz per cell) or allocating more spectrum to mobile communications. The figure shows the operators are facing a rapid growth in capacity demands with a minimal increase in spectrum bandwidth and spectral efficiency. The capacity gap can only be filled by increasing the cell density. This has led to the rapid deployment of macro cells, micro cells and Pico cells. It is anticipated therefore that demand for small or indoor cell sites, known in the industry as Femto cells, will rapidly increase.

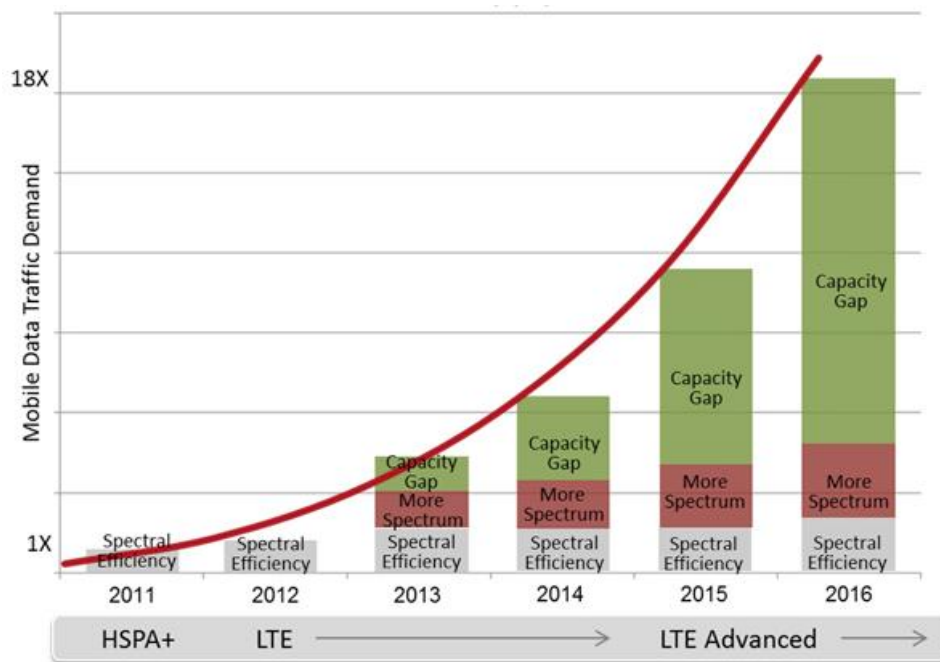


Figure 1.1: The mobile network capacity gap keeps widening with minimal anticipated increases in spectrum and efficiency [3].

A Femto cell needs to handle a variety of technologies such as Wireless Local Area Network (WLAN), mobile 3rd Generation (Wideband Code Division Multiple

Access - WCDMA), 4th Generation (Advanced Long Term Evolution - ALTE), and future 5th Generation networks [4-13]. The Femto cell hardware should handle all these different standards in a low cost power efficient way. This thesis is concerned with the transmitter section of such a Femto cell, which modulates the Baseband (BB) signal to RF and provides amplification.

1.1 Indoor Wireless Transmitter

Limited coverage, low spectral efficiency and poor performance experienced by indoor users of cellular mobile networks lead to bad customer experience. Poor service quality is sometimes caused by high penetration loss and wall attenuation of the radio signal resulting in existing network providers finding it difficult to provide high data rates for indoor coverage. As a result, this has motivated the recent emergence of the small-cell concept based on Femto cell architectures [14-18].

A majority of user mobile traffic originates from indoor locations. According to [19], the mobile traffic generated in the indoor locations (i.e. home, office) was estimated at 40% in 2007. By 2012, it reached 81% (55% of all mobile traffic occurred at home and 26% occurred in the office). This percentage has been increasing over time and is expected to increase further. If a user has a home BS at his/her home (and/or office), then the existing macro cell networks need only carry the remaining 19% of traffic which is generated at outdoor locations. Femtocells, often called home BSs, are small cellular access points installed by home users to extend voice and data coverage, which leads to lowering the network's capital cost. Typically, Femtocells are connected to the Internet via a Digital Subscriber Line (DSL), cable modem, or optical fibre. A recent study

estimated that by 2020, there will be more than 50 billion Internet connected devices [20].

Femto cell networks rely on sharing frequencies with other similar networks [14, 15] while enhancing the capacity and coverage indoors; consequently this activity may cause interference to other users in surrounding networks [16-18]. Therefore, Femto cell transceivers need to be low powered to reduce their interference footprints. They should also have frequency flexibility to change channels quickly and avoid interference from other Femtocells. The Femto cell transmitter should have good linearity and good fidelity which implies a low Error Vector Magnitude (EVM) and low Adjacent Channel Power (ACP). Next generation Femto cell BSs will need to be small, low cost, power efficient, wide bandwidth, frequency flexible and programmable to different wireless standards if they are to meet the key challenges of achieving cost-efficient provision of coverage and capacity [2].

1.2 All-Digital Wireless Transmitter

Software-Defined Radio (SDR) is gaining popularity because digital circuits provide software controllable features such as coding/decoding, modulation/demodulation, filtering, mixing, and power control [21-23]. The trend in SDR is to push the digital part close to the antenna part to remove analog selection mechanisms. However, traditional SDR still requires some analog components such as Analog-to-Digital and Digital-to-Analog converters (ADC/DAC), up/down converters, RF selectivity and RF amplification.

Femto cells have low output power and this allows the possibility of a fully-digital implementation. Digital wireless transmission is related to all-digital transmitter design with fully-digital components. To move towards all-digital wireless transmitters, the elimination of analog components is required. Various signal processing innovations are now being proposed by the research community to this end. If such a solution can be found then integration on to low cost digital *Silicon* Complementary Metal Oxide Semiconductor (*SiCMOS*) technology will produce a major reduction in both size, cost and energy consumption.

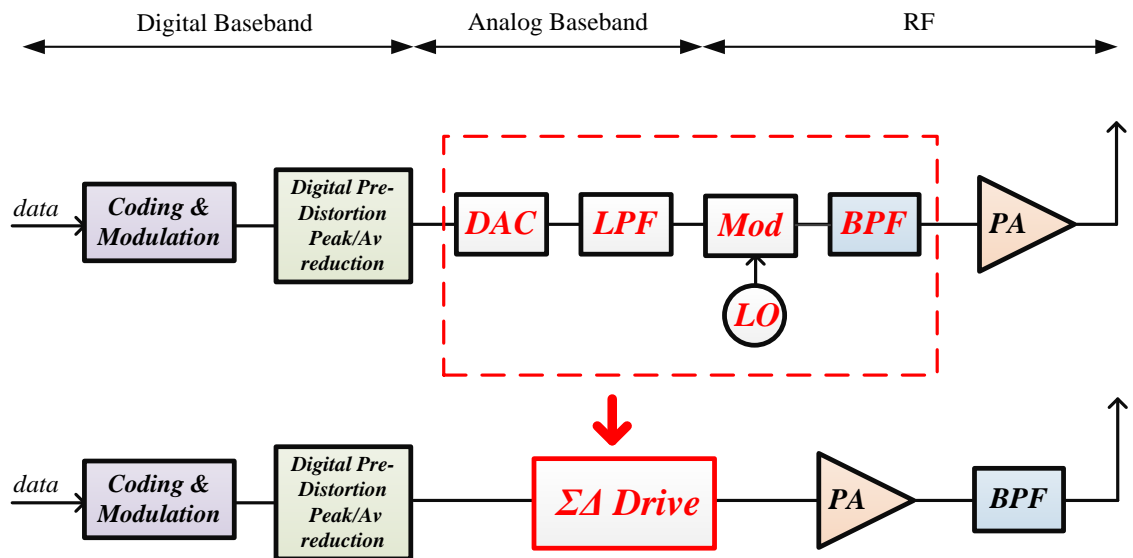


Figure 1.2: Sigma-Delta ($\Sigma\Delta$) structure can potentially replace the analog components of the traditional wireless architecture (top). A potential future wireless transmitter architecture (bottom).

A traditional wireless transmitter architecture is described in Figure 1.2 (top). It consists of analog components such as ADC/DAC, filters, a Modulator (MOD), and a Local Oscillator (LO). A new wireless transmitter architecture in Figure 1.2(bottom) has

introduced the use of a digital Sigma-Delta ($\Sigma\Delta$) structure which replaces the analog components from the traditional transmitter architecture. Removal of the analog components also removes many analog problems, such as gain-phase imbalance and carrier leakage of the quadrature modulator, the need for an RF synthesiser and the need for wideband matching of the Low-Pass Filters (LPF).

$\Sigma\Delta$ techniques are most well known for their use in ADC and DAC structures. These schemes are almost entirely based on the conversion of low-pass signals. The best known early application of $\Sigma\Delta$ DACs was for the Compact Disc (CD) player [24]. Here the sample rate was increased to reduce the (quantisation) noise power spectral density which was shaped by a first order filter to further reduce the noise in the lower frequencies. In this way, high fidelity signal reproduction was possible from DACs' reduced resolution. Similarly, in this thesis, $\Sigma\Delta$ techniques allows the RF signal to be coarsely quantised in amplitude and phase.

1.3 Wireless Transmitter Challenges

The demand for broadband wireless connectivity has forced the development of wireless standards with wider bandwidth, higher data rate, and spectrum efficiency. Orthogonal Frequency Division Multiplexing (OFDM) and Code Division Multiple Access (CDMA) nowadays can support wider bandwidth and higher data rate communication in multi-carrier systems. However, OFDM and CDMA suffer from high Peak-to-Average Power Ratio (PAPR) that will limit the transceiver energy efficiency [25-27]. Power amplifier linearity in the transmitter is critical [28-30]. The BS also needs to operate with high energy efficiency. The combined requirements of high bandwidth,

high data rate, high efficiency, linearity and signal dynamics make the design of RF-PAs difficult.

All PA classes (Class A, B, AB, C, D, E, F, etc.) can be operated with a switching input waveform if their bandwidth is wide enough, hence RF Pulse Width/Position Modulation (RF PWM/PPM) is a potential technique for future high efficiency transmitter architectures. A low power BS could use Switched-Mode Power Amplifier (SMPA) techniques to improve power efficiency. The ON-OFF nature of the waveforms means that 100% power efficiency is theoretically possible, but in practice is difficult to achieve at RF. SMPAs need to be driven by a two state signal or a pulse train generated from a polar representation of the transmitted BB signal. This combined with the ever improving speeds of digital *Silicon* technology has led to renewed interest in transmitter architectures based on PWM/PPM. Figure 1.3 shows the waveforms involved. A Band-Pass Filter (BPF) is needed to change square pulses into the RF carrier. The pulse widths control the RF amplitude and the pulse positions the phase. The clock frequency, f_{clock} , must be much larger than the nominal carrier frequency, f_c . It is normal to quantise the phase and magnitude components of the modulation such that the pulse edges align with the digital clock (for synchronous digital design).

However, some problems and challenges still remain in the new wireless transmitter architecture. The rectangular nature of the output pulse generates a number of unwanted harmonics and distortion products which fold in-band and cannot be filtered out. Therefore, the management of noise shaping associated with the $\Sigma\Delta$ filtering and reduction of noise and distortion is a key system design challenge. Other problems that need to be solved are: the need for a small Oversampling Rate (OSR), defined as $\left(\frac{f_{clock}}{f_c}\right)$;

and the need for some form of tuning of the RF carrier without changing the digital clock frequency.

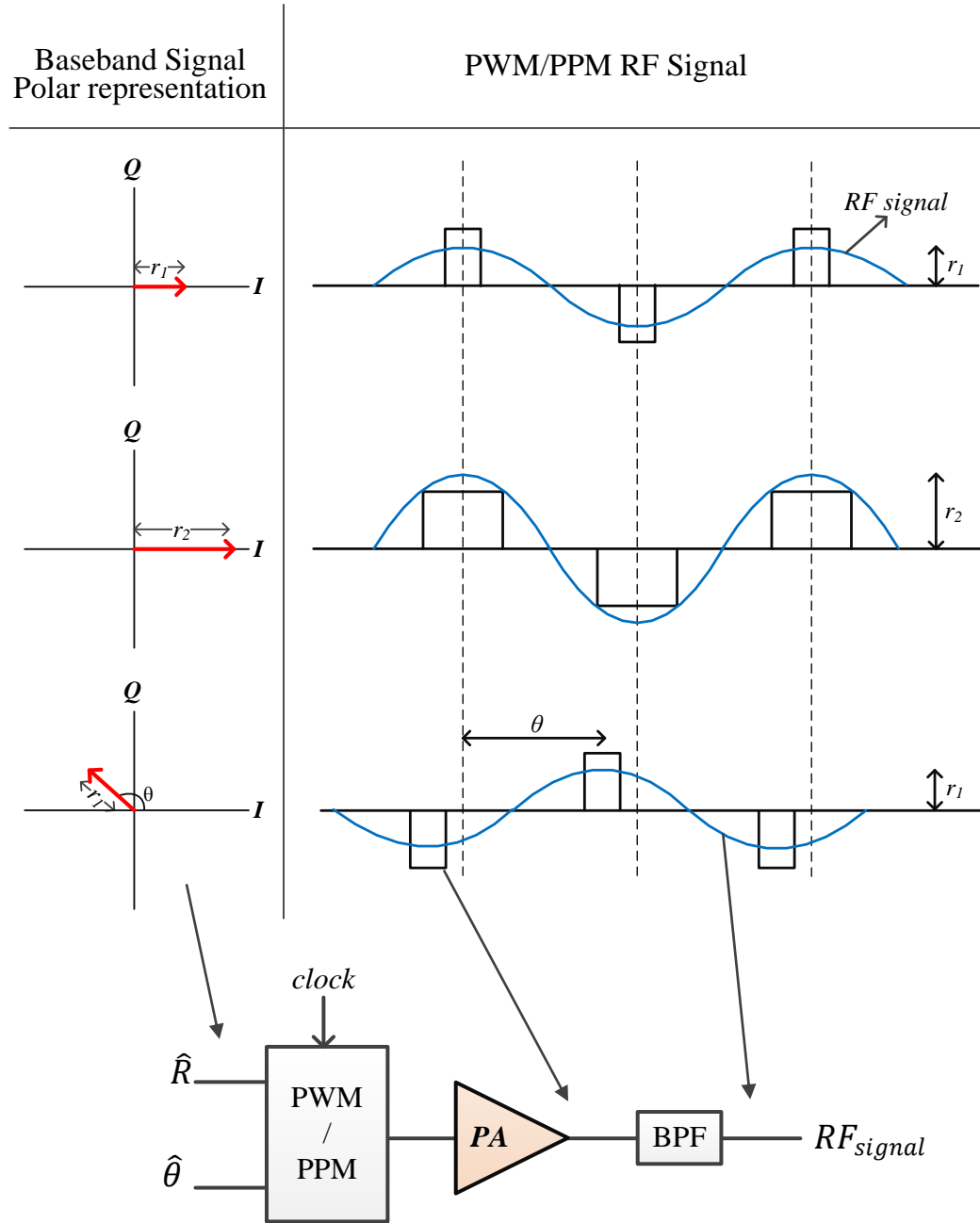


Figure 1.3: PWM/PPM RF signal is generated from the polar baseband signal.

1.4 Research Objective

This research aims to develop a low power transmitter structure suitable for small coverage areas such as those used in a Femto cell. The study aims to develop a new $\Sigma\Delta$ GHz transmitter that will be suitable for low power transmission but with high efficiency and effectiveness for flexible frequency transmission. The developed structure will allow all digital tunability and eliminate the need for analog components.

The following are the identified specific objectives:

- To improve the output spectrum of switched-mode RF-PAs. This involves a new quantisation scheme that has better performance at lower signal power.
- To improve the tuning range of the carrier frequency by removing the noise and unwanted spectral components (distortion). This will enable operation in the cellular frequency band, increasing the applicability of the scheme. The developed structure will allow all digital tunability without changing the clock frequency and so eliminate the need for a synthesiser.
- To demonstrate the schemes' viability through physical measurement and simulation results.

1.5 Thesis Contribution

The following novel contributions have been made in this thesis:

- Improved quantisation schemes called odd quantisation and joint quantisation have been proposed. It is clearly shown that the odd quantisation scheme

outperforms the even quantisation scheme by about 2 dB in terms of signal-to-noise ratio and the joint quantisation scheme gives a further 3 dB reduction.

- A new frequency tuning method has been developed. It involves phase rotators before and after the quantiser.
- A deliberate intermediate frequency shift equal or greater than the transmission bandwidth plus half of a channel bandwidth has been shown to move all distortion products out of band.
- A mathematical derivation has been developed to predict the size and position of the unwanted image. Pre-distortion of the signal input can be used to null the image. This has been experimentally verified.
- A method for reducing noise enhancement caused by frequency tuning has been developed. It involves distorting the feedback signal in the $\Sigma\Delta$ converter.

1.6 List of Publications

A number of peer-reviewed publications have been generated from the research accomplished in this thesis.

1. S. Sirmayanti and M. Faulkner, “ $\Sigma\Delta$ modulator for digital wireless architecture: A review,” in *4th IEEE Makassar International Conference on Electrical Engineering and Informatics (MICEEI)*, 2014, pp. 83-87.
2. S. Sirmayanti, V. Bassoo, H. King, and M. Faulkner, "Baseband tuning of Cartesian delta–sigma RF upconverters," *Electronics Letters*, vol. 50, pp. 635-637, 2014.

3. S. Sirmayanti, V. Bassoo, and M. Faulkner, "Joint odd-even quantisation in cartesian delta-sigma (DS) upconverters," in *2013 AFRICON*, 2013, pp. 1-4.
4. S. Sirmayanti, V. Bassoo, H. King, and M. Faulkner, "OFDM performance with odd-even quantisation in Cartesian $\Delta\Sigma$ upconverters," in *6th IEEE International Conference on Signal Processing and Communication Systems (ICSPCS)*, 2012, pp. 1-5.
5. S. Sirmayanti, V. Bassoo, H. King, and M. Faulkner, "Odd-even quantisation and cartesian delta-sigma ($\Delta\Sigma$) Upconverters for Transmitter Design," in *IEEE International Conference on Communication Systems (ICCS)*, 2012, pp. 100-104.
6. S. Sirmayanti, V. Bassoo, H. King, and M. Faulkner, "Sigma delta ($\Sigma\Delta$) architecture integration with digital pre-distortion to enhance optimal switch mode power amplification (OSMPA) in FEMTO cell transceiver design," in *IEEE 8th International Conference on Information, Communications and Signal Processing (ICICS)*, 2011, pp. 1-4.
7. Sirmayanti, S., "Non-uniform Joint quantisation on Cartesian Delta-Sigma (DS) Upconverters", presented in *Australian Communications Theory Workshop (AusCTW)* (poster), Adelaide Australia, 29 January – 1 February 2013.

1.7 Thesis Organisation

This thesis is organised as follows:

- ❖ Chapter 1 outlines the motivations behind the research. The research objective are presented. The thesis contribution and a list of publications related to the results and finding are given.

- ❖ Chapter 2 provides the necessary background information of relevant existing literature. Firstly, a summary of power amplifiers is presented. Next, $\Sigma\Delta$ modulation is discussed in terms of signal and noise transfer functions and implementation architectures. The application of $\Sigma\Delta$ technique to RF transmitters is reviewed. This chapter also explains the recent Cartesian $\Sigma\Delta$ upconverter scheme [31], which is the basis of the proposed schemes in this thesis.
- ❖ Chapter 3 describes new quantisation schemes to improve the proposed Cartesian $\Sigma\Delta$ upconverter. The odd quantisation scheme is proposed as replacement for the even quantisation method of [32]. Performance is improved at low signal levels. Further improvement in noise floor can be obtained by combining both odd and even quantisation. Simulation and measurement results are presented and implementation aspects discussed.
- ❖ Chapter 4 investigates why $\Sigma\Delta$ -RF upconverters have poor performance when the carrier frequency is tuned away from the centre of the band. A novel technique for shifting both the signal and the noise null to the new frequency position is described.
- ❖ Chapter 5 gives an improved mathematical analysis of the distortion formation process caused by polar to PWM/PPM conversion. Image cancellation and noise cancellation techniques are proposed to solve the distortion problems. Digital pre-distortion can eliminate many of the unwanted signals. Simulations and measurements for different scenarios authenticate the finding.
- ❖ Chapter 6 concludes the work and suggests possible future research opportunities.

Chapter 2

Literature Review

2.1 Introduction

This chapter provides the background information of relevant existing literature. It provides an overview of basic traditional linear PA structures in Section 2.2 and is followed by the trend of digital transmitter architecture with nonlinear SMPAs in Section 2.3. A review of $\Sigma\Delta$ modulators is discussed in Section 2.4. Section 2.5 covers interpolation and decimation for $\Sigma\Delta$ modulators and Section 2.6 covers coding efficiency. Section 2.7 reviews the modulation techniques for switched PA's. Section 2.8 covers $\Sigma\Delta$ modulators and discusses the background and use of Cartesian $\Sigma\Delta$ scheme as the proposed method in this thesis. Three different transmitter architectures based on the $\Sigma\Delta$ structures will be discussed in this section. Section 2.9 discusses RF tuning and Section 2.10 is the summary.

Part of the literature work in this chapter has been presented as a conference paper titled “Sigma delta ($\Sigma\Delta$) architecture integration with digital pre-distortion to enhance optimal switch mode power amplification (OSMPA) in Femto cell transceiver design” at the *IEEE International Information, Communications and Signal Processing Conference* in 2011 [33] and “ $\Sigma\Delta$ modulator for digital wireless architecture: A review,” at the *IEEE 4th Makassar International Conference on Electrical Engineering and Informatics (MICEEI)* in 2014 [34].

2.2 Traditional PAs Architecture

Power amplifiers have been traditionally categorised under many classes: Class A, B, C, D, E, F, etc. [35]. These classes can be classified into two different families: non-switching (Class A, B, and C) and switching (Class D, E, and F) [36].

2.2.1 Non-switching Amplifiers

Class-A amplifiers commonly have the highest linearity over the other amplifier classes since these amplifiers pass current for the entire 360° cycle [37]. The topology has poor energy efficiency since a bias current in addition to the load current is required. The transistor is always biased ON and the output is sinusoidal. The efficiency peaks at 50% of maximum output power, and reduces with input power backoff thereafter.

Class-B amplifiers have no standing bias current and therefore each transistor conducts for only half of each cycle (180°) of the signal waveform [37, 38]. There is no power consumed in the negative half cycle, on the other hand, Class-B amplifiers have severe distortions due to the missing half cycles. Resonators filter out the distortions or

the missing half cycle can be replaced using a push-pull architecture. Theoretical peak efficiency is 78.5% at peak output power [36]. Furthermore, Class-AB amplifiers use small bias current to improve linearity at low signal levels [39].

Class-C amplifiers operate with a drain conduction angle of less than half of one cycle ($< 180^\circ$). The efficiency in Class-C amplifier is typically higher than other PAs. Class-C can offer a maximum efficiency approaching 100% at small conduction angles, however they only deliver a fraction of their power capability [37]. These amplifiers have a limited dynamic range, sometimes below 6 decibels (dB), and have a tendency to snap off if the RF input signal is reduced below the required level.

2.2.2 The Doherty PA Architecture

The Doherty amplifier is a Class-B amplifier modification. The basic principle is to combine the outputs from two or more different RF power amplifiers through a transmission-line coupler. At low output levels, only the first PA operates. As the output power is increased beyond the maximum power of the first PA, the second PA is added to further boost the signal. The first PA is therefore operating at its most efficient state (maximum output power) for a longer time. As this is the conventional Class-B amplifier modification, the Doherty PA can be considerably more efficient; for example there is 60% efficiency improvement compared to the 28% average efficiency of Class-B PA with a modulated RF signal having a Rayleigh-distributed envelope of 10 dB PAPR [40]. The Doherty PA maintains high efficiency over a large range of output powers compared to a traditional Class-B. It is used in many mobile BSs today.

2.2.3 Envelope Elimination and Restoration (EER) and Envelope Tracking (ET)

EER was first proposed as a linearization method. A block diagram of EER is shown in Figure 2.1 [41]. The phase and amplitude of the signal information are separated. A *limiter* eliminates any amplitude modulation to provide a constant phase modulated signal. The phase information is passed directly to the power amplifier which operates in saturation; its most efficient state. The amplitude information is isolated by an *envelope detector*. The envelope is restored onto the carrier by driving the RF PA's bias drain voltage (Figure 2.1). This is a high power signal and the envelope amplifier must be switch-mode if efficiencies are to be high. The switch-mode limits the bandwidth and practical dynamic range of the system [42].

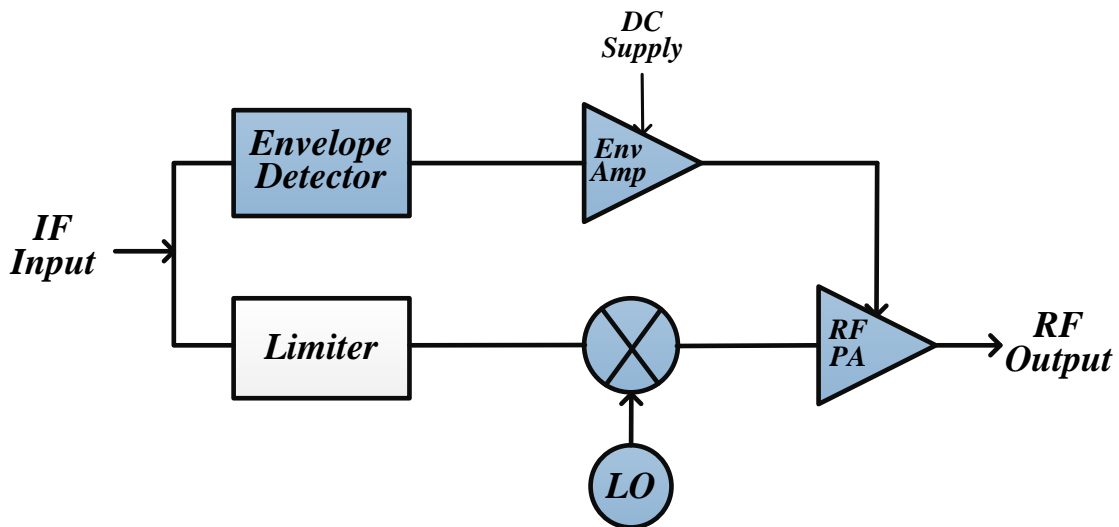


Figure 2.1: An Envelope Elimination and Restoration (EER) architecture. The Envelope Tracking (ET) architecture is similar with the EER but without *limiter*.

The phase and amplitude information have to arrive at the same time, thus the phase information is typically delayed to match the time delay between the two paths. The polar signal in the transmitter has expanded bandwidth. Signal conditioning techniques to reduce the bandwidth of the polar components have been proposed by Mustafa *et al.* [43]. In this way, phase components do not meet any rapid transition that can increase the drive signal bandwidth. An alternate structure closely related to EER is envelope tracking (ET), which has the same structure as Figure 2.1 except the limiter is removed. ET has less problems with bandwidth expansion and is the preferred structure for many modern RF amplifiers.

2.3 Switched-Mode RF Power Amplifiers (RF-SMPAs)

The idea behind PA design in wireless communication research is to maintain high efficiency as well as good linearity of the signal bandwidth [44]. SMPA technology has been developed as a method to obtain high PA efficiency at low frequencies. Current research is to apply SMPA transmitter design in the frequency range 1-4 GHz [45-47]. Theoretically, SMPAs have efficiency of around 100%, but since transistors do not operate as perfect switches at these frequencies practical issues dominate their performance [48, 49]. They show reduced efficiency at higher frequency due to the substantial losses in the parasitic output capacitance of the power device [50].

Depending on the topology, examples of SMPA classes are Class D, S, E, and F [36]. Class-D amplifiers generally have more energy losses, while Class-E and Class-F

try and include the parasitic loss capacitance in an output tuning network which recycles some of the lost energy.

2.3.1 Class-D Amplifier

In [48], there are two main schemes of Class-D PA topology designs which consist of two transistors: voltage-mode with serial resonator circuit (Figure 2.2(a)) and current-mode with parallel resonator circuit (Figure 2.2(b)). Even though the efficiency in the voltage-mode is high for audio implementation, the capacitance of transistor output becomes a dominant switching loss factor at higher frequencies [50]. It is therefore difficult to achieve the same good efficiency in the GHz frequency range. It is however suitable for pulse width modulated signals. The current-mode structure is a good amplifier with a high peak efficiency at GHz frequencies. The transistors are grounded and their parasitic output capacitance are used in the output filter. Unfortunately the efficiency quickly reduces when pulse width modulation is applied.

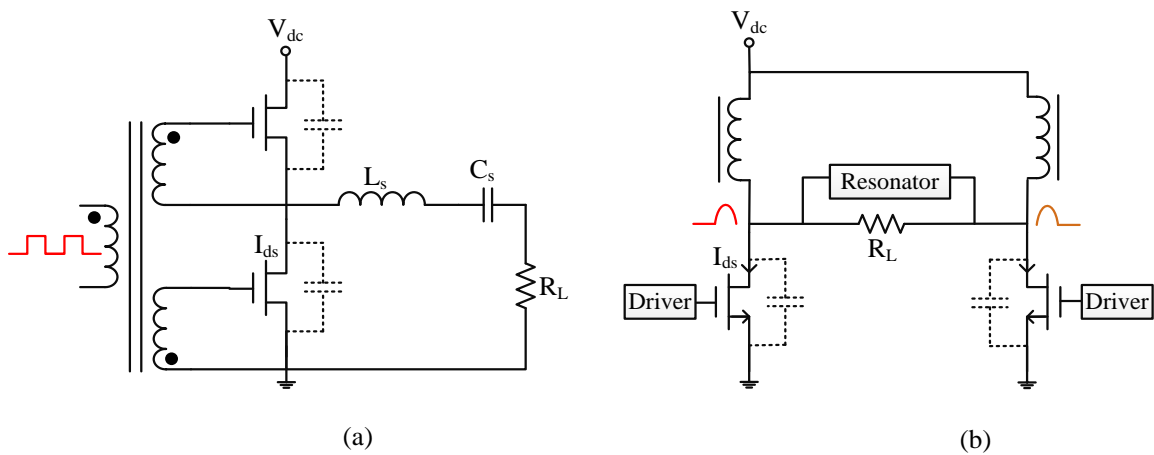


Figure 2.2: (a) Voltage-mode [50] and (b) current-mode [48] of a Class-D PA.

An extension of the Class-D is the Class-T, which includes noise shaping and feedback circuits to reduce distortion and is primarily targeted at audio applications. See US Patent 5,777,512 [51] for further details.

2.3.2 Class-S Amplifier

Class-S amplifiers have a similar structure to Class-D. They can achieve an efficiency theoretically up to 100% and maintain good efficiency over a wide dynamic range in practice [36]. Practically it is much less due to device parasitics, even so, efficiencies of 38% at 450 MHz carrier frequency have been reported using *gallium nitride* (GaN) power MOS transistors [52, 53]. The efficiency of the Class-S amplifier was further improved by using a switching waveform with higher coding efficiency [54]. The transistors of Class-S are driven by square waveform i.e. using an appropriate pulse width modulation, which is often produced by a band-pass $\Sigma\Delta$ modulator at the input (Figure 2.3).

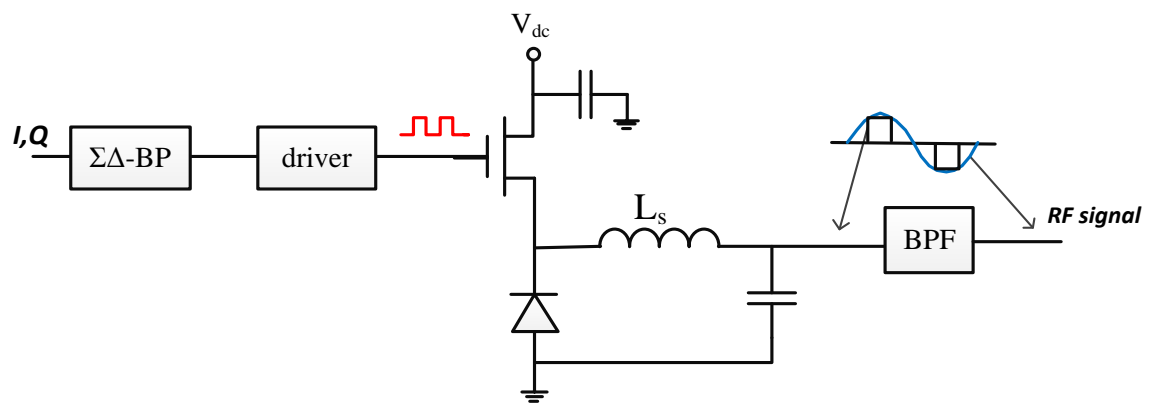


Figure 2.3: Schematic of Class-S PA [36, 55].

2.3.3 Class-E Amplifier

Class-E amplifiers operate as a switch in combination with a resonant circuit. They have a zero overlap between voltage and current on the load line of the transistor so in theory they can achieve an efficiency of 100% [56]. The waveform of the Class-E amplifier is analog in shape and so it supports transistors with a slower switching operation. Class-E amplifier with a parallel circuit has been developed by Grebennikov *et al.* [57]. The parallel circuit includes a parallel capacitance, a parallel inductance and a series resonant circuit. The parasitic output capacitance becomes part of the resonant circuit avoiding the $\frac{1}{2}CV^2$ energy loss that occurs every cycle, as in voltage-mode Class-D structures. Figure 2.4 shows schematic of a Class-E PA. Class-E amplifiers have high efficiency at an output power level, but this quickly clean away as the output level changes. They are less suitable for signals containing amplitude modulation. The later problem was overcome in [58] by altering the load reactance band on the signal level, 55% overall efficiency was maintenance over a 6.5 dB dynamic range.

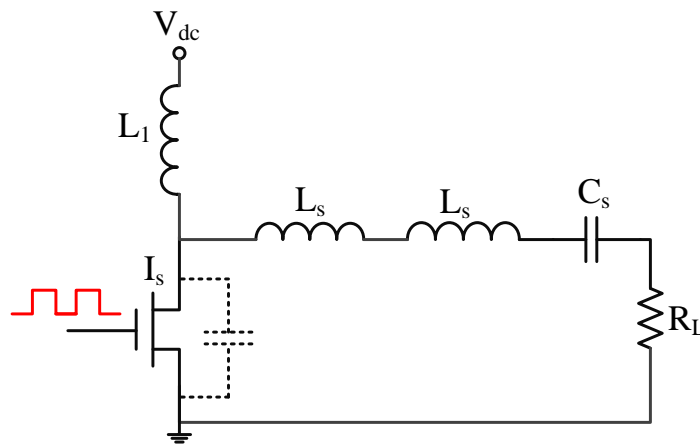


Figure 2.4: Schematic of a Class-E PA.

2.3.4 Class-F Amplifier

Class-F amplifiers ideally have multiple resonators to control frequency harmonic contents of the drain voltage. In most Class-F amplifier designs, the drain output harmonics must be presented with either an open or short circuit. In this way, the output waveform can be made squarer looking, reducing the power dissipating current/voltage cross-over region. The main concern in the practical design of this structure is the optimum termination of the third harmonic, at high frequencies. Colantonio *et al.* [59] and Raab [60] stated that the maximum power and efficiency in Class-F amplifiers are limited to 75% if only the third harmonic is terminated. A 2.2 GHz design would therefore require a 6.6 GHz harmonics termination [48].

2.3.5 Bridge Structure

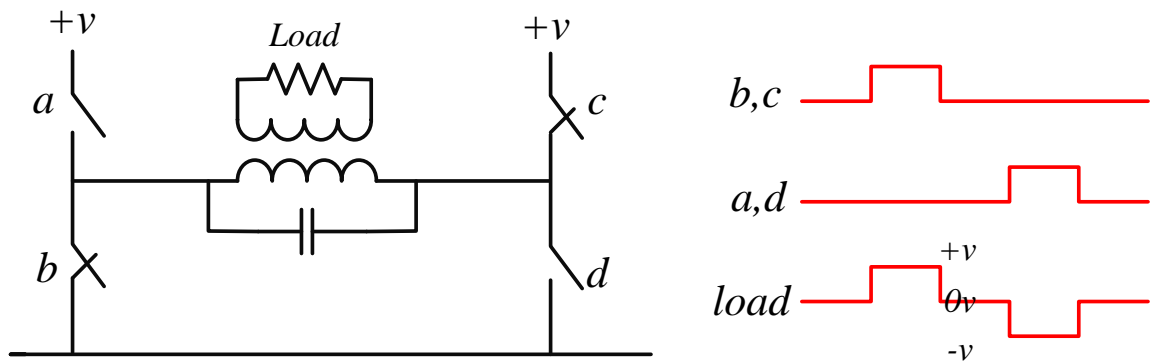


Figure 2.5: Generation of a three-level waveform with bridge structure.

All the previous amplifiers have been described in their single-ended or push-pull form. Full-bridge forms are also possible, and can be advantageous for switching PAs. Figure 2.5 shows the structure [31]. Using this structure it is possible to generate a three-

level signal across the load using two digital input streams. A positive load voltage occurs with switches b and c closed, a negative voltage occurs with switches a and d closed, and a zero voltage occurs when all are open. Three-level waveforms are ideal for RF signal generation and will be used extensively in this thesis.

2.4 $\Sigma\Delta$ Modulators

The $\Sigma\Delta$ technique has been in existence for many years and is primarily used for analog-to-digital (A/D) and digital-to-analog (D/A) conversion. Its wide dynamic range, low chip area, and low power consumption make it the converter of choice for many medium bandwidth applications such as found in many consumer electronic items. Research in $\Sigma\Delta$ techniques is now including RF structure that replace many analog components required in a traditional wireless transceiver architecture.

2.4.1 Basic $\Sigma\Delta$ Modulation

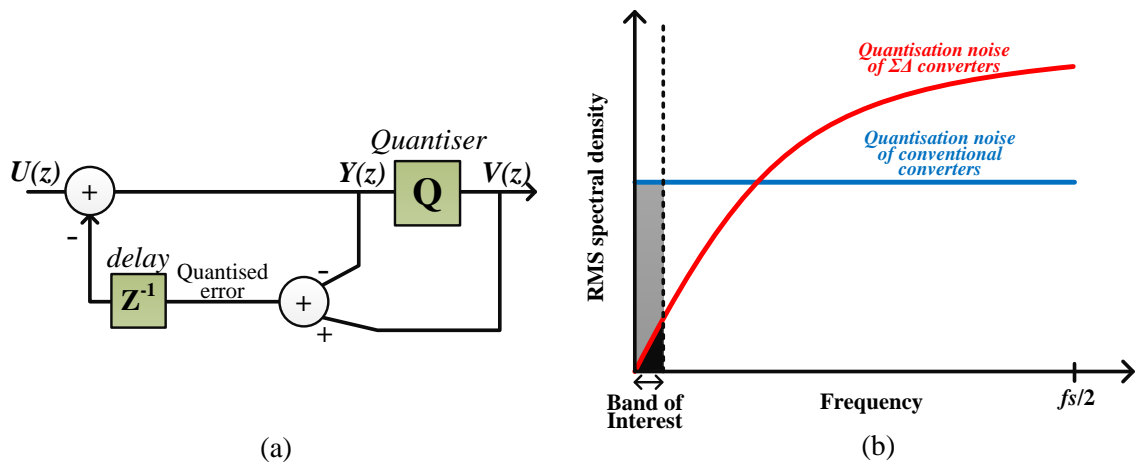


Figure 2.6: (a) 1st order $\Sigma\Delta$ modulator (MOD1) and (b) quantisation noise power spectral density vs. frequency for conventional and $\Sigma\Delta$ converters. f_s is the $\Sigma\Delta$ sample rate [31].

$\Sigma\Delta$ techniques are used to spectrally shape quantisation noise away from the signal of interest. They operate by subtracting the current sample's quantisation error from subsequent samples [24]. In its basic form (first-order), the quantisation error of sample n will be removed in sample $n+1$ (Figure. 2.6(a)). This error feedback causes the $\Sigma\Delta$ system to act as a filter having separate transfer functions for noise and signal. The filtering of the quantisation noise by the noise transfer function (NTF) is shown by the red line in Figure. 2.6(b). Higher $\Sigma\Delta$ orders have greater noise shaping capabilities [24, 61].

Figure 2.7 (top) shows the basic structure of an A/D with the filter (integrator) implemented in analog, and Figure 2.7 (bottom) shows a D/A with the filter (digital integrator) implemented in Digital Signal Processing (DSP).

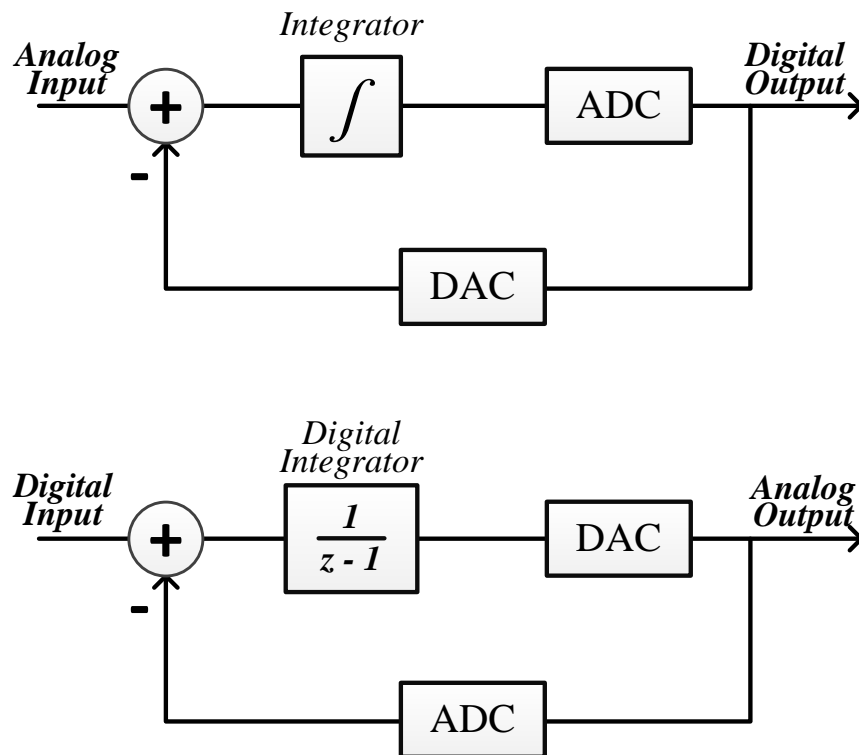


Figure 2.7: A $\Sigma\Delta$ modulator as an A/D converter (top) and D/A converter (bottom).

A $\Sigma\Delta$ modulator has two key features: a *noise shaping filter* which can distribute the quantisation error or noise away from the signal of interest, and a high *oversampling rate* which can reduce the power spectral density (PSD) of the quantisation noise [24].

2.4.2 Linear $\Sigma\Delta$ Modulator Model

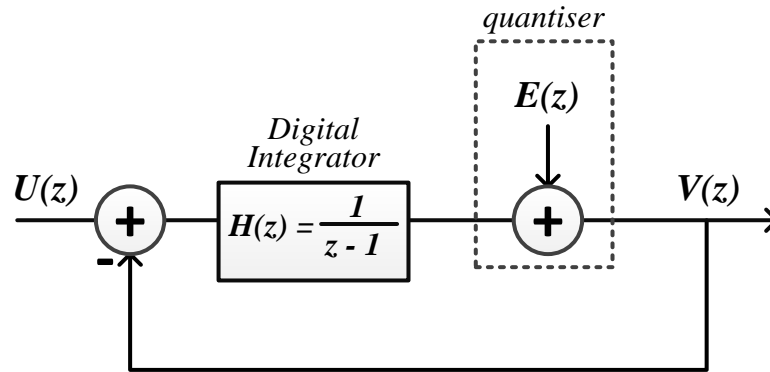


Figure 2.8: Linear z -domain of $\Sigma\Delta$ modulator (MOD1) of Figure 2.5(a) structure.

A *basic* first-order $\Sigma\Delta$, which consists of a quantiser and digital integrator, is shown in Figure 2.8. The $\Sigma\Delta$ modulator is normally linearised to make it easy to do the mathematical analysis. The linear model assumes that the quantiser can be considered as an uncorrelated white noise source, $E(z)$, and then the output becomes the summation of the quantisation noise shaped by the NTF and the input signal shaped by the signal transfer function (STF). The digital filter $H(z)$ takes the form of an integrator with transfer function $\frac{1}{z-1}$ and operates as a *noise shaping filter* on $E(z)$ and as a *signal shaping filter* on $U(z)$. A single integrator system (1st order) is often called first-order modulator (MOD1). The integrator provides an infinite gain at direct current (DC) which results in

zero noise at DC. Increasing the order of $H(z)$ in the circuit can further improve the noise shaping characteristic.

2.4.3 Signal Transfer Function (STF) and Noise Transfer Function (NTF)

The Δ and Σ description can be seen in the *basic* MOD1 z -domain representation of Figure 2.9 (top). The input signal $U(z)$ is subtracted from the previous output signal, corresponds to the Δ function; and the integrator corresponds to the Σ function. The feedback loop continuously forces the average of the quantised bit(s) to be equal to the input signal. By increasing the clock rate (or oversampling) and using a higher order $\Sigma\Delta$ modulator, it is possible to produce less noise at the lower frequencies. A cascade of two MOD1 structures is called a second-order modulator (MOD2), which is shown in Figure 2.9 (bottom) [24].

The quantisation noise is represented by the additive error term, $E(z)$, in the quantiser function $\mathbf{Q}(\cdot)$. The error is added in place of the quantiser. Therefore, $V(z)$, the output of quantiser function $\mathbf{Q}(\cdot)$ from Figure 2.9 is described as follows:

$$V(z) = Y(z) + E(z) \quad (2.1)$$

where $Y(z)$ is the input to the quantiser output and can be represented as:

$$Y(z) = U(z) + z^{-1}Y(z) - z^{-1}V(z) \quad (2.2)$$

for a MOD1 structure. $U(z)$ represents the z -transform of the input signal.

Substituting Equation 2.2 into Equation 2.1 defines the signal and noise transfer functions (STF) & (NTF), respectively can be defined for MOD1 as:

$$V(z) = U(z) + (1 - z^{-1})E(z) \quad (2.3)$$

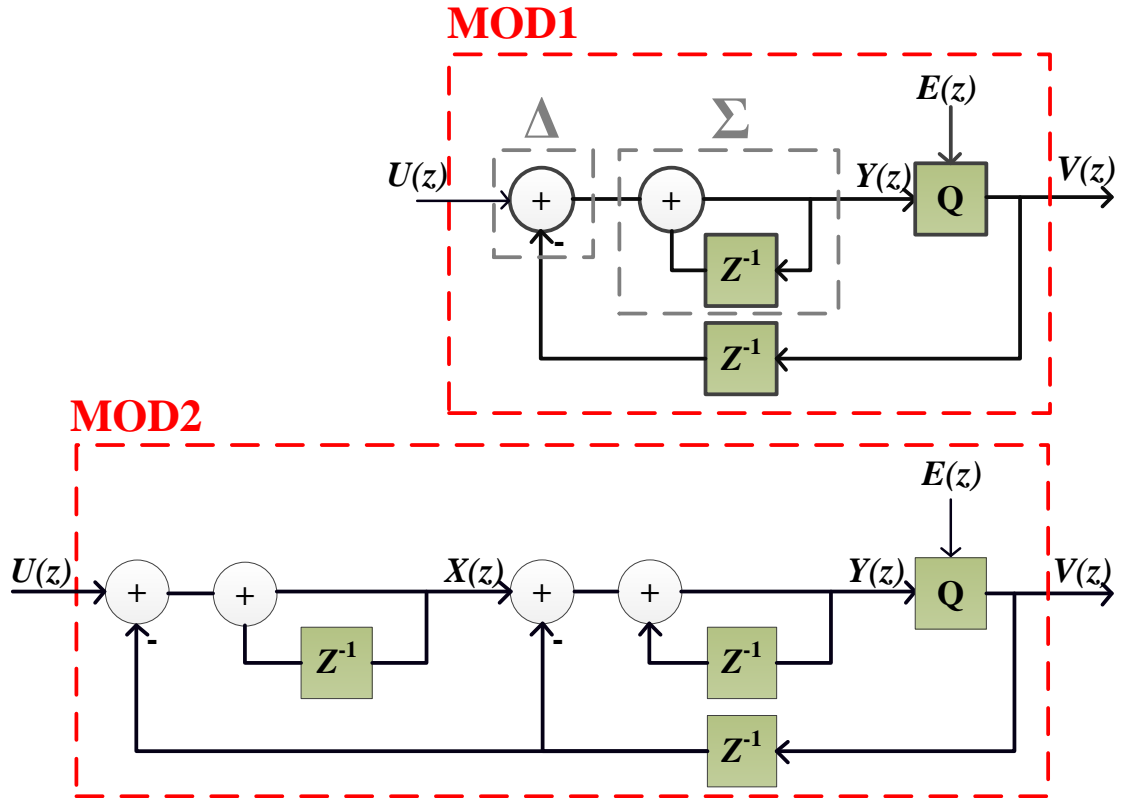


Figure 2.9: Linear model in z -domain of the *basic* MOD1 (top) and MOD2 (bottom).

or can be written as

$$V(z) = STF(z) U(z) + NTF(z)E(z) \quad (2.4)$$

when

$$STF_{MOD1} = 1 \quad \text{and} \quad NTF_{MOD1} = (1 - z^{-1}) \quad (2.5)$$

When $z = e^{j\omega}$, we can estimate the in-band power in frequency domain of the NTF, given by

$$NTF_{MOD1}(e^{j\omega}) = (1 - e^{-j\omega})$$

$$= [1 - (\cos\omega - j\sin\omega)] \quad (2.6)$$

The complex NTF in Equation 2.6 is now useful to find the magnitude of NTF which applies to the power spectral density of the noise shaping function. Thus,

$$\begin{aligned} |NTF_{MOD1}(e^{j\omega})| &= \left[\sqrt{\text{Re}[NTF(e^{j\omega})]^2 + \text{Im}[NTF(e^{j\omega})]^2} \right] \\ &= \left[\sqrt{(1 - \cos\omega)^2 + (\sin\omega)^2} \right] \\ &= \sqrt{2 - 2\cos\omega} \end{aligned} \quad (2.7)$$

Then the square magnitude of NTF MOD1 is

$$\begin{aligned} |NTF_{MOD1}(e^{j\omega})|^2 &= 2 - 2\cos\omega \\ &= [2\sin(\pi f)]^2 \end{aligned} \quad (2.8)$$

We now consider the STF and NTF for MOD2. The resulting structure shown in Figure 2.9 indicates there are two intermediate variables $Y(z)$ and $X(z)$, where

$$X(z) = U(z) + z^{-1}X(z) - z^{-1}V(z) \quad (2.9)$$

Similarly to MOD1, the MOD2 structure can be simply used to derive the general formula of quantiser output, $V(z)$, using Equation 2.2 and Equation 2.3 respectively as:

$$Y(z) = X(z) + z^{-1}Y(z) - z^{-1}V(z) \quad (2.10)$$

$$V(z) = U(z) + (1 - z^{-1})^2 E(z) \quad (2.11)$$

giving $STF_{MOD2} = 1$ and $NTF_{MOD2} = (1 - z^{-1})^2$ (2.12)

In the frequency domain:

$$\begin{aligned} NTF_{MOD2}(e^{j\omega}) &= [(1 - \cos\omega) + j\sin\omega]^2 \\ &= [4 \sin^2(\omega/2) (-\cos\omega + j \sin\omega)] \end{aligned} \quad (2.13)$$

Then, the square magnitude of the NTF MOD2 is given by

$$\begin{aligned} |NTF_{MOD2}(e^{j\omega})|^2 &= [4 \sin^2(\omega/2)]^2 \\ &= [2 \sin(\pi f)]^4 \end{aligned} \quad (2.14)$$

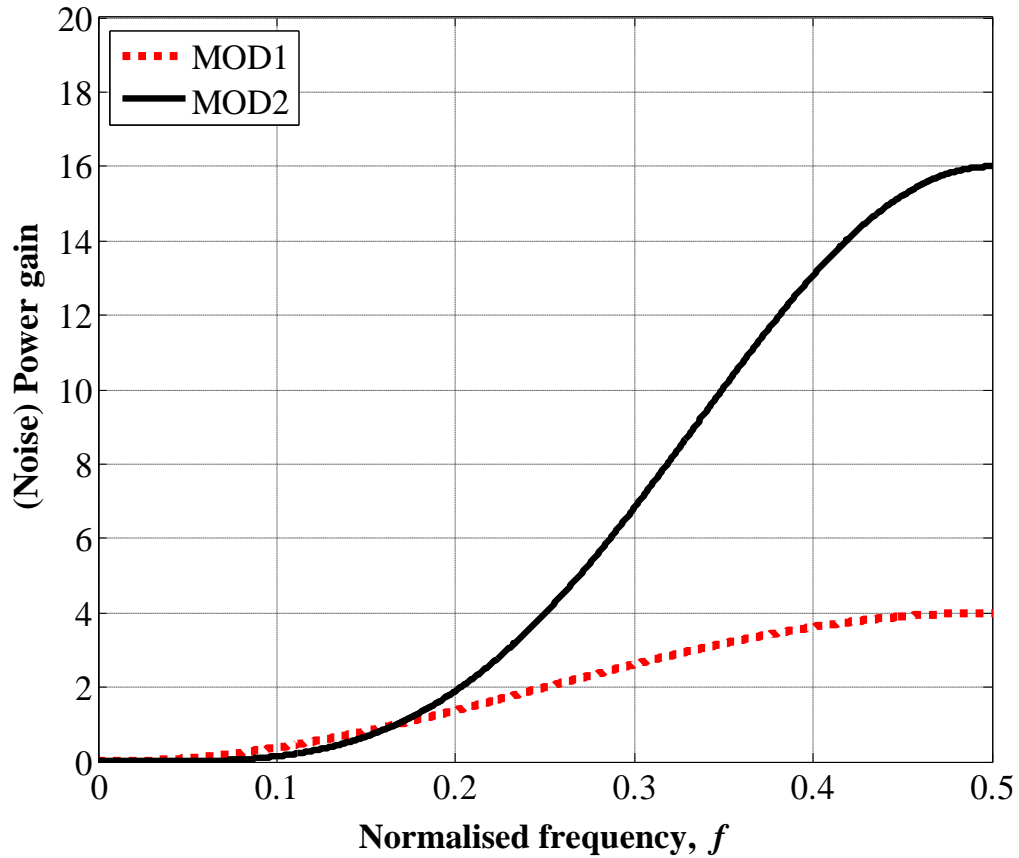


Figure 2.10: NTF for MOD1 and MOD2.

For normalised frequencies $f \ll 1$ (assume $f=0$), $|NTF_{MOD1}|^2 = |NTF_{MOD2}|^2 \approx 0$. This clearly shows that the quantisation noise can be suppressed or amplified away from the desired signal due to the *noise-shaping filter* action. This action is the key feature of the effectiveness of $\Sigma\Delta$ modulation in the low frequency regions.

The comparison of the noise shaping between MOD1 and MOD2 is described in Figure 2.10. The *total* power of the quantisation noise of MOD2 is much higher than MOD1 because the frequency gain of MOD2 is greater than MOD1's NTF. However, the noise shaping of MOD2 is much lower than MOD1 in the band of interest (near DC). The crossover frequency occurs at about $0.17 \times f_s$. MOD2 will be the preferred structure for the Cartesian $\Sigma\Delta$ upconverter used in this thesis.

2.4.4 NTF Low-pass $\Sigma\Delta$ Modulator: Poles and Zeros

The noise shaping of NTF can be controlled by the position of the poles and zeros of $NTF(z)$. Following [24] the design approach is: (i) to place the zeros to null the noise, and (ii) to place the poles to keep noise enhancement $\max_{\omega} |H(e^{j\omega})| < 1.5$ for stability and filtering consideration. The approximation is known as the modified *Lee criterion* [24]. It is a guide only; under some circumstances $\max_{\omega} |H(e^{j\omega})|$ can go higher than 1.5 as will be illustrated in the MOD1 case. The NTF transfer function can be written in terms of poles (p) and zeros (z). The relationship between $STF(z)$ and $NTF(z)$ in terms of the implementation network $H(z)$ (Figure 2.8), can be derived as follows:

$$NTF(z) = \frac{(z-z_1)(z-z_2)\dots}{(z-p_1)(z-p_1)\dots} \quad (2.15)$$

$$NTF(z) = \frac{V(z)}{E(z)} = \frac{1}{H(z) + 1} \quad (2.16)$$

giving $H(z)$, the implementation network

$$H(z) = \frac{1}{NTF(z)} - 1 \quad (2.17)$$

Similarly,

$$STF(z) = \frac{V(z)}{U(z)} = \frac{H(z)}{1 + H(z)} \quad (2.18)$$

$$STF(z) = 1 - NTF(z) \quad (2.19)$$

Taking a MOD1 $\Sigma\Delta$ modulator as an example, the first criteria is that the zeros must be placed to null the noise, which means $z_1 = 1 + j0$ (Figure 2.11) and the zero is in the unit circle line $f = 0$ corresponds to a noise null at DC.

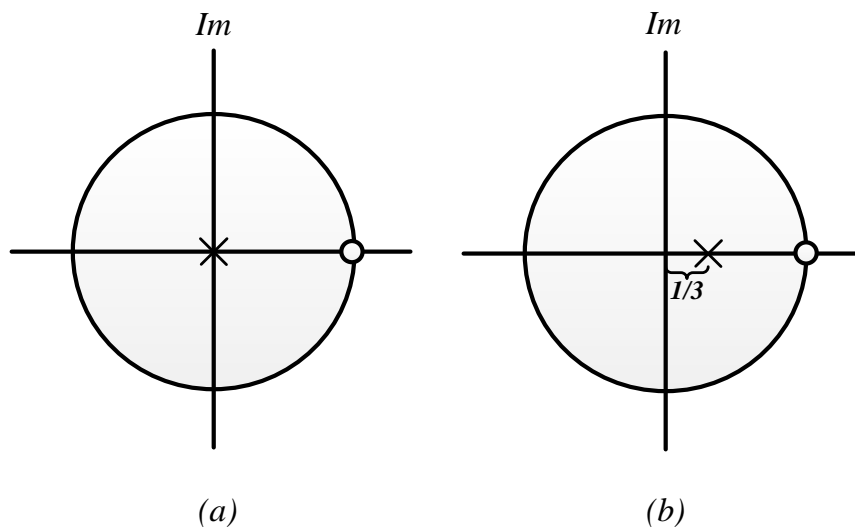


Figure 2.11: (a) The NTF poles MOD1 and (b) the NTF poles MOD1 based on the *Lee criterion*.

Figure 2.11 shows two possible pole positions using the second criteria. Figure 2.11(a) shows the NTF pole for the *basic* MOD1, which is at the origin, giving $\max |H(e^{j\omega})| = 2$. Figure 2.11(b) shows the NTF pole for MOD1 which follows the *Lee criterion* for guaranteed stability. It becomes more important to meet the *Lee* stability criteria at high orders of $H(z)$. The modified *Lee* based MOD1 structure is shown in Figure 2.12. The $NTF(z)$ now can be written based on the general form of Equation 2.15 as

$$NTF(z) = \frac{z-1}{z-\frac{1}{3}} \quad (2.20)$$

In this condition,

$$STF(z) = 1 - \frac{z-1}{z-\frac{1}{3}} = \frac{\frac{2}{3}}{z-\frac{1}{3}} \quad (2.21)$$

and

$$H(z) = \frac{\frac{2}{3}}{z-1} \quad (2.22)$$

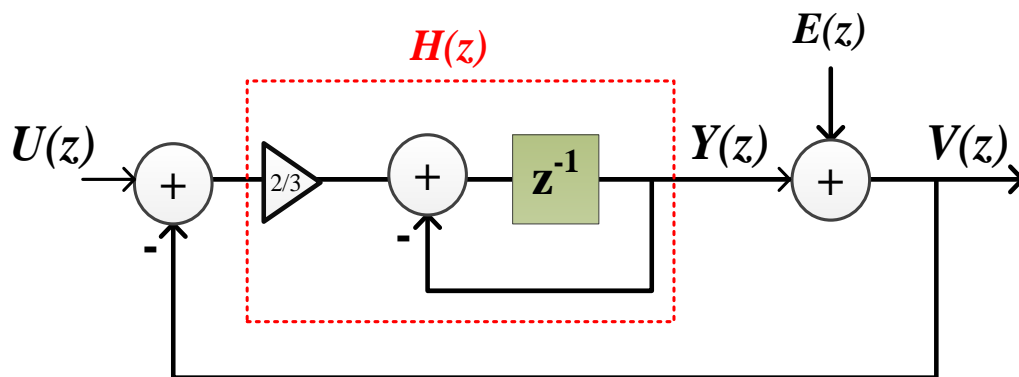


Figure 2.12: The *Lee criterion* based MOD1 $\Sigma\Delta$ modulator.

2.4.5 Band-pass $\Sigma\Delta$ Modulator

A low-pass $\Sigma\Delta$ modulator applies to signals at or near DC. However for most communication systems, signals at radio frequencies are essentially needed. Figure 2.13 shows the linear z -model of a MOD1 based band-pass $\Sigma\Delta$ centred on $\frac{f_s}{4}$. The band-pass NTF characteristic is obtained from the mathematical transformation $z^{-1} \rightarrow -z^{-2}$ [24]. The transfer functions now become

$$NTF(z) = 1 + z^{-2} \quad STF(z) = 1 \quad \text{and} \quad H(z) = -\frac{1}{1+z^2} \quad (2.23)$$

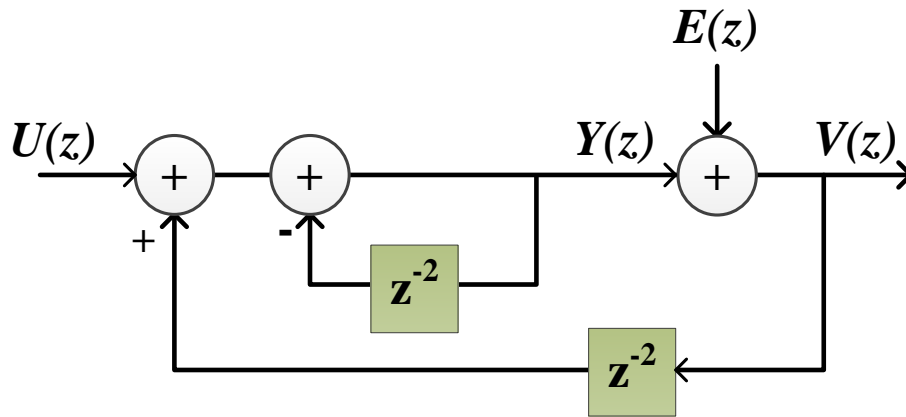


Figure 2.13: A linear z -domain of a band-pass $\Sigma\Delta$ modulator.

It is clearly shown that the number of poles and zeros in the NTF of the low-pass $\Sigma\Delta$ is now doubled. The zeros are rotated in the z -plane into the imaginary axis on the unit circle, from $z = 1 + j0$ to $z = 0 \pm j$, and there are two poles located at the centre of the unit circle, Figure 2.14.

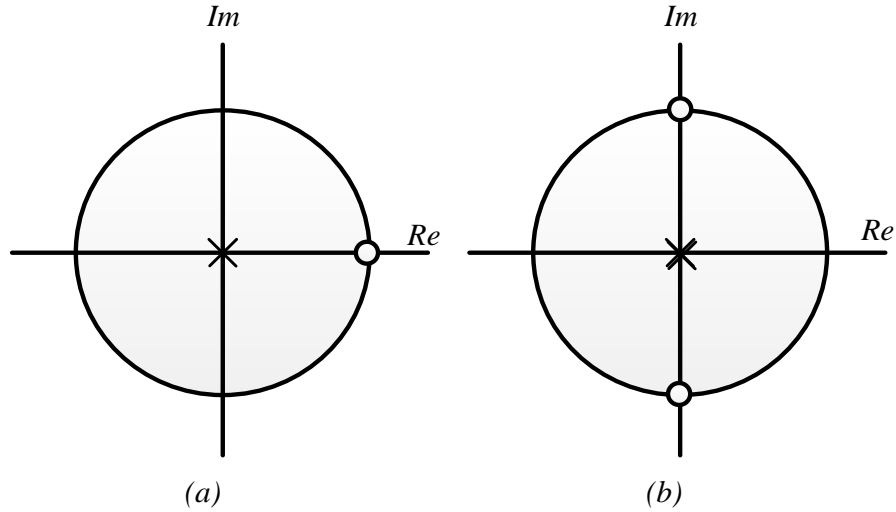


Figure 2.14: Poles-zeros diagram in z -plane of the (a) NTF of low-pass MOD1 and (b) band-pass MOD1.

2.5 Interpolation and Decimation for $\Sigma\Delta$ Modulators

Oversampled $\Sigma\Delta$ modulation is an effective way to build high resolution A/D and D/A converters. However, their highly oversampled digital interface can cause significant processing loads to the connecting DSP circuits unless the sampling rate can be quickly converted to near the *Nyquist* rate, f_N . Therefore, interpolation and decimation filters are required. As long as the signal frequency content is below the *Nyquist* frequency at the lowest sampling frequency, we can decimate the signal or then turn around and interpolate it to recover the original signal without distortion.

For a D/A, the sample rate can be increased from f_N to $f_s = OSR_{BB} \times f_N$ by an integer value using Infinite Impulse Response (IIR) or Finite Impulse Response (FIR) interpolation filters; OSR_{BB} is the oversampling ratio of the baseband. The filter's

principle role is to suppress the spectral replicas centered at $f_N, 2f_N, \dots, (OSR_{BB}-1)f_N$. The frequency representation of the signal (f_{signal}) must be less than half the *Nyquist* rate ($\frac{f_N}{2}$).

For an A/D, decimation is required. Decimation is the process of decreasing the sampling rate, f_s , in a signal processing system. Figure 2.15 shows the standard interpolation and decimation process in a signal processing system. It is common to reduce the word resolution at the higher sample rates to reduce processing load.

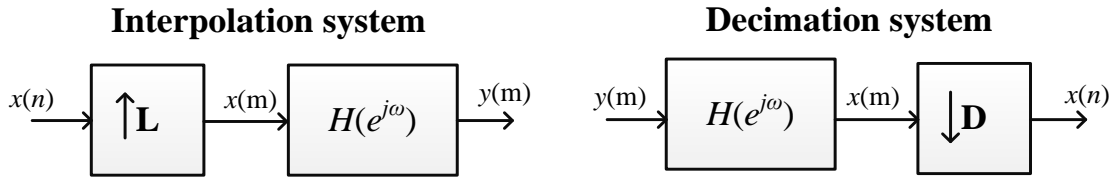


Figure 2.15: Interpolation system (left) and decimation system (right) [62].

The interpolating filter has the frequency domain form [62]

$$Y(e^{j\omega}) = H(e^{j\omega})X(e^{j\omega L}) \quad (2.24)$$

and the decimation filter [62]

$$Y(e^{j\omega}) = \frac{1}{D} \sum_{k=0}^{D-1} H(e^{j(\omega-2\pi k)/D})X(e^{j(\omega-2\pi k)/D}) \quad (2.25)$$

The filter $H(e^{j\omega})$ is usually low-pass, but this need not be the case. If the filter $H(e^{j\omega})$ selects an image of the low-pass BB signal, it can be up-converted to RF (down-converted from RF) without any additional processing. Such a technique can provide the input to a band-pass $\Sigma\Delta$ DAC.

Common filter structures with reduced complexity used in interpolation and decimation are *half-band filters* [63, 64], *comb filters* [65, 66], *CIC filters* [65, 67], and *polyphase filters* [68, 69].

2.6 Coding Efficiency

Coding efficiency, η_p , is defined as the ratio of the reconstructed signal power relative to the total pulse train power [70]

$$\eta_p = \frac{V_{L,rms}^2}{P_A} \quad (2.26)$$

where, $V_{L,rms}^2$ denotes the in-band of a complex signal corresponding to the power recovered after $\Sigma\Delta$ filtering, and P_A is the total power of the output pulse stream.

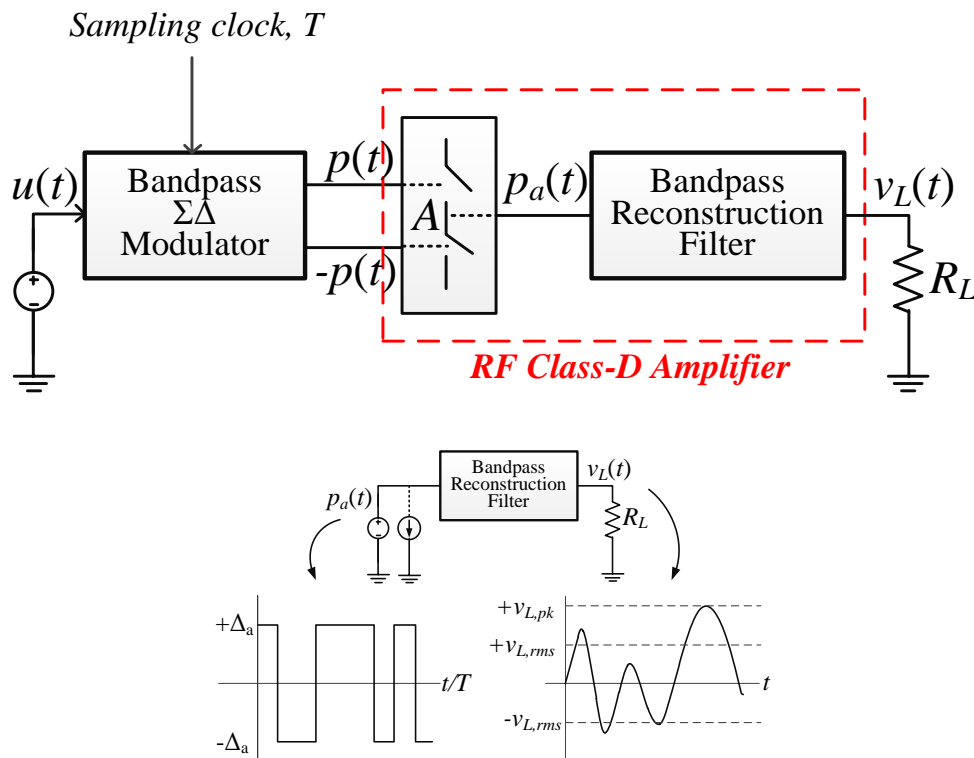


Figure 2.16 : Coding efficiency measurement for band-pass $\Sigma\Delta$ modulator with Class-D amplifier [71].

A coding efficiency measurement is illustrated in Figure 2.16 in [71]. $p_a(t)$ is the input pulse train with amplitude levels $\pm\Delta_a$. The pulse train is filtered with a

reconstruction band-pass filter. P_L is the signal load power into R_L after any out-of-band noise has been filtered away. The total pulse train power is $P_A = \Delta_a^2 / R_L$ for a voltage pulse train (measured without filter). Therefore, the definition of coding efficiency can be written as [71]

$$\eta_p = P_L R_L / \Delta_a^2 \quad (2.27)$$

The coding efficiency as an effective gain can be expressed from Equation 2.27. It relates the amplitude of the load signal to the amplitude of the switched pulse train in the circuit and can be expressed as [71]

$$V_{L,rms} = \sqrt{\eta_p} \Delta_a \quad (2.28)$$

The SMPA then can only provide good coding efficiency when the signal level is high and the modulation PAPR is low.

2.7 Modulation Techniques for Switched PA's

In this section the different approaches to generating the drive signal for SMPA's will be reviewed. There are two fundamental approaches: 'burst-mode' and 'cycle-mode'. More emphasis will be placed on the latter since it is more relevant to this work.

2.7.1 Burst-Mode Modulation

Burst-mode modulation is produced by a square wave which then generates an ON-OFF burst of carrier frequency. This is one of many modulation techniques in SMPA to generate an RF signal with the desired amplitude and phase. As mentioned earlier, the

SMPA is either ON or OFF so the PA is either operating at saturation (its maximum efficiency state) or there is no current following. The square wave's duty cycle is varied depending on the amplitude information of the baseband signal. It is then multiplied with an RF carrier. The PA output passes through a BPF which smooths out the bursts to give an RF carrier of the desired amplitude (Figure 2.17) [72]. The amplitude is given by the duty cycle, $\delta_b = \frac{T_{on}}{T_b}$ where T_{on} is the ON time and T_b is burst period. Note $f_b = \frac{1}{T_b} =$ burst repetition rate.

Burst-mode techniques generate distortion products that occur on every harmonic of the burst repetition frequency, f_b . These products can fold back in-band reducing the fidelity of the output signal.

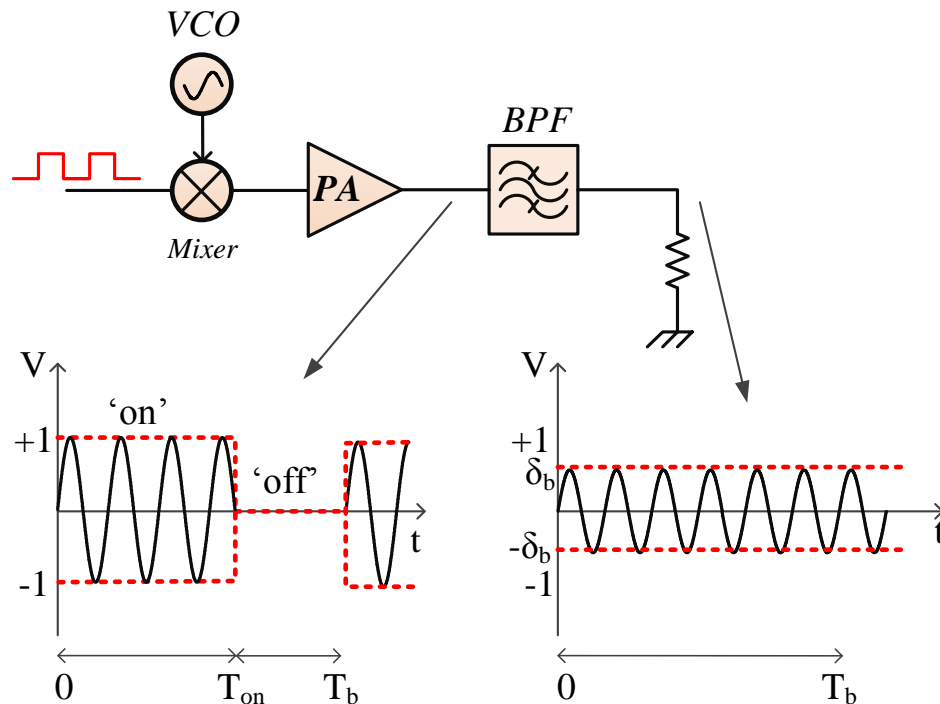


Figure 2.17: Burst-mode operation [72].

Burst-mode techniques using a multistage Doherty design produced high power efficiency in the RF transmitter and reduced out-of-band distortions [73]. Moreover, Hausmair *et al.* in [74] proposed a burst-mode technique that is free from destructive aliasing distortion. However, both of the described transmitter architectures above still use some analog components such as the RF Voltage-Controlled Oscillator (VCO) and upconversion mixer.

Other variations on the burst-mode technique include using a square instead of sinusoidal carrier [75] using a high level modulator operating on the PA, where the digital ON-OFF signal directly switches the supply to the PA [29, 47, 76]. Also the generation of the ON-OFF burst-mode control waveform can take many forms, including triangle wave generated PWM [73, 74] and $\Sigma\Delta$ techniques [77].

In general all burst-mode schemes suffer from bandwidth restrictions caused by the burst repetition rate, which should be much less than carrier frequency ($f_b \ll f_c$) and much greater than signal bandwidth ($f_b \gg B_w$). Despite these drawbacks they have good coding efficiency and can be implemented with medium speed logic.

2.7.2 Cycle-Mode Modulation

Burst-mode modulation varies the duty cycle of the carrier bursts, whereas cycle-mode varies the carrier waveform itself on a cycle-by-cycle basis. The carrier cycles are generally of a square shape enabling variations in pulse width, position and sometimes even amplitude as described in Figure 2.18. A band-pass filter recovers the original sin wave shape.

Cycle-mode modulation requires the clock frequency, f_{clock} , to be higher than the carrier frequency, f_c , to enable the generation of different pulse widths. There are three major approaches: band-pass $\Sigma\Delta$ with the nominal RF carrier frequency, $f_c = \frac{f_{clock}}{4}$ [78]; Cartesian low-pass $\Sigma\Delta$ with quadrature up-conversion to $f_c = \frac{f_{clock}}{4}$ [61]; and Cartesian filtered polar-quantised conversion with $f_c = \frac{f_{clock}}{(4 \times 2^i)}$ where the integer $i \geq 0$ [79].

Sjöland *et al.* in [29] developed a system model to generate an appropriate binary signal where the pulse width represents the amplitude of the RF signal and the pulse position represents the phase of the RF signal. The pulse width and pulse position are quantised to a number of fixed values (Figure 2.18). Compared to the burst-mode technique, less band-pass filtering is required to remove out-of-band noise and distortion. One advantage is the compatibility with synchronous digital design because it uses a regular clock timing grid. Digital circuits usually work best when they are synchronous. All the internal processing blocks change state under the control of an external clock. This quantisation in time forces the pulse edges to be on a regular clock timing grid which causes the generation of quantisation noise.

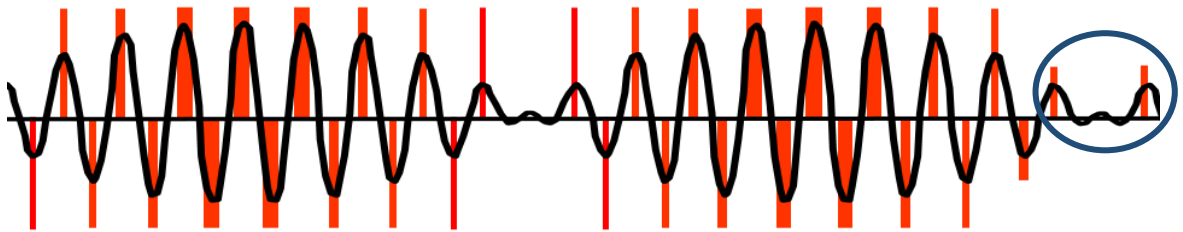


Figure 2.18: PWM of RF carrier, with supply modulation included (circle) [29].

RF pulse generation with pulse width modulation is compatible with switched-mode transmitter architectures. A novel all-digital approach for generating a pulse train suitable for switch-mode power amplifiers was proposed by Bassoo *et al.* [76]. It shows better adjacent channel noise performance than traditional band-pass $\Sigma\Delta$ scheme with a 1-bit drive signal. The concept makes RF PWM/PPM topologies feasible for GHz frequencies enabling their use in many wireless applications. Cycle-mode modulation, which can be obtained by using all digital techniques, will be the preferred modulation technique in this thesis.

2.8 $\Sigma\Delta$ Modulator Architecture

Recent research is now applying $\Sigma\Delta$ techniques to band-pass signals such as those found in radio frequency transceivers [80]. There are a number of challenges to developing such schemes. First, the carrier frequency is of the same order as the sample rate; secondly the bandwidth, EVM and spectral mask of any transmitted RF signal must be met; and thirdly, any design must be realisable in today's silicon technology. These three factors are all inter-related and form a complex trade-off between performance, complexity and energy consumption. This thesis concentrates on all-digital upconverter structures. The binary nature of their output removes the need for analog components in the up-conversion chain. Their outputs can be used directly to drive the SMPA (Class-S or Class-D) for high-efficiency operation [78].

2.8.1 Band-pass $\Sigma\Delta$ Architecture

Band-pass $\Sigma\Delta$ modulator is proposed as a possible solution suitable for RF digital transmitter design using SMPA. A band-pass $\Sigma\Delta$ modulator generates a digital pulse train and shapes the quantisation noise which is then fed to the switched amplifier.

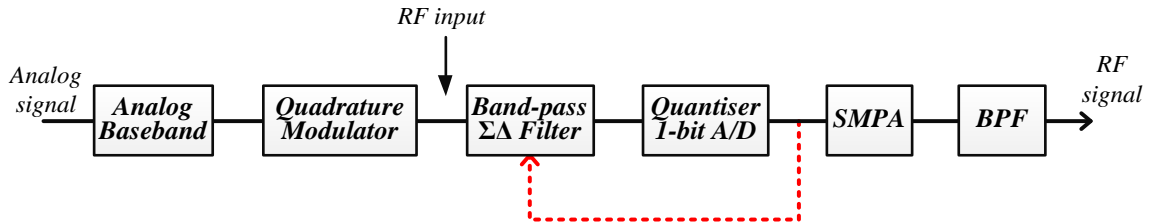


Figure 2.19: Band-pass $\Sigma\Delta$ architecture in [78].

In the band-pass $\Sigma\Delta$ modulator structure in [78], the sampling frequency is four times the required RF carrier frequency ($f_c = \frac{f_{clock}}{4}$), Figure 2.19. The quadrature modulation block upconverts the baseband signal to the RF carrier. The band-pass $\Sigma\Delta$ filters are implemented in analog and the 1-bit A/D generates the digital input signal to the SMPA. One problem is that the output signal can have more than one pulse per half period of the RF carrier. This can potentially increase switching losses since the output goes directly to the SMPA. A BPF is used to remove the noise and switching harmonics, leaving the required RF output as shown in Figure 2.20.

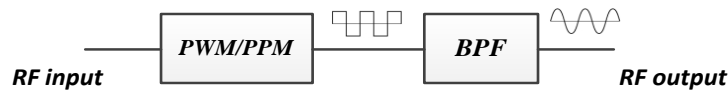


Figure 2.20: BPF for RF PWM/PPM output.

It is possible to avoid the analog processing by doing the up-conversion in DSP and replacing the band-pass $\Sigma\Delta$ 1-bit A/D with a band-pass $\Sigma\Delta$ 1-bit D/A as shown in Figure 2.21 [81]. The DSP module generates the input signal as an I and Q baseband signal. The I - Q baseband is interpolated to a higher sampling frequency before digital up-conversion. The up-conversion operation multiplies the I - Q baseband signals with the pulse sequences of $1,1,-1,-1,\dots$ and $-1,1,1,-1,\dots$ respectively. The two signals are summed together and fed directly into the band-pass $\Sigma\Delta$ modulator, which generates the digital data streams for the SMPA. The band-pass $\Sigma\Delta$ transmitter architecture operates at a sampling frequency that is four times the RF carrier frequency. The high clock rate will require additional power consumption since each signal transition involves a capacitive $(\frac{1}{2} CV^2)$ energy loss, which reduces efficiency [82].

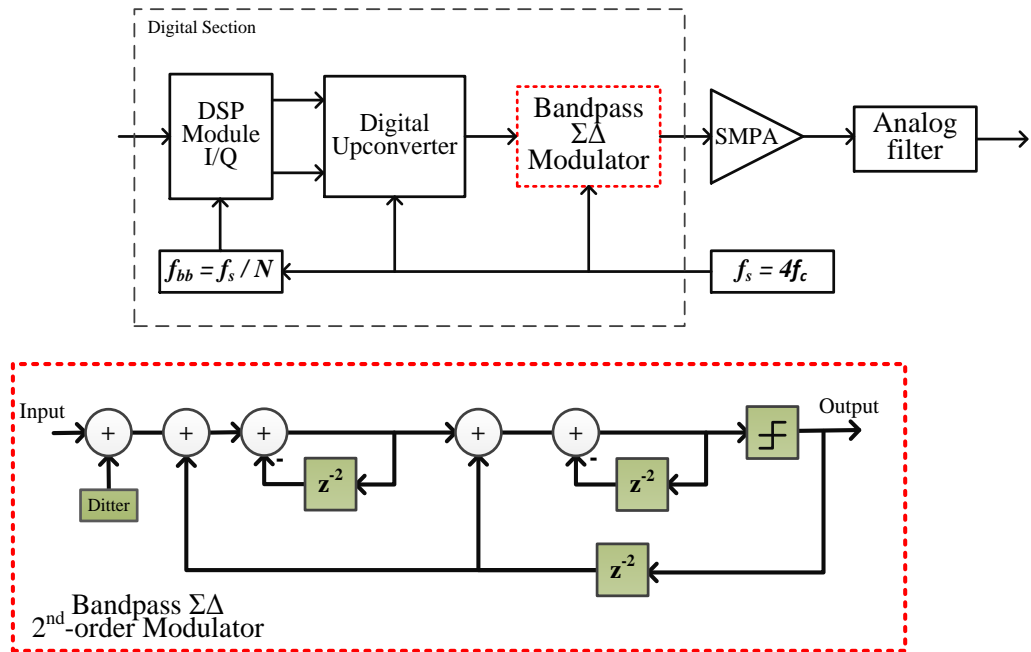


Figure 2.21: The band-pass $\Sigma\Delta$ (2^{nd} -order) architecture proposed in [81].

A digital method proposed in [61], implements the band-pass $\Sigma\Delta$ technique using a combination of two low-pass $\Sigma\Delta$ modulators and upconverters, as shown in Figure 2.22. Each baseband I and Q signal has its own low-pass $\Sigma\Delta$. The three multiplexer units (Mux) implement a quadrature modulator that up-converts the quantised one bit $\hat{I}-\hat{Q}$ signals to RF at a carrier frequency f_c .

$$y_{RF}(n) = \hat{Q} \sin\left(2\pi n \frac{f_c}{f_{clock}}\right) + \hat{I} \cos\left(2\pi n \frac{f_c}{f_{clock}}\right) \quad (2.29)$$

when $f_{clock} = 4f_c$ the above sequences become

$$\sin\left(2\pi n \frac{f_c}{f_{clock}}\right) = 0, 1, 0, -1, 0, 1, \dots \quad (2.30)$$

$$\cos\left(2\pi n \frac{f_c}{f_{clock}}\right) = 1, 0, -1, 0, 1, 0, \dots \quad (2.31)$$

The summation of the sequences is trivial and can be performed in a multiplexer, since one term is always 0.

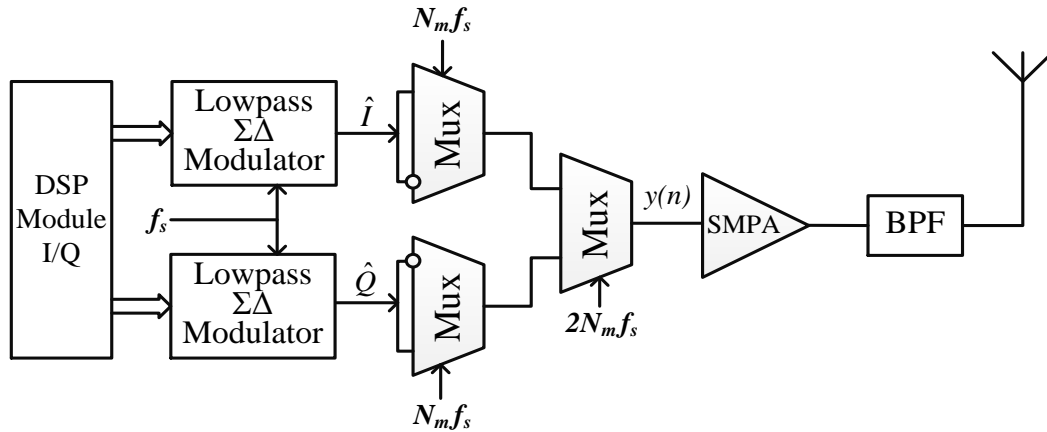


Figure 2.22: The band-pass $\Sigma\Delta$ (two low-pass $\Sigma\Delta$ s) architecture proposed in [61].

It is possible to generate RF signals with carrier frequency $f_c > 1$ GHz using off-the-shelf multiplexer devices. However it is harder to achieve GHz sample rates (f_s) for the DSP and $\Sigma\Delta$ modulators without resorting to Application-Specific Integrated Circuit (ASIC) implementation [83]. The achievable bandwidth is proportional to f_s .

It is difficult to get high sampling rates on the $\Sigma\Delta$ D/A's because of the feedback path. The filtering and quantisation must all be completed within the latency of one clock period. Frappé *et al.* [84] developed an ASIC using Borrow-Save arithmetic, non-exact quantisation and a multiphase-clock to complete all calculations of a 3rd order $\Sigma\Delta$ filter in 250 ps (pico second). A signal bandwidth of 50 MHz was obtained.

2.8.2 Polar $\Sigma\Delta$ Architecture

Polar $\Sigma\Delta$ techniques operate on the polar (amplitude $A(t)$ and phase $\Phi(t)$) signals rather than the more normal I - Q representation. The polar $\Sigma\Delta$ structure was proposed in [77, 85-87] where the aim was to reduce the switching activity and also to eliminate the need for analog components.

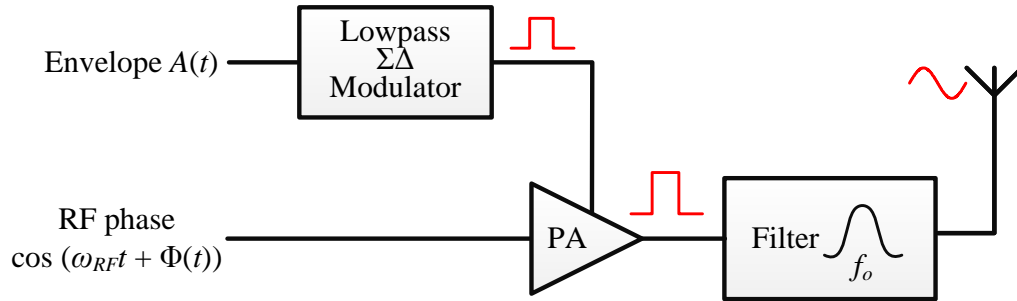


Figure 2.23: The polar $\Sigma\Delta$ based burst-mode architecture proposed in [77].

Figure 2.23 shows a polar $\Sigma\Delta$ architecture consisting of a low-pass 1-bit $\Sigma\Delta$ modulator using a phase modulated clock and a gated PA [77]. The envelope input signal $A(t)$ represents the average value of the ON-OFF period of the square wave signal at the output of the low-pass $\Sigma\Delta$ modulator. The phase information is represented by the zero-crossing timing of the RF carrier. The PA is operated in saturated mode (for best

performance with a Class-C structure [88]), and the input waveforms are square waves. This scheme implements burst-mode modulation where the $\Sigma\Delta$ modulator switches the square wave RF input signal ON or OFF [77].

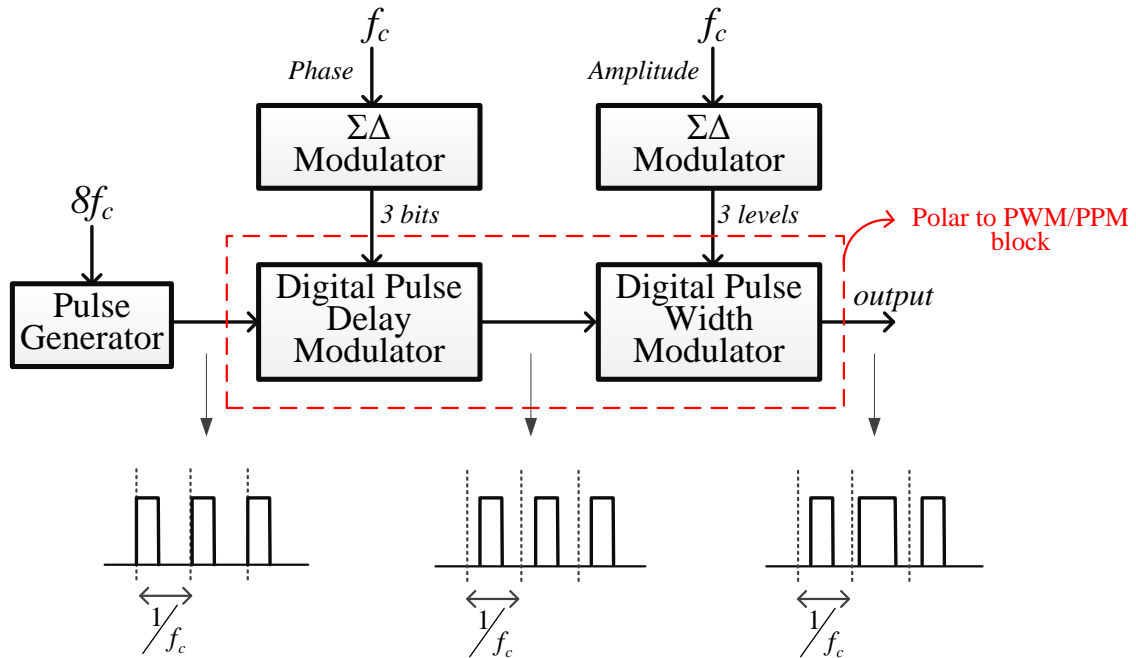


Figure 2.24: The polar $\Sigma\Delta$ architecture proposed in [86].

Keyzer *et al.* in [86], the architecture consists of the two $\Sigma\Delta$ modulators (each modulator generates a pulse train representing the phase and amplitude signals respectively), followed by up-conversion blocks to perform PWM and PPM generation, Figure 2.24. The amplitude is quantised into three levels and the phase is quantised into eight levels. A digital pulse delay modulator acts on an input periodic pulse train with period of f_c and pulse width $\frac{1}{8f_c}$ to produce an output phase modulated pulse train. This is then followed by a pulse expander to change the phase width. The structure limits the number of pulses per period to one and there is often no switching pulse when the input

signal is small. Therefore, it should have good efficiency; however there is a bandwidth penalty.

Bassoo *et al.* in [87] investigated the polar $\Sigma\Delta$ structure which is shown in Figure 2.25. The input signal of I - Q complex baseband is converted to polar representations, $R = \sqrt{I^2 + Q^2}$ and $\theta = \tan^{-1}\left(\frac{Q}{I}\right)$. Low-pass $\Sigma\Delta$'s are used to independently quantise the R (amplitude) and the θ (phase) signals respectively. The R value is quantized into 4 distinct levels while θ is quantized to 16 levels uniformly distributed between 0 to 2π . The output of these quantisers is fed back to their appropriate $\Sigma\Delta$ filter. The quantized signal is also passed through a 'Polar to PWM/PPM' block converter to generate the appropriate pulse waveform. The pulse train output of the 'Polar to PWM/PPM' block feeds to the SMPA and BPF.

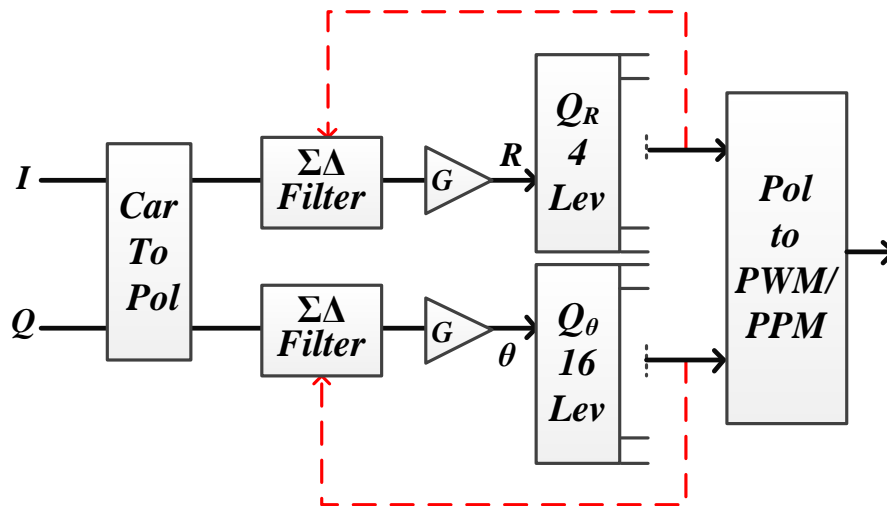


Figure 2.25: Polar $\Sigma\Delta$ Architecture proposed in [87].

Normally, the $\Sigma\Delta$ filters update the pulse width and position every whole number of cycles of the carrier frequency (or half cycles if a bridge amplifier is used). The $\Sigma\Delta$ filters for the phase signal must be modified to handle the phase wrap-around. The polar

components have a wider bandwidth than the I - Q components, and this limits the modulation bandwidth of this structure hence the effective oversampling rate is reduced. Besides that, the conversion process of I - Q complex baseband from Cartesian format to polar format is a nonlinear process which causes some of the quantisation noise to fold back into the band of interest and hence it cannot be filtered out [31].

Another problem is unwanted spectral components which arise when baseband polar signals are upconverted to RF using PWM/PPM techniques. The ‘Polar to PWM/PPM’ block upconverts the signal to RF with quantised amplitude and phase. The amplitude of the RF is controlled by the pulse width and the phase of the RF is controlled by the pulse position. In the PPM process, a change in phase is represented by a change in position and the pulse edge must occur on the digital timing grid. This process eventually leads to amplitude modulation (AM) as a pulse is swallowed whenever there is a change in quantisation level. Recently, Bassoo *et al.* in [87] has established that the dominant distortions are the image and harmonic components generated in the PPM circuit (‘Polar to PWM/PPM’ block).

2.8.3 Cartesian $\Sigma\Delta$ Architecture

The authors in [76, 89] realised that Cartesian $\Sigma\Delta$ upconverters are an improvement over the polar $\Sigma\Delta$ modulator in [87], with regard to solving the bandwidth expansion problems and reducing switching activity. Figure 2.26 shows the comparison plot between polar and Cartesian $\Sigma\Delta$ s using an OFDM signal. The output spectrum and ACP versus signal level are compared. The Cartesian $\Sigma\Delta$ has better noise shaping with a better null around the band of interest and lesser noise than the polar $\Sigma\Delta$ (Figure 2.26(a)).

Figure 2.26(b) shows the Cartesian $\Sigma\Delta$ has at least 10 dB less ACP, over a wide dynamic range of input signal levels, compared to the polar $\Sigma\Delta$.

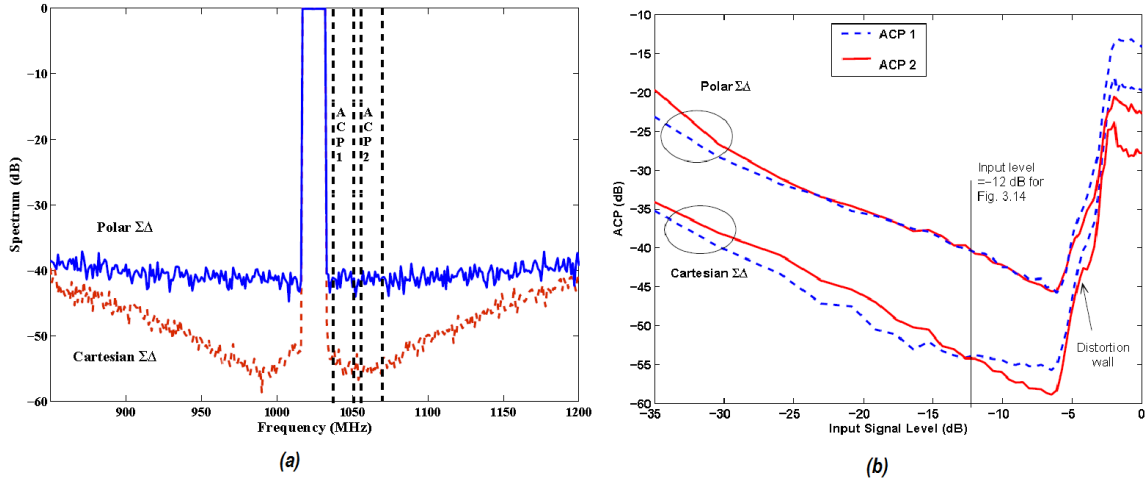


Figure 2.26: (a) Normalized spectrum of OFDM and (b) ACP for Cartesian $\Sigma\Delta$ and polar $\Sigma\Delta$ modulator [76].

The proposed Cartesian $\Sigma\Delta$ structure can be seen in Figure 2.27. It consists of MOD2 low-pass $\Sigma\Delta$ s [24] for the Cartesian I and Q input signals. After $\Sigma\Delta$ -filtering, the I and Q signals are then converted to polar co-ordinates $[R, \theta]$ and separately quantised in the Q_R and Q_θ blocks resulting into $[\hat{R}, \hat{\theta}]$. The Gain block (normally set to $G \leq 1$) works to improve efficiency (by reducing the number of switching edges) at the expense of a degraded spectrum [29]. The output of the quantisers is converted back to Cartesian co-ordinates, $[\hat{I}, \hat{Q}]$ (removing bandwidth expansion [29]) and fed as feedback to the $\Sigma\Delta$ filters. The outputs of both quantisers are also upconverted to RF using PWM/PPM techniques in the ‘Polar to PWM/PPM’ block.

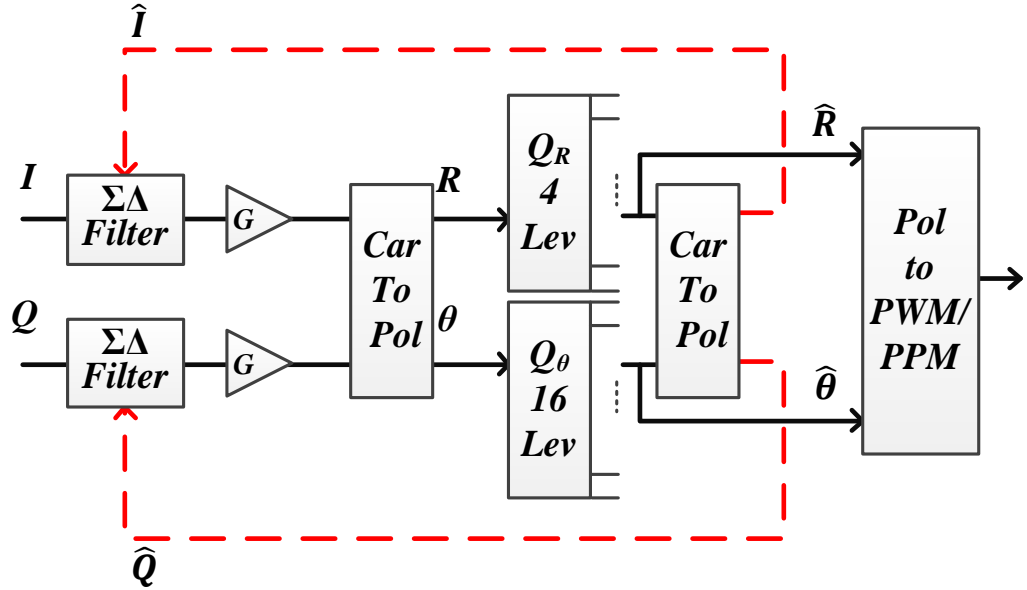


Figure 2.27: Cartesian $\Sigma\Delta$ Architecture [79]. $\Sigma\Delta$ filtering is in Cartesian with quantisation in polar.

The proposed quantiser used an even quantisation technique where the three-level-waveform at the output is based on pulses with an even number of clock periods [32, 76, 79]. The quantised amplitudes, \hat{R} , of the RF signal are calculated by changing the pulse widths in increments of two clock periods. However, this leads to a potential coarse quantisation at low signal levels, as the minimum pulse width in the even quantisation scheme is two clock periods.

Furthermore, while reducing the bandwidth expansion, the Cartesian $\Sigma\Delta$ model may still cause unwanted spectral components due to the ‘Polar to PWM/PPM’ block. The most relevant work to the aims of the proposed research was presented in [79]. It showed that in a single carrier environment, an increase in offset frequency increases the unwanted spectral components. The image and 3rd order harmonic components are the dominant distortions. The PPM block was shown to be responsible for these distortions, but no solutions were proposed.

2.9 RF Tuning

All the schemes so far require the carrier frequency (f_c) to be harmonically related to the clock frequency (f_{clock}). The almost universal choice is $f_{clock} = 4f_c$. Tuning of the carrier requires changing the clock frequency. Small offsets in f_c can be accommodated by a slow rotation of the I - Q input signal, but this generates an unwanted spectral component. Bassoo *et al.* in [79] mathematically showed that a Single Side Band (SSB) modulated tone causes an unwanted image and 3rd-order distortion products. Such unwanted signals can cause jamming to the other users of the spectrum. More recently, Routsalainen *et al.* in [90] showed that larger frequency offsets caused image noise to fold in-band (Figure 2.28). A solution using complex noise shaping filters was proposed for both moving the main noise null and suppressing the image noise. Later, a second solution using a fractional delay in the feedback path was also suggested [91].

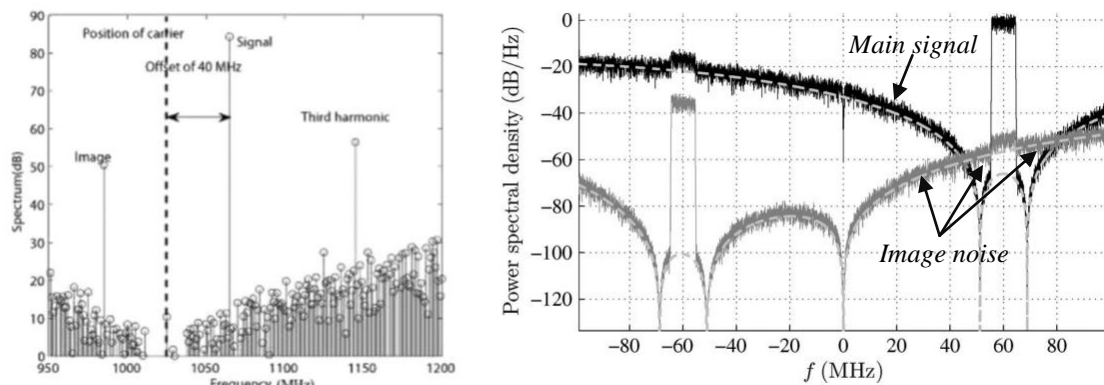


Figure 2.28: SSB output spectrum from a Cartesian $\Sigma\Delta$ with the distortions from the PWM/PPM with image and 3rd harmonic (right) [79], and the conjugate quantisation noise folding in the frequency domain (left) [90].

In this thesis further solutions will be proposed to the problem of baseband tuning. Using the work by Bassoo *et al.* [79], one possible solution is to introduce digital pre-distortion and post-distortion based on the signal conjugate. The research in this thesis will focus on methods to eliminate noise and distortion products.

2.10 Summary

In this chapter, a brief analysis of PA design has been carried out. Since the goal of the proposed architecture scheme is for an all-digital transmitter scheme, the discussion of switching amplifier operation is complementary. Basic $\Sigma\Delta$ concepts are presented. These include system modulation techniques, STF, NTF, poles, zeros, interpolation, decimation, and coding efficiency. The ‘burst-mode’ and ‘cycle-mode’ versions of digital RF transmissions were then discussed. A more detailed study was then made of the three dominant switched-mode transmitter architectures: band-pass, polar and Cartesian $\Sigma\Delta$. The scheme used in this thesis is based on the Cartesian $\Sigma\Delta$ upconverter. The problem of distortion and noise generation in baseband tuned architectures was flagged, and some solutions to the problem will be presented in later chapters.

In the next chapter, the first technical part of the thesis, the existing Cartesian $\Sigma\Delta$ upconverter is modified with an improved quantisation scheme. The scheme is more suited to low power signals which are more prevalent in today’s high PAPR modulations.

Chapter 3

Proposed Polar Quantisation Scheme

3.1 Introduction

After studying different schemes for the $\Sigma\Delta$ transmitter architecture, the existing Cartesian $\Sigma\Delta$ structure, as shown in Figure 2.27, is chosen as a potential candidate for future wireless base stations. The output of the architecture produces a three-level waveform, Figure 2.5, with low switching activity thus reducing the power loss in the SMPAs. The RF pulse train waveform, as shown in Figure 2.18, has reduced second and even order distortions, improved coding efficiency, and can derive SMPAs in a bridge structure. The main focus of this study is in the waveform generation in the ‘Polar to PWW/PPM’ block. The previous technique in [79] used an even number of clock periods to generate the pulse width and alter it by adding (or subtracting) a clock period to (or

from) each edge, to maintain the pulse centre-of-gravity. This technique is called even quantisation.

This chapter offers the alternative approach of using odd quantisation instead of the previously used even quantisation of [32, 76, 79, 87]. Odd quantisation is proposed to reduce the possible pulse widths by one clock period while maintaining a constant phase reference. The acceptable pulse widths become (0, 1, 3, 5 ...) for the odd quantisation compared to the (0, 2, 4, 6 ...) values for the even quantisation. In the even quantisation technique, the three-level-waveform at the output is based on pulses with an even number of clock periods. The quantised amplitudes, \hat{v}_r , of the RF signal are calculated by changing the pulse widths in increments of two clock periods. This leads to a potential coarse quantisation of low level signals as the minimum pulse width in the even quantization scheme is two clock periods. In both cases the phase reference does not change with the pulse width, allowing separate quantisers for amplitude and phase. The evaluation of the adjacent channel interference caused by the quantisation process in the $\Sigma\Delta$ architecture will be discussed. Later, a Cartesian $\Sigma\Delta$ upconverter with joint quantisation will be considered. It is shown that a trade-off exists between the RF oversampling factor OSR_{RF} and the fidelity of the quantiser.

Section 3.2 presents the Cartesian $\Sigma\Delta$ upconverters. Section 3.3 gives details of the new odd quantisation scheme with its performance compared to the even quantisation scheme. Section 3.4 discusses a joint quantisation odd-even scheme. Section 3.5 presents the baseband RF tuning. Section 3.6 gives the simulation setup and results. Section 3.7 describes the experimental measurement setup and results. Finally, we draw a summary in Section 3.8.

The work in this chapter has been presented at some conferences with full reviewed papers entitled: “Odd-even quantisation and Cartesian delta-sigma ($\Delta\Sigma$) Upconverters for Transmitter Design” at the *IEEE International Communication Systems Conference* in 2012 [92]; “OFDM performance with odd-even quantisation in Cartesian $\Delta\Sigma$ upconverters” at the *IEEE International Signal Processing and Communication Systems Conference* in 2012 [93]; and “Joint Odd-Even Quantisation in Cartesian Delta-Sigma Upconverters” at the *IEEE International AFRICON Conference* in 2013 [94].

3.2 Cartesian $\Sigma\Delta$ Upconverters

Polar $\Sigma\Delta$ modulators were introduced by Keyzer *et al.* [86] to generate a pulsed square waveform with a number of quantised pulse widths and pulse positions to control amplitude and phase respectively. It is important to limit the number of edges in the waveform to two per period of the RF carrier, since each edge represents power loss in any subsequent amplifying stage. The polar $\Sigma\Delta$ did this by converting the digital baseband signals to polar and then using the $\Sigma\Delta$ filters to quantise the amplitude and phase components separately. The problem with the scheme is the high noise floor caused by passing the bandwidth expanded polar signals through the $\Sigma\Delta$ filters. A partial solution to the problem involved using Cartesian signals in the $\Sigma\Delta$ filters and polar signals in the quantiser. This improved the spectral performance, but at the expense of a rectangular to polar conversion inside the $\Sigma\Delta$ loop [76]. The structure is shown in Figure 3.1.

$\Sigma\Delta$ techniques in this structure were used to shape the noise away from the band of interest. Upconverters operate by subtracting the current quantised error signal from

the subsequent sample and $\Sigma\Delta$ modulation is achieved through the processes of oversampling and noise shaping. Oversampling reduces the noise PSD as it spreads the noise over a wider bandwidth. As expected, increasing OSR will decrease the in-band noise proportional to $\frac{1}{OSR}$. The oversampling ratio of the baseband (OSR_{BB}) is given by

$$OSR_{BB} = \frac{f_s}{f_B} \quad (3.1)$$

where f_B is the maximum signal bandwidth and f_s is the sampling frequency. The quantisation error is also noise shaped using feedback in the $\Sigma\Delta$ filter. The NTF for MOD2 is given by $(1 - z^{-1})^2$.

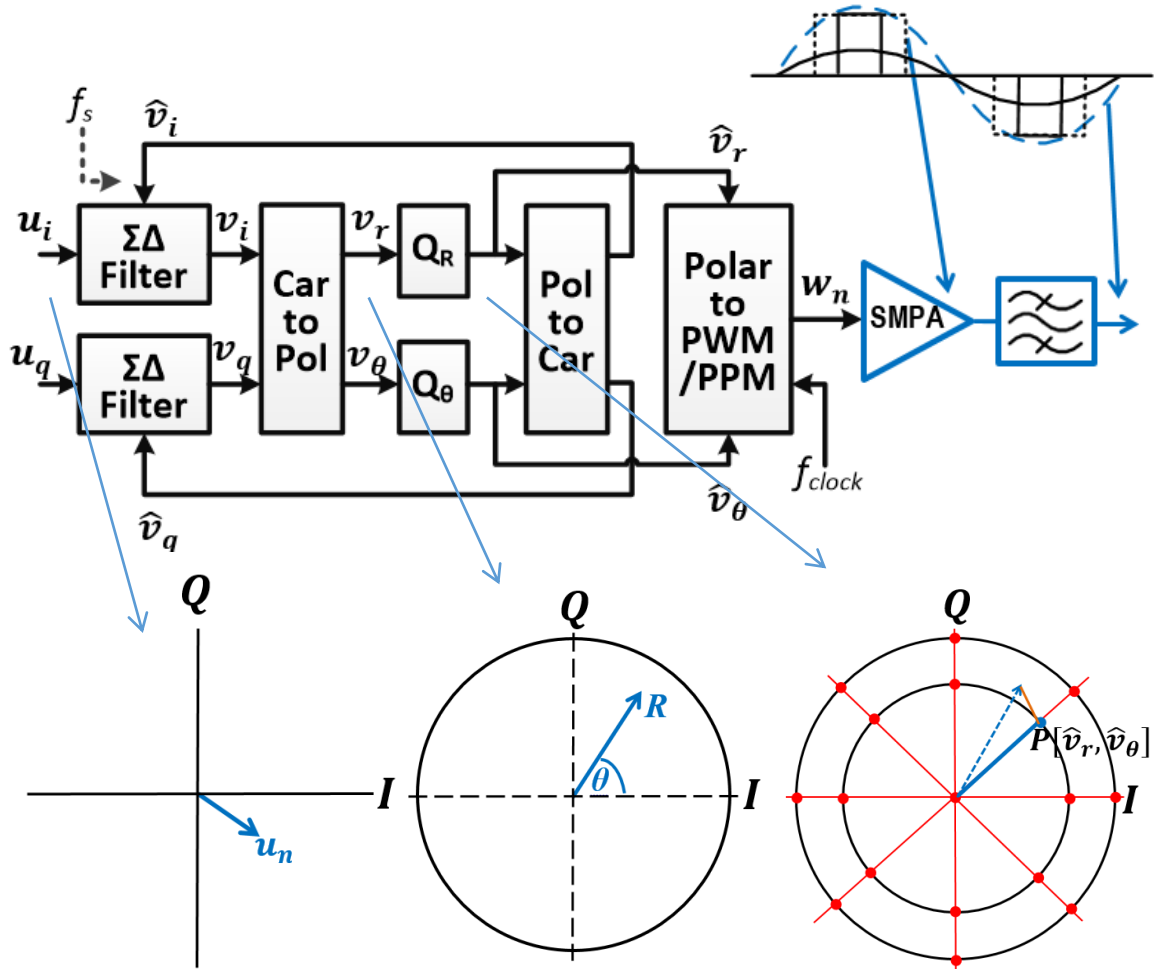


Figure 3.1: Cartesian $\Sigma\Delta$ with polar quantisation showing signals at different points. The two quantised sinusoidal amplitudes and pulse widths are shown top right.

The Cartesian $\Sigma\Delta$ upconverters structure consists of two second-order low-pass $\Sigma\Delta$ (MOD2) for the Cartesian I and Q input signals (see Figure 3.1). After $\Sigma\Delta$ filtering, the I and Q signals are converted to polar coordinates $[v_r, v_\theta]$ and separately quantised in the Q_R and Q_θ blocks. The output of the quantisers $[\hat{v}_r, \hat{v}_\theta]$ is converted back to Cartesian format and fed back to the $\Sigma\Delta$ filters. Moreover, the quantised amplitude, \hat{v}_r , and phase, \hat{v}_θ , that are in polar format are fed to the switching power amplifier in PWM/PPM format (see Figure 3.2 for an example output waveform w_n). A band-pass filter at the output of the SMPA reconstructs the sinusoidal RF signal. SMPAs can use binary input signals or tri-state input signals if a full-bridge structure is employed [31] (see Section 2.3.5). Tri-state will remove the even harmonics.

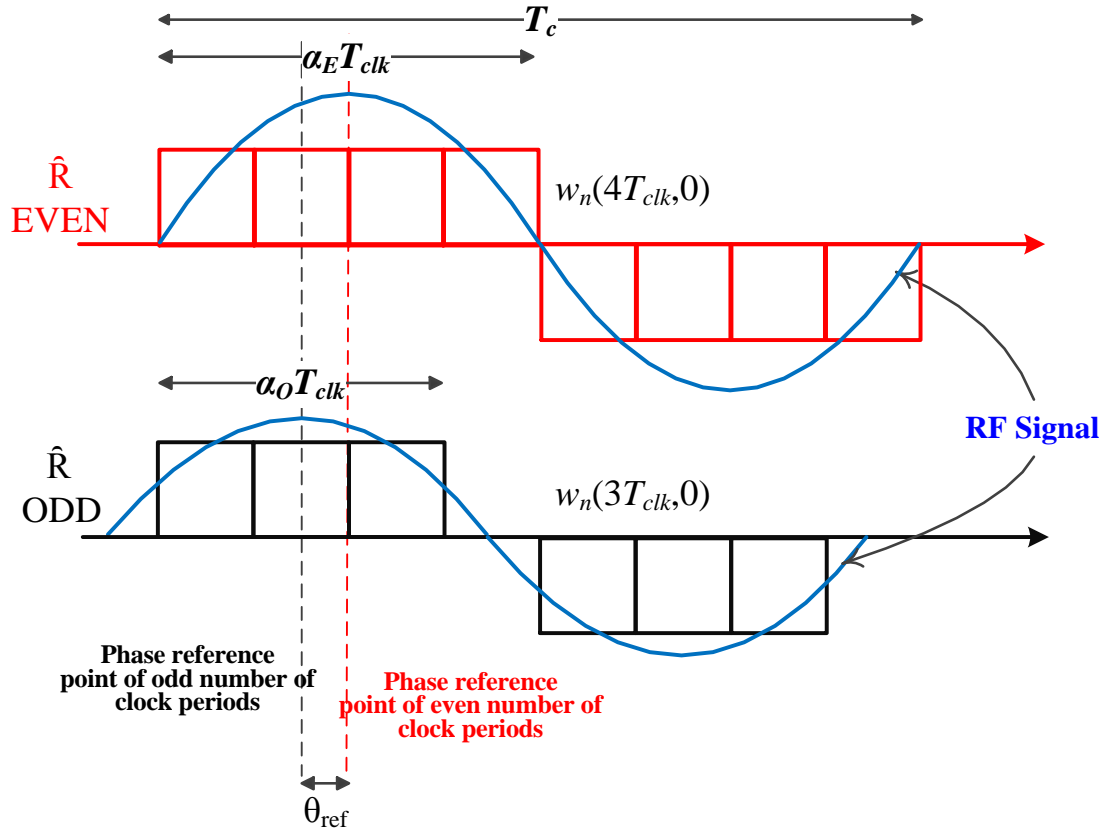


Figure 3.2: The PWM/PPM output for $OSR_{RF} = 8$. Note, a two level signal version would set the negative pulses to zero.

3.3 Odd Quantisation and Even Quantisation

The PWM/PPM process requires the digital clock (f_{clock}) to oversample the nominal RF carrier frequency (f_c) of the signal output by a factor of OSR_{RF} . The OSR_{RF} is given by

$$OSR_{RF} = \frac{f_{clock}}{f_c} \quad (3.2)$$

The number of quantisation levels, N_p , is a function of the OSR_{RF} , or the number of clock cycles per period of the RF carrier ($N_p = OSR_{RF}$). The amplitude and phase of the switching waveform can be updated in half-period increments of the RF carrier giving the sample rate, f_s , of the $\Sigma\Delta$ filters which is defined by

$$f_s = \frac{2f_c}{i} \quad (3.3)$$

where $i \geq 1$ is a positive integer. Normally i is much greater than one because of the difficulty of making high speed $\Sigma\Delta$ filters.

The quantised amplitude levels, N_A , are given by the amplitude of the fundamental sinusoidal component of the repeating pulsed waveform. There are N_A (see Equation 3.6) different possible amplitudes. For the case where $OSR_{RF} = 8$, these amplitudes correspond to pulse widths of 0, 1, 2, 3 and 4 clock periods; the latter two waveforms are shown in Figure 3.3. It is noticeable in Figure 3.2 that a change in carrier amplitude can be accompanied by a change in phase reference (θ_{ref}) of half a clock period. This makes quantisation difficult and so previous work has restricted the amplitude quantisation levels to pulse widths that are either an even number of clock periods or an odd number of clock periods because the phase reference does not change [17]. In the above example, this would give pulse widths of either 0, 1, 3 or 0, 2, 4 clock

periods. Figure 3.2 is an example of the waveform PWM/PPM output corresponding to an even $w_n(4T_{clk}, 0)$ or odd $w_n(3T_{clk}, 0)$ number of clock periods at $OSR_{RF} = 8$.

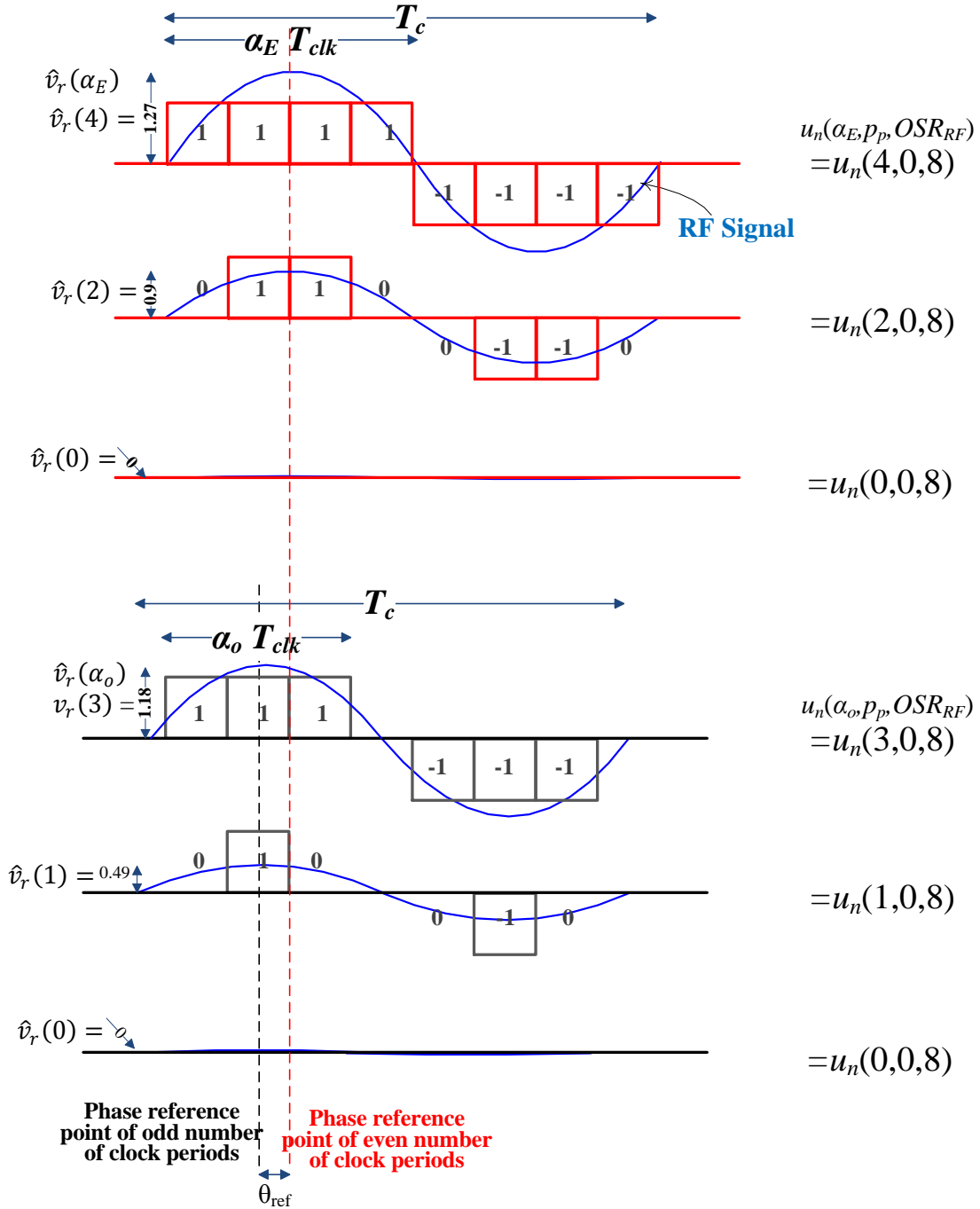


Figure 3.3: Quantised amplitude of the RF carrier $\hat{v}_r(\alpha)$ for even and odd pulse widths ($OSR_{RF} = 8$). α_E, α_o define the pulse width and p_p defines the pulse position.

The phase is therefore uniformly quantised into a number of phase quantised levels of N_p increments over the range 0 to 2π . The quantised phase, \hat{v}_θ , is determined by the pulse position. The quantised amplitude, \hat{v}_r , is determined by the pulse width as shown in Figure 3.3. The top trace shows the maximum amplitude condition for $OSR_R = 8$. The output is a full square wave and, after band-pass filtering, produces the sinusoidal output. The second trace down shows a reduced amplitude sinewave caused by the reduced pulse widths of the three-level waveform. The third trace shows the zero amplitude sinewave. The $\Sigma\Delta$ filter cycles the output between these three quantised states to generate any specified amplitude of the RF signal.

In Figure 3.3, the top three traces show pulse widths that contain an even number of clock periods, and the bottom three traces show the odd sized pulse widths. The phase reference, θ_{ref} , is taken from the middle of the pulse and is 0 degrees for even pulse widths. However the reference for odd pulse widths is given by

$$\theta_{ref} = \frac{2\pi}{2 \times OSR_{RF}} \text{ [radians]} \quad (3.4)$$

If the quantised amplitudes, \hat{v}_r , are confined to all the even pulse widths, then the phase reference does not change and so amplitude quantisation and phase quantisation are independent One Dimensional (1D) operations; it is similar when the quantisation amplitudes are confined to odd pulse widths. When both odd and even pulse widths are taken into account, a change in amplitude can cause a change in phase of θ_{ref} (AM to Phase Modulation (PM) conversion) and so to avoid this joint amplitude and phase quantisation must be applied. This is a two-dimensional operation and leads to a great increase in quantiser complexity.

The amplitude and phase quantisation points can be described in the phase plane of the output carrier signal. The v_i and v_q signals from the $\Sigma\Delta$ filters form the input vector that is to be quantised in terms of amplitude and phase. The quantisation points, P_i , are the intersection of the N_A amplitude rings with the N_P phase spokes. The input vector must be quantised to the closest quantisation point. This is shown in Figure 3.4 for odd quantisation and even quantisation schemes. In both cases the phase and amplitude decisions are orthogonal, so the selection of amplitude and phase of the closest quantisation point are independent.

Figure 3.4 shows the even quantisation and the odd quantisation in the polar plane. The radius of the circles is set by \hat{R} . The radial lines show the quantised phase, $\hat{\theta}$. The even quantisation point of $Q_E[\hat{v}_r, \hat{v}_\theta]$ are illustrated by red dots. The odd quantisation points $Q_O[\hat{v}_r, \hat{v}_\theta]$ are illustrated by the black crosses. The dashed circles between each of the circles (red is for even polar, and black is for odd polar) are the threshold levels for the amplitude quantiser, L_R . The phase threshold levels, L_θ , are measured midway between two phase increments, and are shown as dashed lines.

The number of threshold levels for the amplitude, n_{L_R} , is given by

$$n_{L_R} = N_A - 1 \quad (3.5)$$

where N_A is the number of level amplitude increments. N_A is determined by OSR_{RF} such that

$$N_{A_{even}} = N_{A_{odd}} = \frac{OSR_{RF}}{4} + 1 \quad (3.6)$$

and the number of phases N_P is the same for even and odd

$$N_P = OSR_{RF} \quad (3.7)$$

The total number of quantisation points is therefore

$$N_{Q_{even}} = N_{Q_{odd}} = OSR_{RF} \left(\left(\frac{OSR_{RF}}{4} \right) + 1 \right) \quad (3.8)$$

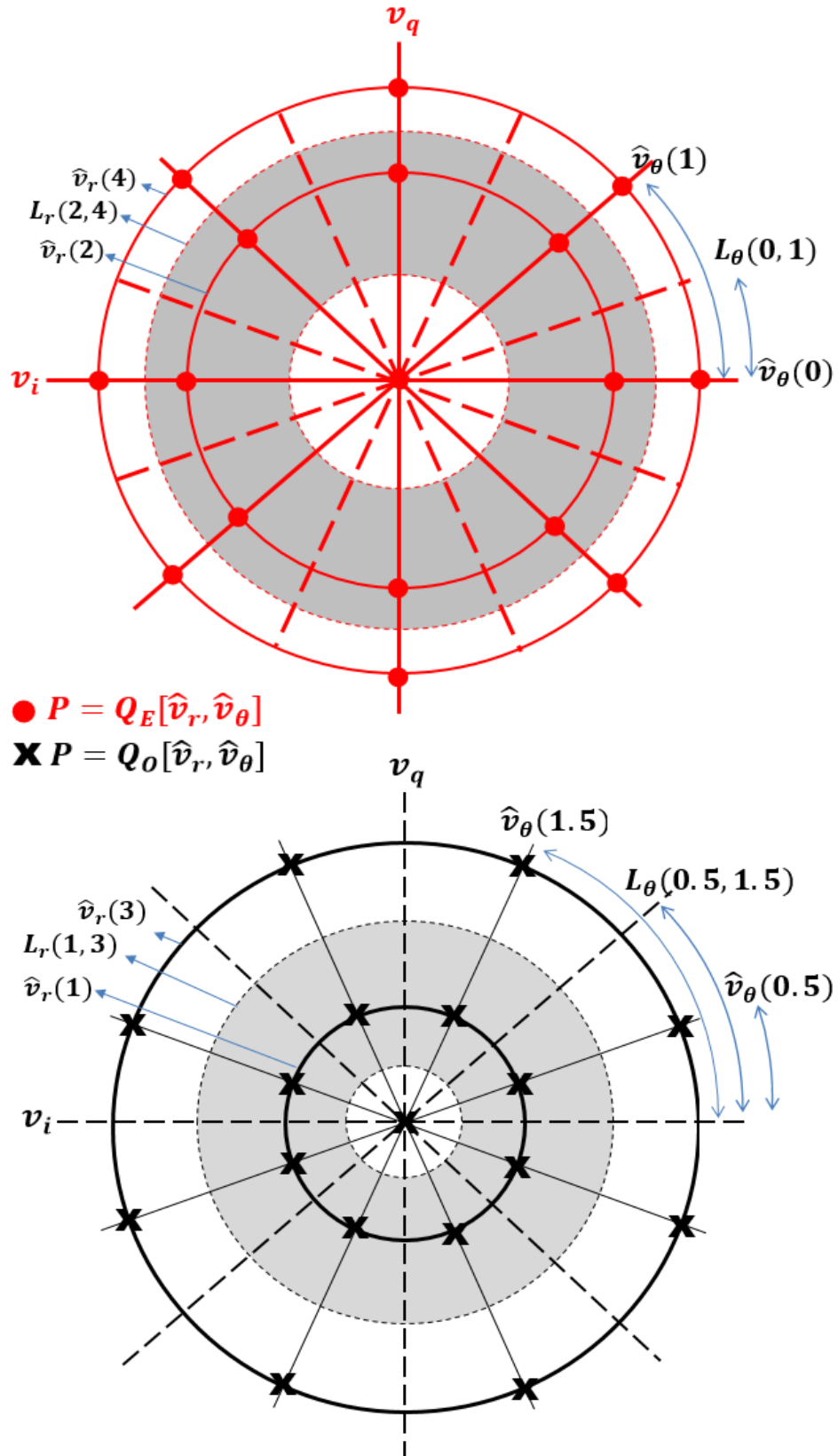


Figure 3.4: The polar quantisation points in the I - Q plane, 'even' (top) and 'odd' (bottom), $OSR_{RF} = 8$, $N_{A_{even}} = N_{A_{odd}} = 3$, $N_P = 8$.

The phase threshold levels, L_θ , are measured midway between two phase increments, and are shown by the dashed line in the polar plane. The number of phase threshold levels, nL_θ , is the same as the number of phase quantised levels, given by

$$nL_\theta = N_p \quad (3.9)$$

Even quantisation leads to a potential coarse quantisation at low signal levels, as shown by the inner (red) circle in Figure 3.4. Therefore, we propose odd quantisation to refine the quantisation of low signal levels by changing the minimum pulse width to one clock period while maintaining a constant phase reference. The first quantisation level is now smaller (pulse width of one). The largest quantisation level is also reduced but by a smaller amount. A calculation of the quantisation amplitude and phase levels which correspond to pulse widths with an odd number of clock periods is shown in Table 3.1.

The quantised phase, \hat{v}_θ , based on the odd polar plane, as shown in Figure 3.4, is given by

$$\hat{v}_\theta = (p_p + 0.5) \frac{2\pi}{N_p} \quad (3.10)$$

where the 0.5 represents the change in reference, θ_{ref} in Figure 3.2. The threshold level L_θ for the quantised phase is calculated by

$$L_\theta((p_p + 0.5), (p_p + 1.5)) = p_p \frac{2\pi}{N_p} \quad (3.11)$$

The amplitude levels are calculated by evaluating the fundamental spectral component of the three-level waveform, $u(\alpha, p_p, OSR_{RF})$ with amplitudes 1, 0, and -1. α is the pulse width corresponding to the α_O clock cycles (α_O is for odd) or α_E clock cycles (α_E is for even). p_p is the pulse position and refers to the time delay or advance. $p_p = (0, \dots, (N_p - 1))$ and represents the PPM delay in clock periods.

Table 3.1: Values of quantised amplitude, \hat{v}_r , for different OSR_{RF} and pulse width (α_E or α_o). There are OSR_{RF} clock periods in one cycle of the nominal RF carrier.

α_o	$OSR_{RF} (=N_P)$					Quantisation scheme
	4	8	16	32	64	
0	0	0	0	0	0	O D D
1	0.9003	0.4873	0.2484	0.1248	0.0625	
3	-	1.1763	0.7074	0.3696	0.1868	
5	-	-	1.0587	0.6002	0.3094	
7	-	-	1.2488	0.8078	0.4290	
9	-	-	-	0.9843	0.5444	
11	-	-	-	1.1229	0.6546	
13	-	-	-	1.2184	0.7585	
15	-	-	-	1.2671	0.8551	
17	-	-	-	-	0.9434	
19	-	-	-	-	1.0227	
21	-	-	-	-	1.0921	
23	-	-	-	-	1.1510	
25	-	-	-	-	1.1988	
27	-	-	-	-	1.2351	
29	-	-	-	-	1.2595	
31	-	-	-	-	1.2717	
α_E						E V E N
0	0	0	0	0	0	
2	1.2733	0.9003	0.4873	0.2484	0.1248	
4	-	1.2733	0.9003	0.4873	0.2484	
6	-	-	1.1763	0.7074	0.3696	
8	-	-	1.2733	0.9003	0.4873	
10	-	-	-	1.0587	0.6002	
12	-	-	-	1.1763	0.7074	
14	-	-	-	1.2488	0.8078	
16	-	-	-	1.2733	0.9003	
18	-	-	-	-	0.9843	
20	-	-	-	-	1.0587	
22	-	-	-	-	1.1229	
24	-	-	-	-	1.1763	
26	-	-	-	-	1.2184	
28	-	-	-	-	1.2488	
30	-	-	-	-	1.2671	
32	-	-	-	-	1.2733	

Since $u(\alpha, p_p, OSR_{RF})$ is a repeating waveform [32], the amplitude of the spectral component can be generated from one period only using the Fourier series. Here, a highly oversampled version of $u_n(\alpha, p_p, OSR_{RF})$ is used to get the same result from a discrete Fourier transform (DFT).

$$U_b(\alpha, p_p, OSR_{RF}) = \frac{1}{N_{FFT}} DFT \left(u_n(\alpha, p_p, OSR_{RF}) \right) \quad (3.12)$$

where N_{FFT} is the fast Fourier transform (FFT) size. The amplitude of the fundamental of the pulse wave occurs in the first frequency bin $b = 1$, defined by

$$\hat{v}_r(\alpha) = 2[|U_{b=1}(\alpha, p_p, OSR_{RF})|] \quad (3.13)$$

The amplitude threshold levels are given by the midpoint of two amplitude quantised levels,

$$L_R(\alpha, \alpha + 2) = \frac{\hat{v}_r(\alpha) + \hat{v}_r(\alpha, \alpha + 2)}{2} \quad (3.14)$$

where α is selected in ascending order.

Table 3.1 shows the quantised amplitudes of the resulting RF signals for odd quantisation and even quantisation schemes. N_A is determined by Equation 3.6 and N_p by Equation 3.7.

Figure 3.5 illustrates the quantisation steps of the quantised amplitude \hat{v}_r versus input amplitude v_r for the odd quantisation and even quantisation schemes. As shown, the example is based on Table 3.1 for $N_p = 8$.

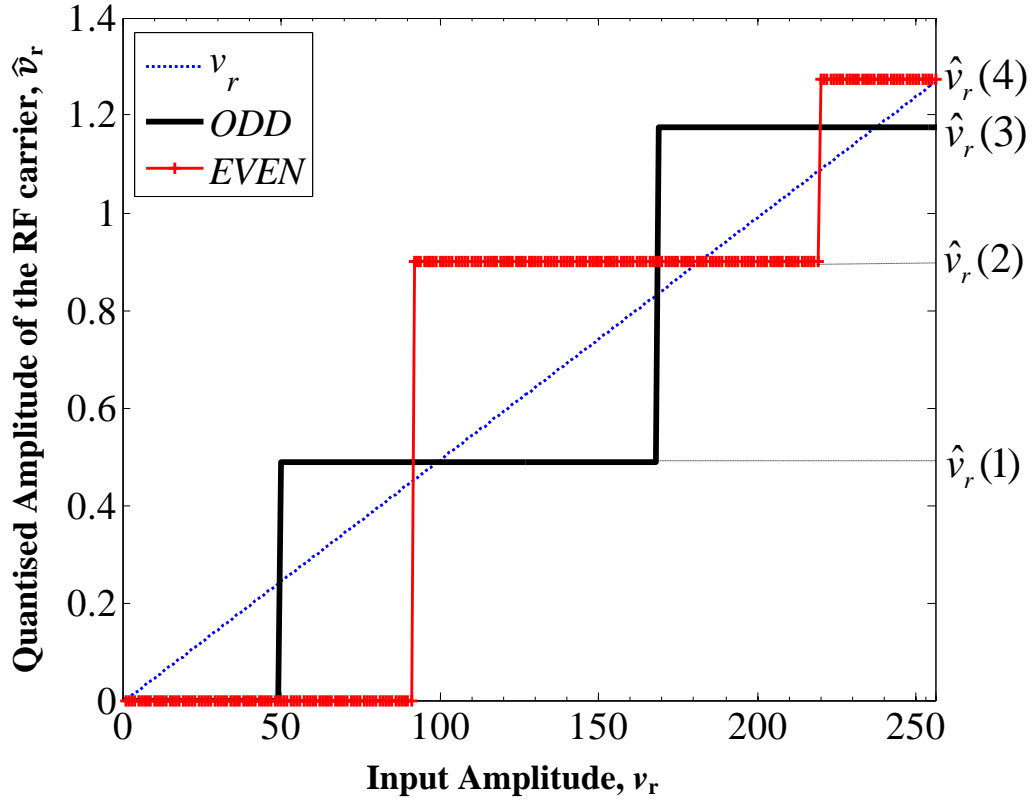


Figure 3.5: Quantisation steps used by Q_R , (Figure 3.1), $OSR_{RF} = 8$.

3.3.1 Polar to PWM/PPM Block

After quantisation (see Figure 3.6), the ‘Polar to PWM/PPM’ block is used to convert the quantised signals, $[\hat{v}_r, \hat{v}_\theta]$ in polar representation to RF using PWM and PPM process. The location of the pulse position of the PPM process is determined using the quantised phase, \hat{v}_θ , which is the output from Q_θ block in Figure 3.1. A change in position depends on a change of \hat{v}_θ where the pulse edges must occur on the digital timing grid. The output of Q_R block, \hat{v}_r , determines the duration of the PWM process.

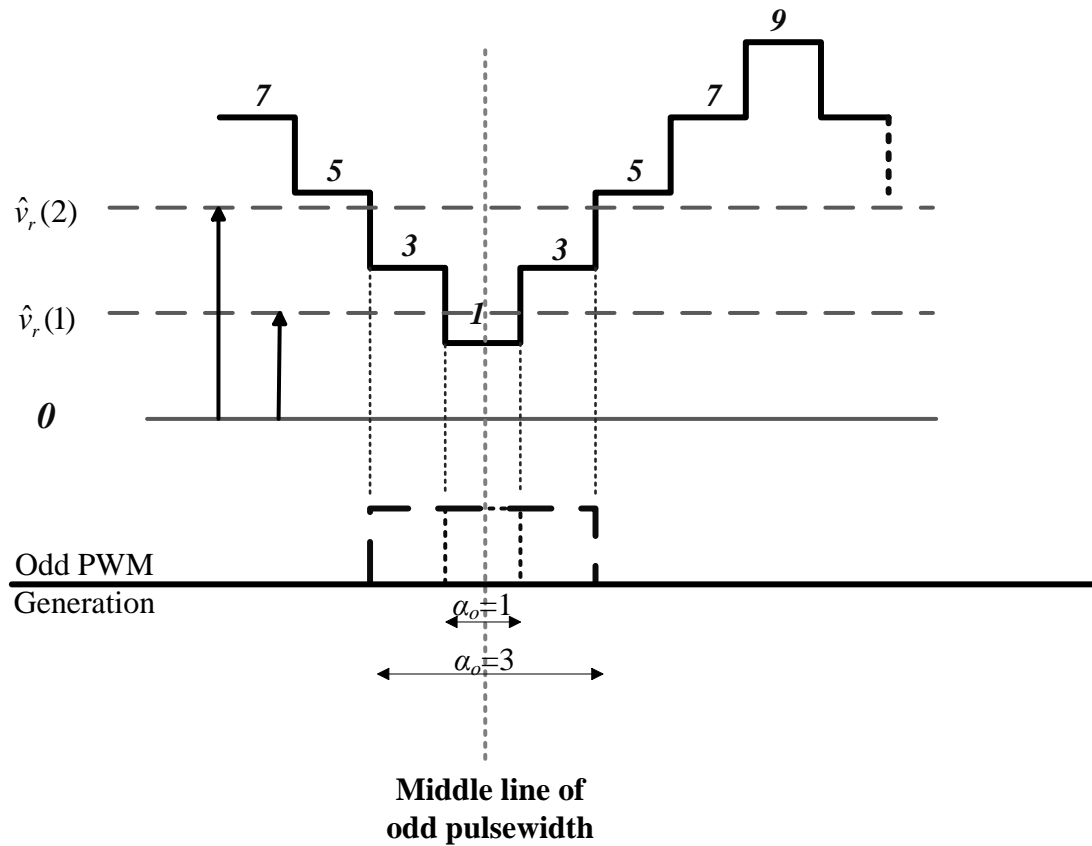


Figure 3.6: Odd PWM generation, $OSR_{RF} = 8$.

Figure 3.6 illustrates the PWM generation the odd quantised signals using a stepped triangle wave. It shows two examples of quantised amplitudes: $\hat{v}_r(1)$ and $\hat{v}_r(2)$. The output pulse widths, $\alpha_o(1)$ and $\alpha_o(3)$, are defined by the crossing points of the line $\hat{v}_r(1)$ and $\hat{v}_r(2)$ respectively and the stepped triangular waveform signal. The pulse width must change with two sample increments to decouple the amplitude response from the phase response. The pulse width then maintains symmetry about its midpoint.

3.3.2 Complexity, Sample Rate and Bandwidth

All DSP systems scale with the sample rate and so the higher the sample rate the larger the bandwidth of the noise transfer function null. This is clearly desirable since $\Sigma\Delta$ systems are a feedback system and so the maximum sample rate (or minimum sample period) is set by the time it takes to process all blocks in the feedback loop. This also includes the quantiser. It is therefore important to make any quantisation process fast.

The benefit of the even or odd pulse-width schemes is that they allow the independent quantisation of phase and amplitude, such that these operations can be performed in parallel, increasing speed and leading to the structure of Figure 3.1. The downside is that only half the possible quantisation points are used and this increases the quantiser error.

In Figure 3.1, quantisation is a three stage process, Cartesian-to-Polar (C2P) conversion, followed by quantisation and then Polar-to-Cartesian (P2C) conversion. The last stage is trivial because quantisation has occurred and there are only a few states to convert; hence a look-up-table (LUT) is the best way to go. The first and quantisation stages can be combined together. A possible solution is to use a few iterations of an iterative algorithm such as CORDIC [95]. CORDIC is an iterative algorithm based on binary arithmetic. It rotates a Cartesian specified vector to the real axis of the complex plane. The rotation gives the angle of the vector and the real component gives it's magnitude.

The feedback structure of $\Sigma\Delta$ converters makes them particularly tolerant to errors in the quantiser decision regions. This fact can be exploited to reduce the number of iterations in the CORDIC algorithm and so reduce latency. Using pre-computing

techniques, it is possible to design a Cartesian $\Sigma\Delta$ with polar quantiser such that its additional latency has almost no effect on the maximum sample rate [32], compared to using I - Q quantisation [61].

3.4 Joint Quantisation Scheme

It is possible to reduce quantisation noise by increasing the density of the quantisation points. One method for achieving this is to increase the OSR_{RF} . Unfortunately, this also increases the clock frequencies, which might not be always practical. An alternative solution is to combine the ‘even’ set of quantisation points with the ‘odd’ set of quantisation points. The downside of this approach is that the phase reference no longer remains constant with signal amplitude, making the design of the quantiser very complex.

In order to get the benefit of the reduced quantisation noise provided by the full family of quantisation points (Figure 3.7), we shall now consider implementation options for joint odd-even quantisation. Intuitively speaking the quantisation error vector will be approximately half that of the even or odd modes when considered separately. The number of quantisation points for the joint odd-even quantisation scheme is:

$$N_{Q_{joint}} = OSR_{RF} \left(\frac{OSR_{RF}}{2} \right) + 1 \quad (3.15)$$

The quantisation point closest to the input vector (shown in blue) must be selected. Two methods are considered: ‘exhaustive search’ and ‘combined odd+even search’.

3.4.1 Exhaustive Search

This is a Two Dimensional (2D) search that involves calculating the squared distance between the input vector and each quantisation point. The quantisation point, P , with the minimum distance is chosen. Five instructions are required to calculate the squared distance, two subtractions, two square operations, and one summation. Selecting the smallest of the outputs requires $N_{Q_{joint}} - 1$ compare (subtract) operations. In terms of latency, we note that all the squared distances can be calculated at once using parallel hardware. The latency is therefore dominated by the compare operations.

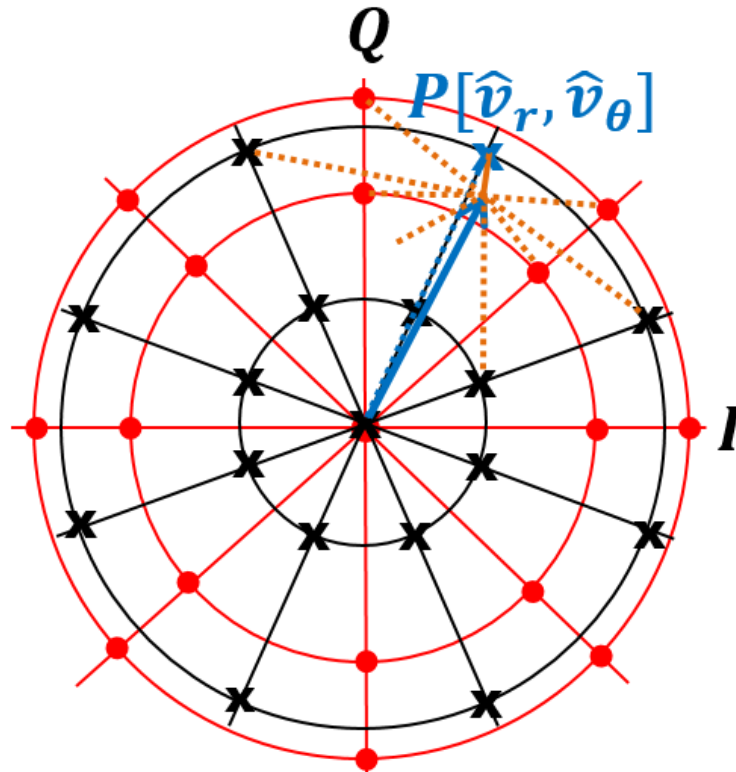


Figure 3.7: Phase plane for optimum joint odd-even quantisation ($OSR_{RF} = 8$).

3.4.2 Combined Odd+Even Search

In this method both odd quantisation and even quantisation are performed separately on the input signal. This gives two potential solutions to the closest constellation point. These two points are then compared in terms of *Euclidean* distance to give the overall optimum choice, see Figure 3.8. The method allows the simpler 1D searches to be performed, with a final single 2D squared error magnitude comparison.

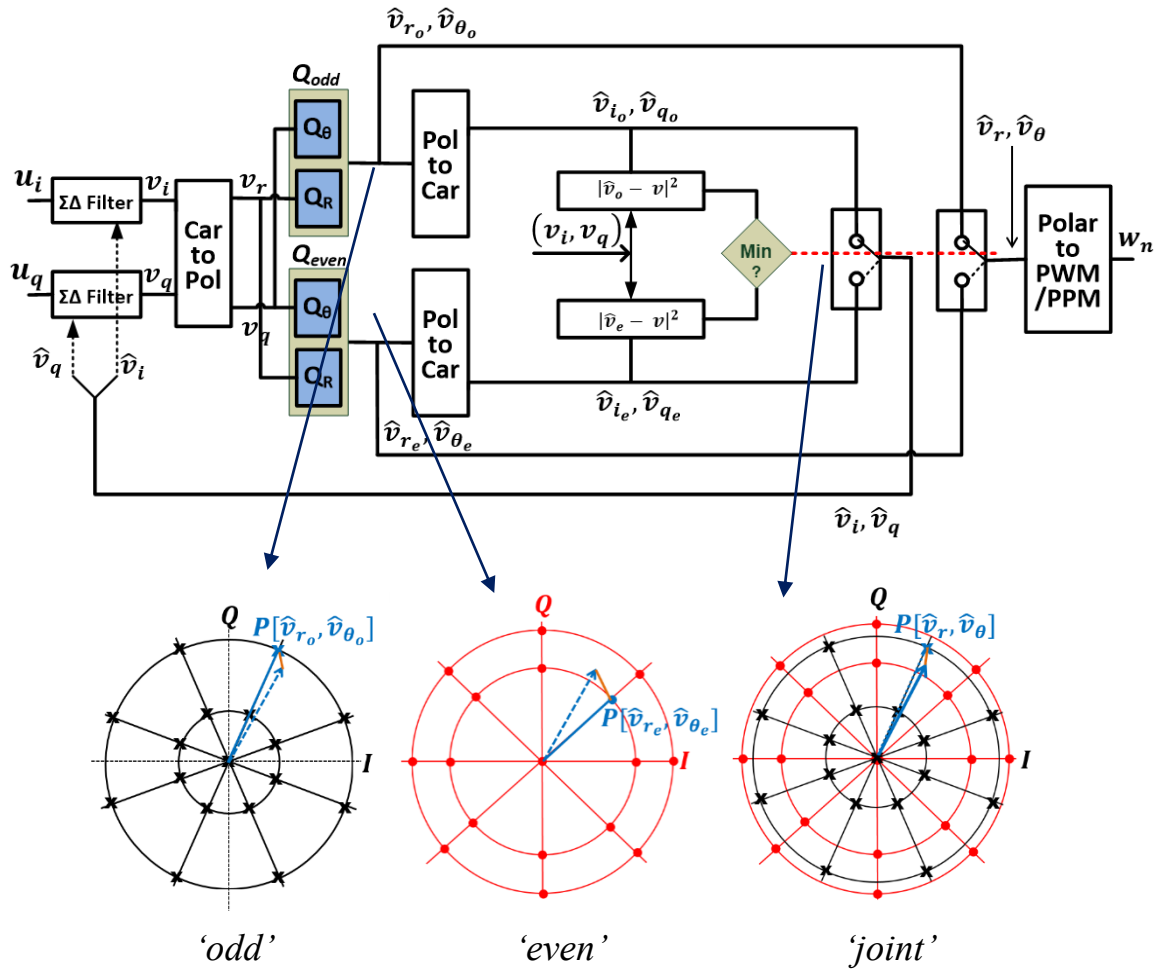


Figure 3.8: Proposed reduced complexity quantiser using separate odd and even quantisers followed by a minimum error selection. An example $OSR_{RF} = 8$ of joint polar plane is described.

Table 3.2: The number of arithmetic operations to implement the quantiser.

Number of Operation							
Scheme Method	Equation	Quantisation Scheme	OSR_{RF}				
			4	8	16	32	64
<i>Odd (or Even) Quantisation</i>							
C2P	$2 \ln_2(OSR_{RF}) + 3$	Odd / Even	7	9	11	13	15
Quantised Amplitude Quantised Phase	$(N_p + N_A) = \left(\frac{5 * OSR_{RF}}{4} + 1\right)$	Odd / Even	6	11	21	41	81
P2C (LUT)	1	Odd / Even	1	1	1	1	1
Total	$2 \ln_2(OSR_{RF}) + \frac{5 * OSR_{RF}}{4} + 5$	Odd / Even	14	21	33	55	97
<i>Joint Quantisation, Method-1: exhaustive search</i>							
Select closest constellation point	$N_{Q_{joint}} - 1$	Joint	8	32	128	512	2046
Minimize $\arg \min_i (\ v - P^i\)$ $i=1; N_{Q_{joint}}$	$5N_{Q_{joint}} = 5\left(\frac{OSR_{RF}^2}{2} + 1\right)$	Joint	45	165	645	2565	10235
Total	$6\left(\frac{OSR_{RF}^2}{2}\right) + 1) - 1$	Joint	53	197	773	3077	12281
<i>Joint Quantisation, Method-2: Combination Odd+Even</i>							
C2P	$2 \ln_2(OSR_{RF}) + 3$	Odd & Even	7	9	11	13	15
Quantised Amplitude and Quantised Phase (number includes both Odd and Even)	$2(N_p + N_A) = 2\left(\frac{5 * OSR_{RF}}{4} + 1\right)$	Odd & Even	12	22	42	82	162
P2C (LUT) and Selection Odd or Even	$2(1 + 5) + 1 = 13$	Odd & Even	13	13	13	13	13
Total	$(2 \ln_2(OSR_{RF}) + 3) + \left(2\left(\frac{5 * OSR_{RF}}{4} + 1\right)\right) + 13$	Odd & Even	32	44	66	108	190

3.4.3 Complexity Comparison

The C2P operation can be achieved by the CORDIC algorithm which approximately doubles the phase accuracy for every iteration. If there are OSR_{RF} phases, then the number of CORDIC iterations should be $\ln_2(OSR_{RF})$ with each iteration having an addition and a compare operation. The amplitude accuracy converges faster without a problem. P2C is a LUT operation and takes only one instruction to operate. Amplitude quantisation takes N_A compare (subtract) operations and phase quantisation takes N_P compare operations for the lowest latency solution (i.e. occurring in parallel). A tree search will reduce the number of compare statements but increase latency.

Table 3.2 shows the breakdown of the number of operations for the odd quantisation and even quantisation schemes and both the exhaustive and combinational joint odd-even quantisation schemes. The odd quantisation and even quantisation schemes are dominated by the quantisation process, with the polar-Cartesian transforms only becoming significant at the lowest OSR. For the joint quantisation scheme the combined method shows an increasing performance benefit over the exhaustive search method as the OSR_{RF} increases.

3.5 Baseband RF Tuning

Wireless systems generally require the carrier frequency to be tunable to any channel position within the band of operation. Ideally, the $\Sigma\Delta$ noise null should span the whole band to avoid the need for a tunable RF band-pass filter at the output. There are two tuning possibilities: firstly, by changing the clock frequency of the upconverter

circuit, which implies the use of a synthesized clock, with an appropriate fine frequency resolution; and secondly by frequency offsetting the input signal within the existing noise null.

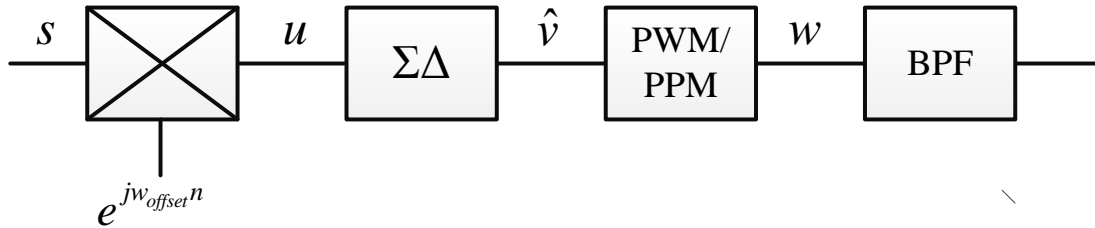


Figure 3.9: The input baseband signal is offset by $\exp(j\omega_{offset}n)$.

The input signal is frequency offset in the baseband by multiplying by $\exp(j\omega_{offset}n)$ prior to being applied to $\Sigma\Delta$ filters (Figure 3.9). Note f_c is the nominal carrier frequency. Unfortunately, a number of distortion products (spurious signals) become apparent when the frequency offset signal is measured *after* the ‘Polar to PWM/PPM’ block. Harmonics, due to the nature of the square pulse of the output signal, fold in-band and become a potential source of interference to adjacent and nearby channels as illustrated in the next section.

3.6 Simulation Results

3.6.1 Spectrum Analysis with SSB signal

In this section the performance of the odd quantisation scheme is measured. The simulation parameter is shown in Table 3.3. The test signal is a SSB tone. Figure 3.10 shows the frequency spectrum of a SSB signal which is offset by 64 MHz from the carrier.

Table 3.3: Simulation parameters for spectrum analysis with SSB signal.

<i>Parameter</i>	<i>Value</i>
Modulated Signal	Continues wave
Nominal frequency carrier (f_c)	1024 MHz
Frequency Offset, Hz (f_{offset})	16, 32, 64, 128, 256 MHz
Bin frequency (Δf)	1 MHz
Oversampling ratio (OSR_{RF})	32
Active tone (A)	1

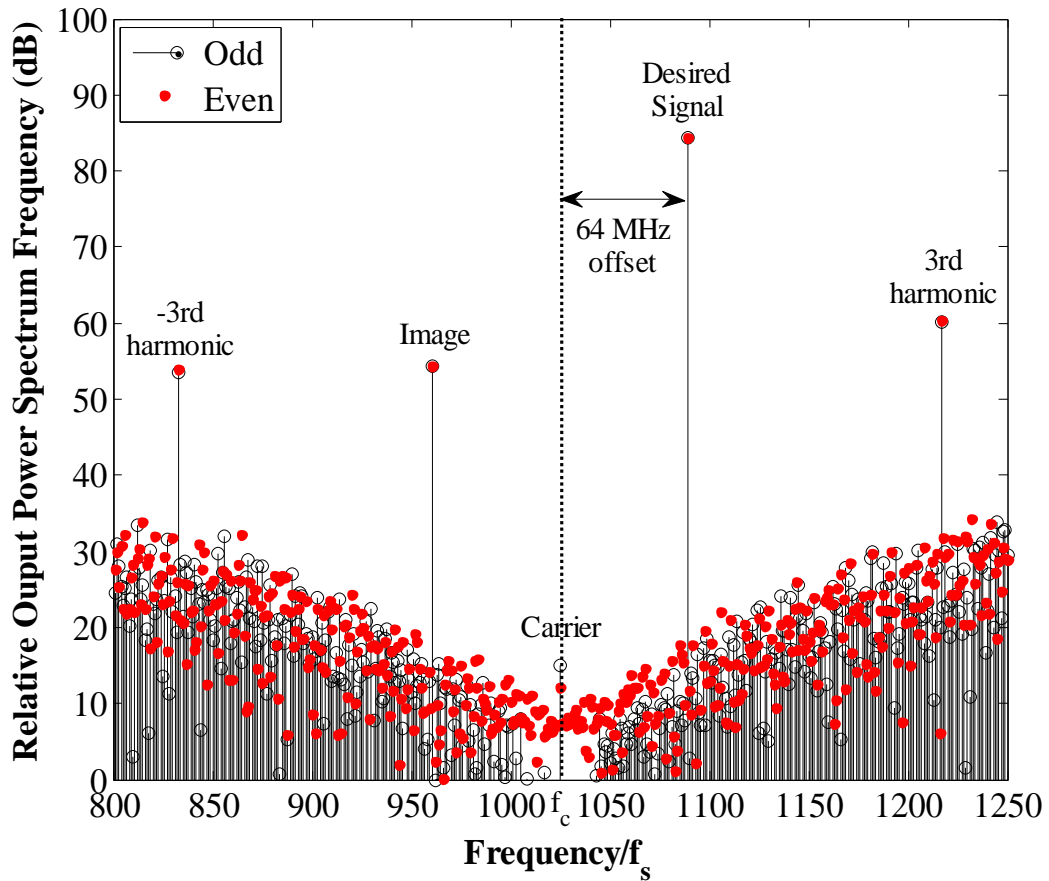


Figure 3.10: Output spectrum of ‘Polar to PWM/PPM’ block, $OSR_{RF} = 32$.

The results are given at the *output* of the ‘Polar to PWM/PWM’ block in Figure 3.1. The spectrums of both the even quantisation and the odd quantisation are drawn for comparison purposes. The red dots show the even quantisation while the black hollow circles show the odd quantisation. Offsetting the carrier frequency from f_c causes distortion products to occur. As shown in Figure 3.10, the dominant harmonic products are the image and odd order harmonics (1st harmonic, 3rd harmonic and -3rd harmonic). The desired signal itself has been placed in the position of the 1st harmonic. The image and 3rd harmonic are unwanted signals. The noise is nulled at the nominal carrier frequency by the $\Sigma\Delta$ operation. The further the signal is from this point the greater the accompanying noise (leading to larger in band EVM).

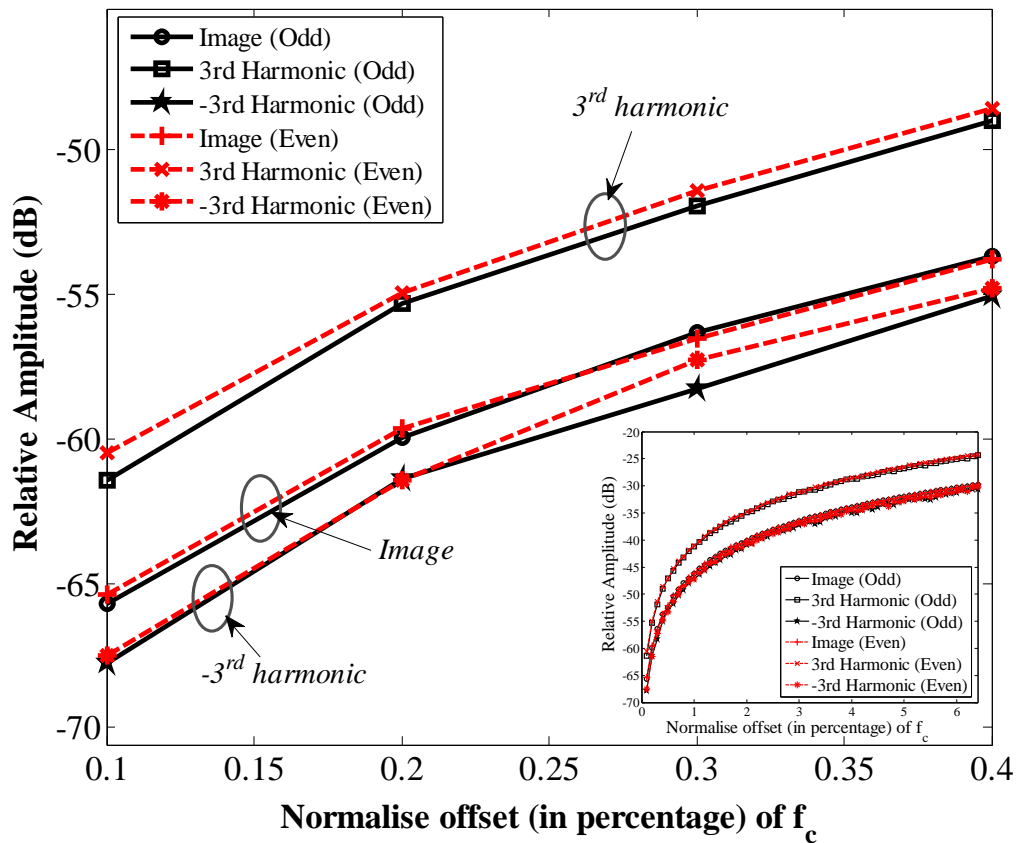


Figure 3.11: Zoom-in of sizes of unwanted signals against 64 MHz of offset frequency ($f_c = 1024$ MHz, $OSR_{RF} = 32$), dB relative to carrier.

The amplitude of the distortion products was compared for the even quantisation and the odd quantisation schemes. As shown in Figure 3.11, the size of unwanted distortion products in the odd quantisation scheme reduces slightly (~ 0.5 dB) compared to the even quantisation scheme. The 3rd harmonic is the largest distortion component. As shown in Table 3.4, the signal-to-noise ratio (SNR) of the desired signals between both schemes are compared. The noise power was calculated for different offset frequencies using a signal bandwidth of 16 MHz ($\frac{f_c}{64}$), that is within ± 8 MHz of the desired signal.

Table 3.4: Comparison of the SNR for odd quantisation and even quantisation schemes.

<i>Offset carrier frequency, Δf MHz (% w.r.t f_c)</i>	<i>SNR, dB</i>	
	<i>Q_{odd}</i>	<i>Q_{even}</i>
16 (1.5%)	92.5	89.4
32 (3.1%)	87.8	85.4
64 (6.25%)	80.4	78.9
128 (12.5%)	70.7	69.8
256 (25%)	59.0	58.4

The signal amplitudes of both the odd quantisation and even quantisation schemes remain stable for all carrier frequency offsets. Interestingly, the signal amplitude for the odd quantisation scheme was slightly reduced compared to the even quantisation scheme. As expected, SNRs degrade when the signal is moved into noisier parts of the spectrum as the frequency offsets increase. More interestingly, the odd quantisation scheme has an

average improved SNR of about 2 dB compared to the even quantisation scheme. This was anticipated for OFDM like signals where low signal magnitudes dominate, but it seems to also apply to continuous wave SSB signals. The explanation is due to the noise components that are part of the $\Sigma\Delta$ output waveform.

The difference between odd quantisation and even quantisation on the image and higher order distortion products is less pronounced. These distortions are caused by the phase quantisation [79] and will make it hard for either scheme to work with a large frequency offset.

3.6.2 Spectrum Analysis with OFDM input signal

A Quadrature Phase Shift Keying (QPSK)-modulated OFDM signal is fed into Cartesian $\Sigma\Delta$ upconverters as described in Figure 3.12. The OFDM bandwidth (B_{ofdm}) was set at $\frac{f_c}{64}$ with $f_c = 1024$ MHz which is equivalent to a B_{ofdm} of 16 MHz (applicable bandwidth to WLAN). The f_s of the $\Sigma\Delta$ is related to the f_c , by

$$f_s = \frac{f_c}{K} \quad (3.16)$$

where the index K is the number of carrier periods between each output sample of the $\Sigma\Delta$ modulator, ($K = \frac{i}{2}$, where i is an integer).

When $i=1$ and $K = \frac{1}{2}$, the pulse width and position is updated every half period of the carrier, which is the highest update rate. In this work we use $K = 1$ ($i=2$) and update every period, to guarantee a DC free waveform. If Δf is the bin frequency spacing between the active tones (A) of subcarriers, therefore B_{ofdm} is equal to $A \times \Delta f$.

The simulation parameters are summarized in Table 3.5. N is the nominal number of

subcarriers in the channel bandwidth, including the null sub-carriers forming the guard band between adjacent channels. D contains all data information. In this situation it is possible to incorporate any frequency offsets into the IFFT used for OFDM generation (Figure 3.12). N_{offset} is the offset frequency measured in bin frequencies.

$$N_{offset} = \frac{f_{offset}}{\Delta f} \quad (3.17)$$

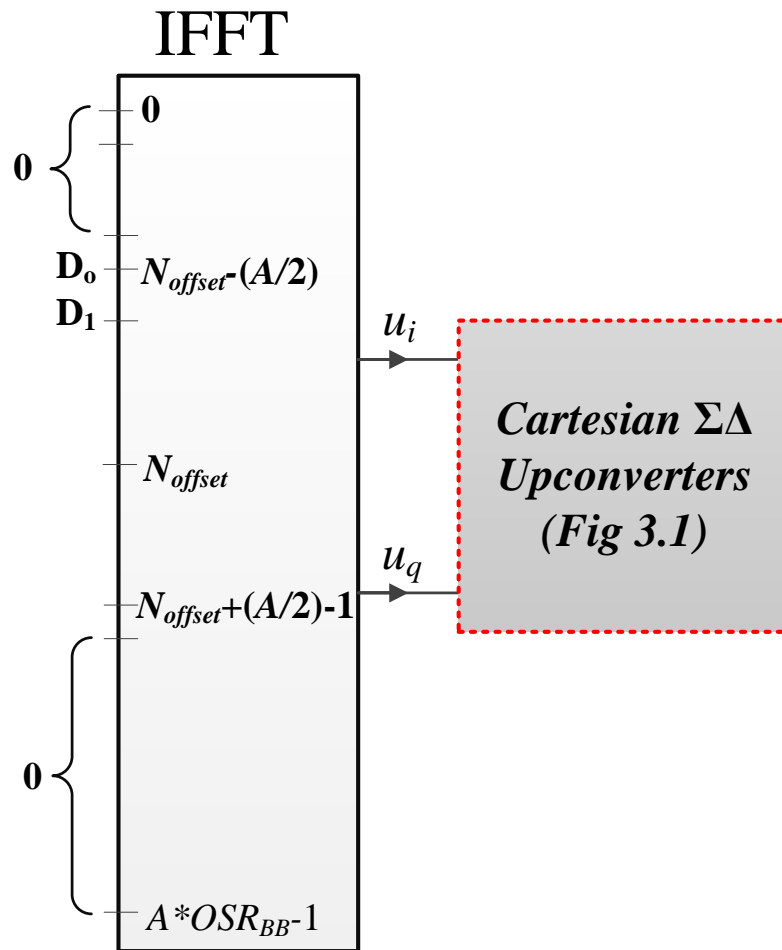


Figure 3.12: The I - Q signal OFDM input to Cartesian $\Sigma\Delta$ upconverters with an offset carrier of N_{offset} frequency bins.

Table 3.5: Simulation parameters for OFDM signal.

<i>Parameters</i>	<i>Value</i>
Modulated Signal	QPSK, OFDM
Nominal frequency carrier (f_c)	1024 MHz
OSR_{BB}	64
Oversampling ratio (OSR_{RF})	32
Nominal channel bandwidth ($N \times \Delta f$)	20 MHz
Active tones (or bins) (A)	16
Active bandwidth ($B_{ofdm} = A \times \Delta f$)	16 MHz
Guard band ($(N-A) \times \Delta f$)	$0.25B_{ofdm}$
Bin frequency (Δf)	1 MHz
Frequency Offset, Hz (f_{offset})	20 MHz
Frequency offset tones (N_{offset})	20

3.6.2.1 Comparison of Joint, Odd, and Even Quantisation Noise Level

The spectrum of the offset OFDM signal is shown in Figure 3.13. The benefit of joint quantisation over odd quantisation or even quantisation is clearly apparent, where an across the band 5 dB reduction in the noise floor is apparent. The even quantisation and odd quantisation levels almost sit on top of each other. The spectrum is measured after the quantiser output (*input* to ‘Polar to PWM/PPM’ block) in which case no distortion or image is present. The next sub-section includes the distortion effect of the ‘polar to PWM/PPM’ block.

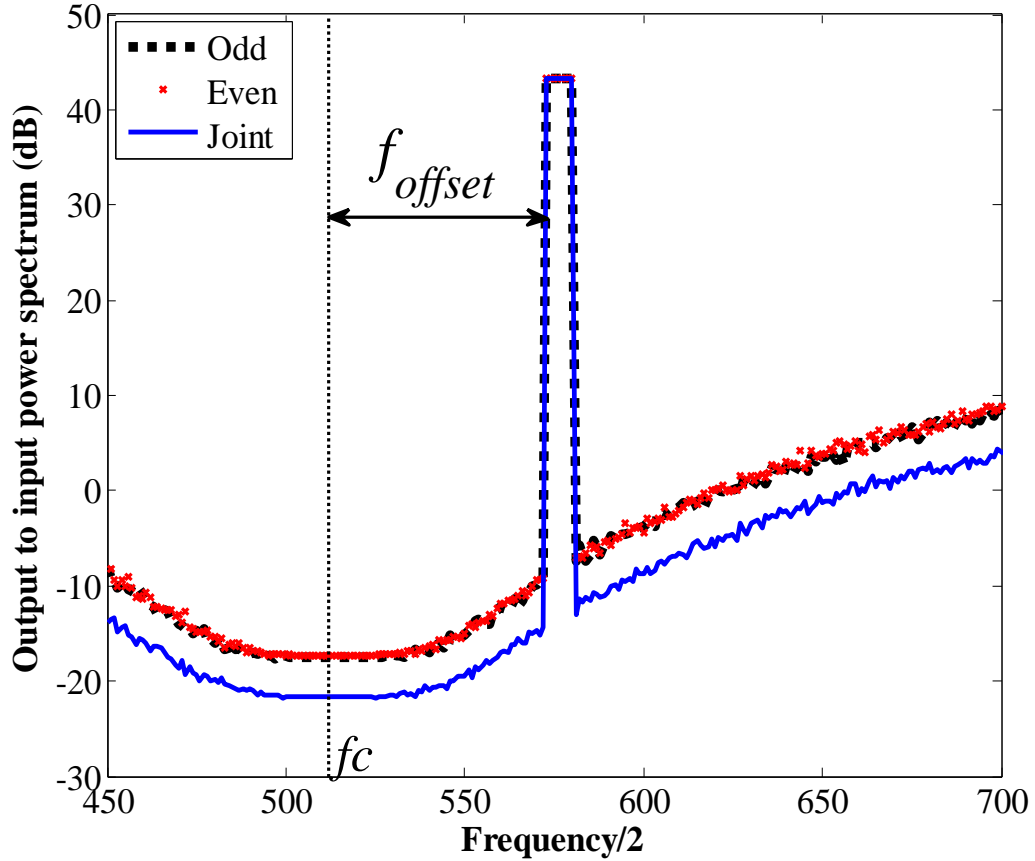


Figure 3.13: An offset OFDM signal with 10 MHz bandwidth, $OSR_{RF} = 32$. ‘Odd’, ‘even’, and ‘joint’ quantisation are compared.

3.6.2.2 Adjacent Channel Powers (ACPs) Characteristics of Odd quantisation and Even quantisation

A spectrum plot of the pulse waveform, w_n , (‘polar to PWM/PPM’ output) of the Cartesian $\Sigma\Delta$ upconverter is shown in Figure 3.14. An RF carrier with an OSR_{RF} of 32 and an OFDM input signal level, $u = -7$ dB (with respect to $u_{rms} = 1$), was offset by one channel bandwidth to examine the resultant spectral images. The adjacent channels and the nominal position of the carrier are marked on the figure to facilitate the understanding of the plot. The signal is present in channel 1. The image is present in

channel -1 and the 3rd harmonic is situated in channel 3 with the highest noise. The noise is lowest in channel 0 as the NTF of the $\Sigma\Delta$ operates from f_c and maximum attenuation of quantisation noise occurs around that region ($\Sigma\Delta$ filters with MOD2). Note the energy of the 3rd order products is smeared over a wider bandwidth compared to the image, and affects more than one channel. The smearing is caused by complicated high order convolutions of the distortion generation process.

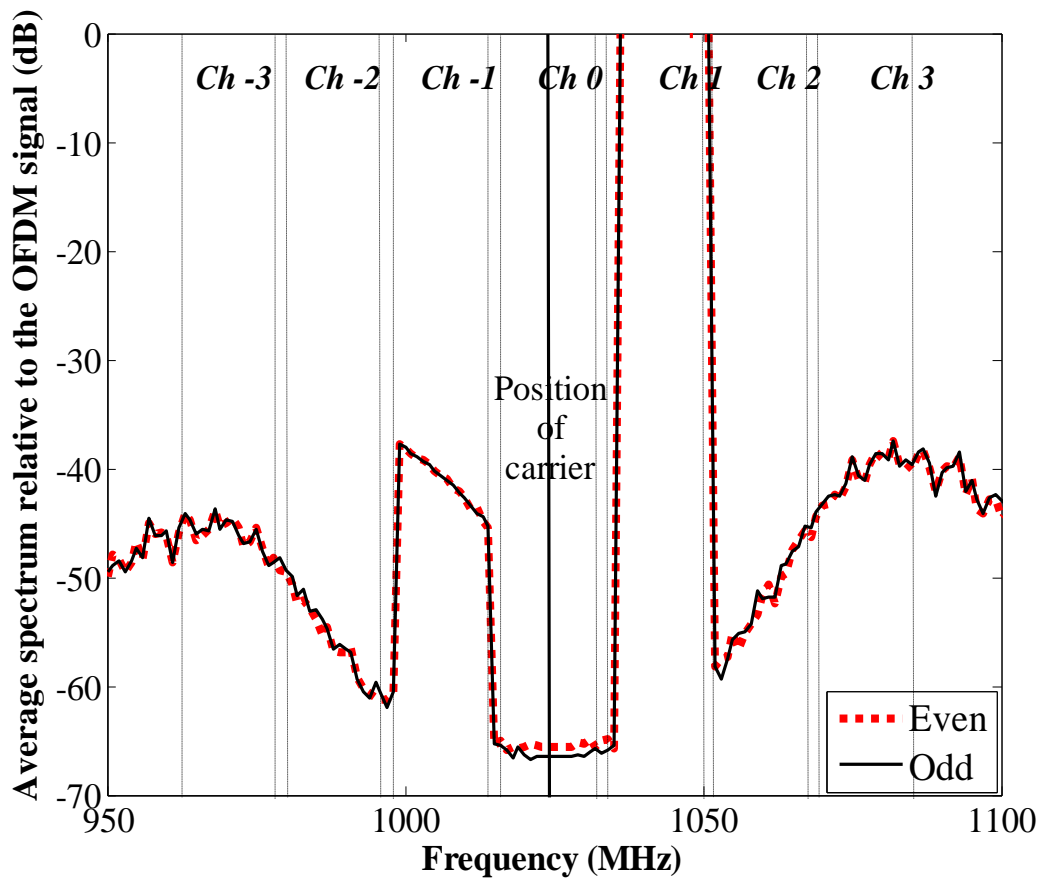


Figure 3.14: Spectrum of odd quantisation and even quantisation with offset OFDM signal ($OSR_{RF}=32$, $f_c=1024$ MHz, and offset=20 MHz/Channel).

The out-of-band distortions for both odd quantisation and even quantisation schemes are compared by calculating their ACPs. The ACPs are defined as the noise

power in the adjacent channel divided by the signal power. The noise power includes quantisation noise as well as distortion arising from PPM.

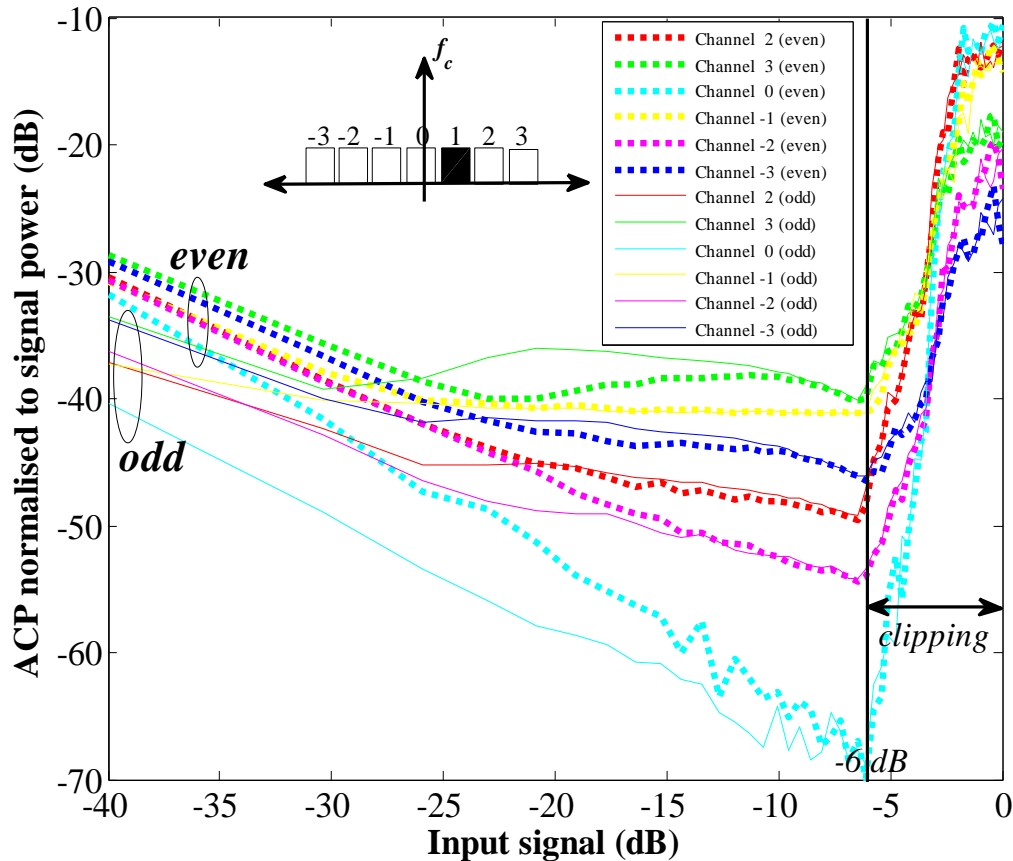


Figure 3.15: Cartesian $\Sigma\Delta$ with the odd quantisation and even quantisation schemes (ACP in adjacent channel versus input signal-to-noise level). $OSR_{RF}=32$, $f_c=1024$ MHz, and offset=20 MHz/Channel.

Figure 3.15 shows a plot of input signal level (dB) against ACP (dB) normalized to signal power for the six adjacent channels obtained after simulating the Cartesian $\Sigma\Delta$ scheme. The shape of the curves indicates -6 dB is the optimum input signal level for best ACP performance. It represents the maximum input signal before the onset of signal clipping that causes a step rise in distortion. At low signal levels, the distortion products are all below the noise floor. Odd quantisation has lower quantisation

thresholds and produces less noise than the ‘even’ method. This figure shows between 4 dB to 8 dB noise reduction in ACP across all adjacent channels. At high signal levels, the noise advantage of the ‘odd’ method dissipates and distortion products dominate many of the adjacent channels because of the larger input signal. Note the poor ACP performance in channel 3, channel -1 and channel -3 where the distortion products dominantly fall. Channel 0 has no distortion and lower noise because the $\Sigma\Delta$ null is centered at f_c .

Single carrier modulation schemes, such as M-ary Quadrature Amplitude Modulation (MQAM), are anticipated to have similar properties to OFDM with the same bandwidth. The key difference would be a small increase in the clipping level (Figure 3.15) due to the more confined amplitude distributions of the modulation.

3.7 Experimental Setup and Measurement Results

The experimental setup for the measurements is shown in Figure 3.16. The equipment used are:

- Tektronix AWG7122B - 2 channel, Arbitrary Waveform Generator (AWG), 12 GB/s
- Tektronix DTG5274 - 2 channel, Data Timing Generator (DTG), 2.7 GB/s
- Mixed Signal Oscilloscope, Tektronix MSO5204, 2 GHz
- Spectrum Analyser, NS, 30, 9 kHz - 3.0 GHz
- A passive combiner.

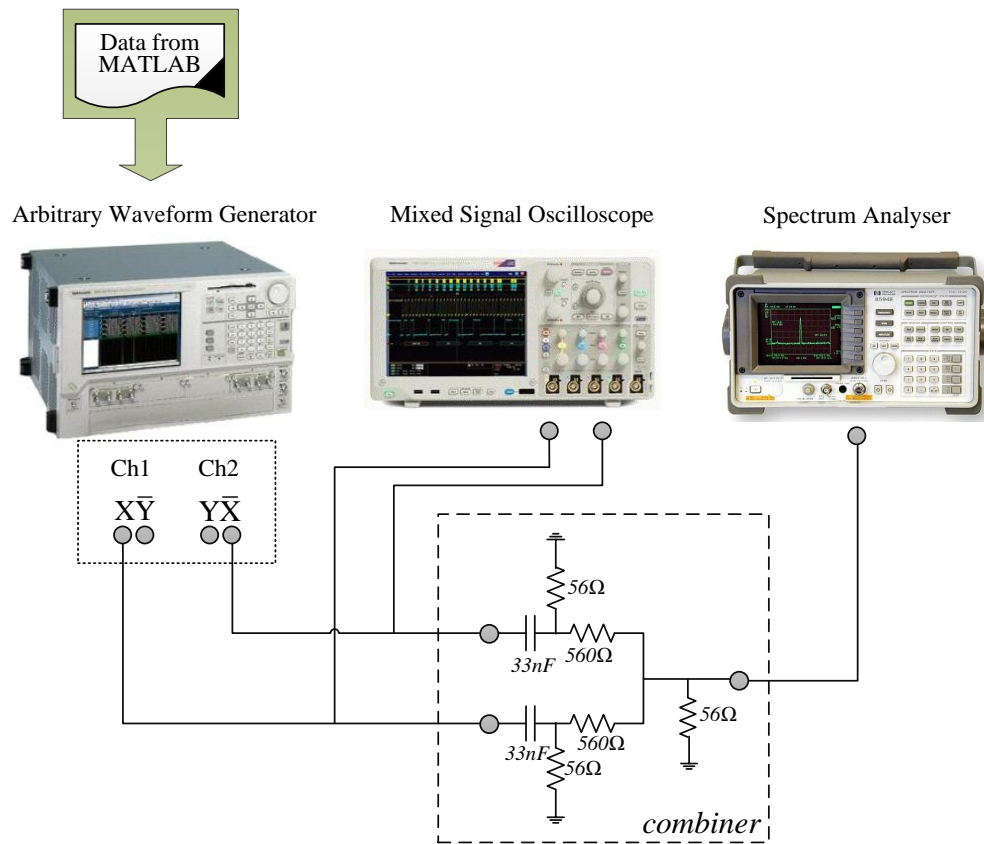


Figure 3.16: Experimental setup for measurement.

The AWG can output an arbitrary sequence of pulses that can drive an SMPA or be directly connected to the load. Two waveforms are generated (b,c) and $-(a,d)$ (see Figure 2.5). Channel 1 is for positive data (b,c) and channel 2 is for inverse negative data $-(a,d)$. The output from the AWG is connected to the spectrum analyser via a passive combiner circuit. The passive combiner circuit sums the two streams (channel 1 and channel 2) to produce the three-level waveforms. A mixed signal oscilloscope was connected from the output of the AWG to show the waveforms of the two component channels (Figure 3.16). The original input waveforms are simulated in *MATLAB*[®], saved in a text file and then downloaded to the AWG.

The measurements were performed at clock rates of 1 GHz, 6 GHz and 12 GHz.

All frequencies are scaled by $\frac{f_{clock\ measurement}}{f_{clock\ simulation}}$ and therefore will affect both f_c and the signal bandwidth by the same fraction. The simulations assume a carrier frequency of 1.024 GHz with different OSR_{RF} values, and therefore different clock frequencies. Table 3.6 shows the relationship between measured and simulated values of f_c and f_{clock} as a function of OSR_{RF} used in this thesis.

Table 3.6: Parameter set for AWG input.

OSR_{RF}	Simulation		Measurement		Ratio ($= \frac{f_{cm}}{f_{cs}}$)	Result Figure
	f_{cs}	f_{clock_s} ($= OSR_{RF} \times f_{cs}$)	$f_{cm} = f_{centre}$ (Max f_{centre} on Spectrum Analyser is 3 GHz)	f_{clock_m} (Max f_{clock_m} on AWG is 12 GHz)		
32	1.024 GHz	32.768 GHz	31.25 MHz	1 GHz ¹	0.030517578	Figure 3.17
16		16.384 GHz	750 MHz	12 GHz	0.732421875	Figures 5.11, 5.12
4		4.096 GHz	1.5 GHz	6 GHz	1.46484375	Figure 5.18

Figure 3.17 shows the experimental results of odd quantisation and even quantisation compared with joint odd-even quantisation. The results are for three-level waveforms with $OSR_{RF} = 32$ and MOD2 $\Sigma\Delta$ filters. The objective was to validate the simulation results using real signals. The measured carrier frequency (f_{cm}) was down-banded to 31.25 MHz by the 1 GHz¹ clock frequency (f_{clock_m}). The joint quantisation scheme has lower noise floor compared with the odd quantisation and even quantisation scheme in the out-of-band region 3 dB - 7 dB. The improvement is less in the in-band zone due to the presence of a floor caused by either the measurement process or distortion products leaking from the OFDM signal. The ‘joint’ improvement is not quite

¹ The high speed AWG was not available for this measurement. The DTG ($f_{clock} < 2.7$ GHz) was used at reduced clock rate to give a more rectangular pulse shape.

as large with respect to the ‘odd’ scheme; suggesting that the ‘odd’ has slightly less noise than the ‘even’ scheme for OFDM signals.

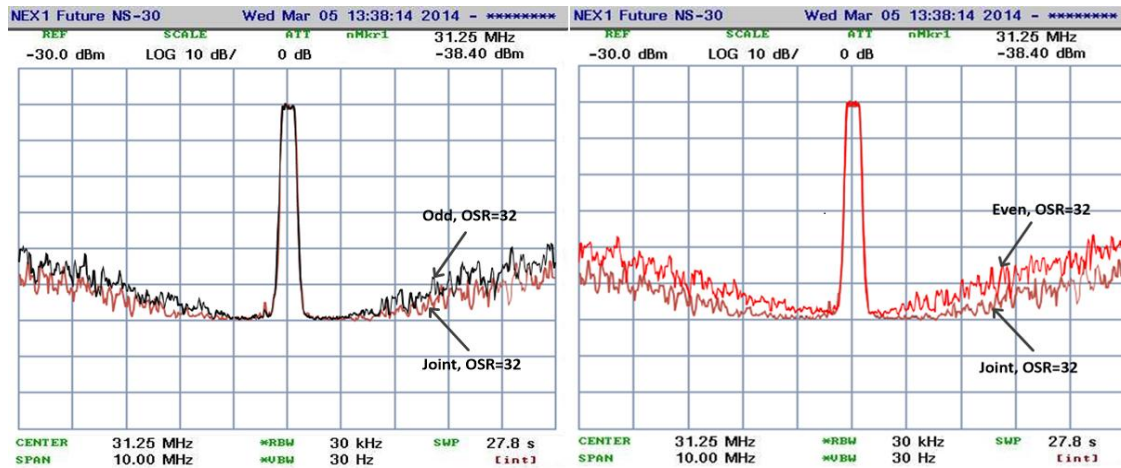


Figure 3.17: Measurement result. The comparison of joint vs. odd quantisation schemes (left) and joint vs. even quantisation scheme (right), $OSR_{RF} = 32$.

3.8 Summary

$\Sigma\Delta$ systems with 2D polar quantisation can be used to generate PWM/PPM signals suitable for radio frequency transmission. These give good bandwidth and noise performance when the $\Sigma\Delta$ filtering is performed in the I - Q domain rather than the polar domain. However, this makes quantisation more difficult because C2P conversion is required inside the $\Sigma\Delta$ feedback loop. The simplest quantisation occurs when pulse widths are restricted to either an even number of clock cycles or an odd number of clock cycles. Quantisation can then be done in amplitude and phase separately.

Previous researchers have developed the ‘even’ scheme, in this chapter we have proposed, developed and implemented an odd quantisation scheme in an attempt to minimize quantisation noise compared to the ‘even’ scheme; the ‘odd’ scheme still changes pulse widths by a factor of 2 to maintain the constant phase reference with varying pulse widths but uses a single pulse (one clock period) as the minimum quantised

amplitude rather than two pulses. This improves resolution for small signals. An experiment was carried out to evaluate in-band noise performance of an unmodulated carrier (SSB tone) with differing frequency offsets by channel noise powers for both the odd quantisation and even quantisation schemes. The noise was measured with a bandwidth of ± 8 MHz of the offset SSB tone and showed a reduction of 2 dB for the 'odd' scheme compared to the 'even' scheme.

Joint-quantisation, which uses both odd and even pulse widths gives a 5 dB reduction in noise floor, but the complexity of the quantiser more than doubles. The best quantiser for the 'joint' scheme does the quantisation of the 'odd' and 'even' points separately and then chooses the closest to the input signal vector. In the experimental measurement it was established that the joint quantisation scheme performs better in the out-of-band region by about 3 dB – 7 dB.

Offsetting of the transmitted signal introduces a number of distortion products which were less effected by the choice of quantisation. It can be observed that the 3rd harmonic is the biggest noise contributor followed by the image. When OFDM modulation is used the distortion components can expand and corrupt many adjacent channels. The type of quantisation ('even', 'odd', or 'joint') does not affect this aspect of the output spectrum. The image and 3rd order distortions dominate the performance at large signal levels and make signal tuning by using frequency offsetting at baseband an unattractive proposition. Tuning by changing the clock rate (f_{clock}) would obviate the need for offsetting and hence avoid the problem, but this is a less flexible solution. The next two chapters will consider solutions to the tuning problem which do not involve changing the clock frequency.

Chapter 4

Proposed Baseband and IF Tuning

4.1 Introduction

Advances in the speed of digital logic has opened the possibility of directly generating modulated RF signals from a single bit stream. As described in the previous section, PWM/PPM techniques are used to control the amplitude and phase of an RF carrier. However, the rectangular nature of the output pulse generates a number of unwanted harmonics and distortion products (the image, 3rd harmonic, -3rd harmonic and other odd order harmonics). In addition, quantisation noise is generated when the pulse edges are synchronised to the timing grid of the digital clock. The management of distortion and noise is a key design challenge as is the requirement for tunability. $\Sigma\Delta$ techniques can shape the noise away from the carrier band for subsequent removal in a band-pass filter (Figure 4.1) [24], but tunability remains a problem.

In this chapter, we propose and describe a method of tuning which is particularly suitable for schemes with high-resolution polar quantisers, such as the waveform PWM-mode Cartesian $\Sigma\Delta$ [32, 76, 79]. The proposed scheme recovers much of the dynamic range over the operating band.

Section 4.2 describes the scenario where a complex phase rotation is applied to the baseband tuning for Cartesian $\Sigma\Delta$ scheme. Section 4.3 discusses interference distortion. Section 4.4 shows spurious removal using IF tuning. Section 4.5 gives a summary.

The work in this chapter has been published for publication by the *IET journal on Electronics Letters*. The title is “Baseband tuning of Cartesian delta–sigma RF upconverters” [96].

4.2 Baseband Tuning for $\Sigma\Delta$ Upconverter

As previously identified in Section 3.5, tuning the carrier frequency to the desired channel is an expected feature in any wireless transmitter. Tuning in the baseband involves frequency offsetting the input signal by rotating the input baseband components. When this occurs a number of distortion products (spurious signals) become apparent in the output spectrum from the ‘polar to PWM/PPM’ block. Harmonics caused by the rectangular pulse shapes fold in-band and cause interference to adjacent and nearby channels. The most dominant of these harmonics are the image and low-order harmonic components which occur in most PWM and $\Sigma\Delta$ like structures [79]. These distortions reduce the dynamic range making it difficult to meet the spectrum mask requirements within the operating band.

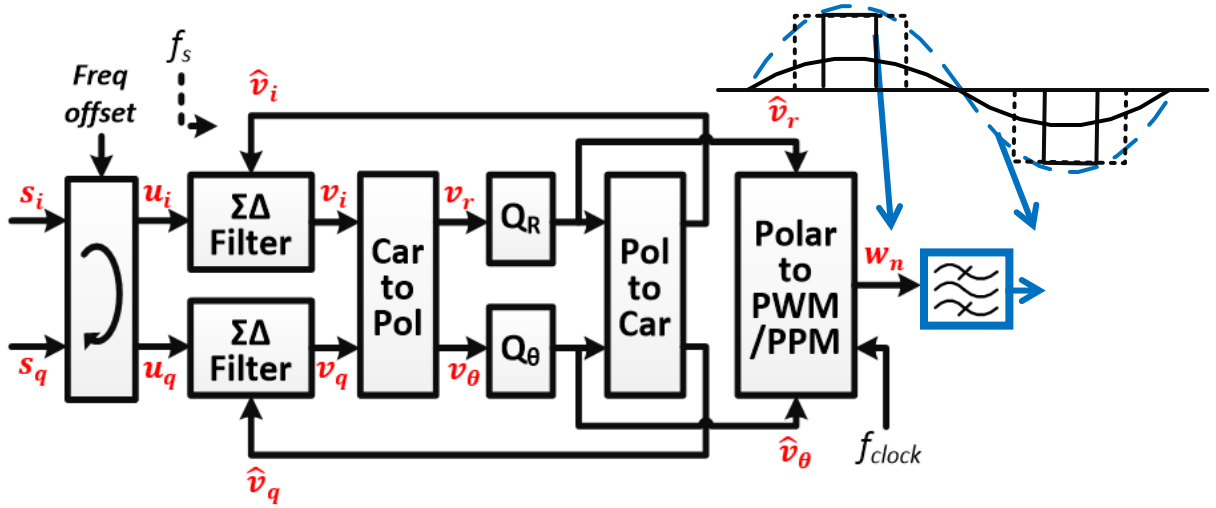


Figure 4.1: Cartesian $\Sigma\Delta$ scheme, joint quantisation is applied for baseband tuning scenario.

As mentioned in Section 3.2, the Cartesian $\Sigma\Delta$ scheme operates at baseband and avoids bandwidth expansion by using a polar quantiser in a Cartesian structure. The magnitude and phase quantisers, Q_R and Q_θ , are sandwiched between C2P and P2C converters (see Figure 4.1). The quantised polar output $[\hat{v}_r, \hat{v}_\theta]$ selects an appropriate bit stream (w_n), from the ‘Polar to PWM/PPM’ block, having the desired pulse width and pulse position for the specified quantised value. The bit stream repeats every RF carrier period. The number of clock periods (f_{clock}) per nominal RF carrier period (f_c) sets the number of available quantisation points; the number of pulse widths or quantisation levels is N_A and the number of pulse positions or quantisation phases is N_P . Improved quantiser fidelity implies a higher digital clock frequency.

The width and position of the pulse train are updated after K periods of the RF carrier ($K \geq 1$) giving a fixed relationship between the $\Sigma\Delta$ sample frequency, f_s , and the nominal carrier frequency f_c (see Equation 3.16) such that

$$K = \frac{f_c}{f_s} \quad (4.1)$$

See [32] for further details. In the simulations the $\Sigma\Delta$ filters are second-order (MOD2) [24], the nominal carrier frequency $f_c = 512$ MHz, $K = 1$ and $OSR_{RF} = 32$. The clock frequency, f_{clock} , is therefore 16 GHz, which is within the limits of today's digital technology [84, 97].

4.3 Interference Distortion

A $BW_b = 70$ MHz with $BW_{ch} = 10$ MHz channelization (normalised bandwidths of 0.137 and 0.02 respectively) are considered a complex phase rotation applied on the input baseband signal, s , will frequency offset the output signal, u , to the desired channel position by f_{offset} , where

$$u = \exp\left(j \times \frac{2\pi}{f_s} \times f_{offset} \times n\right) \times s \quad (4.2)$$

where $u = (u_i + ju_q)$, $s = (s_i + js_q)$ and n is the sample number. In Figure 4.2, channel 4 ($f_{offset} = 0$) shows only small distortion skirts some 56 dB below the carrier affecting the two nearest adjacent channel positions. However offsetting the frequency by 10 MHz to the next channel (channel 3) enables the identification of a number of large distortion components: the image in channel 5, the -3^{rd} order harmonic in channel 7 and the $+3^{rd}$ order harmonic in channel 1. The $+3^{rd}$ order distortion produces the worst-case in-band spurious components some 41 dB below the carrier, which is 14 dB more than that produced by channel 4. As the offset frequency increases so does the magnitude of the spurious outputs. Channel 1, at the band edge generates the largest spurious components, of which the image in channel 7, some 35.5 dB below the carrier is the most problematic.

The distortion components destroy the good in-band noise shaping performance of the $\Sigma\Delta$ filters.

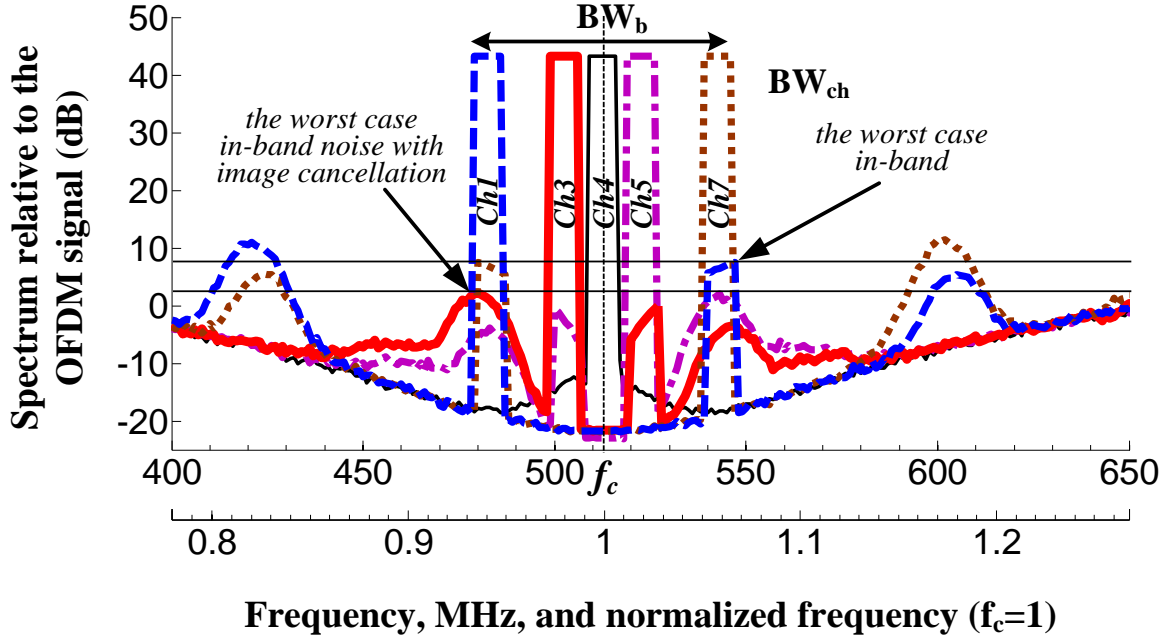


Figure 4.2: Simulated output spectrum for different channel position.
 $OSR_{RF}=32$, Quantisation = ‘joint’.

4.4 Spurious Removal using IF Tuning

We exploit the fact that as the frequency offset increases, the distortion products actually move out-of-band and can be potentially filtered out using the RF band-pass filter. If the whole band is shifted by an intermediate frequency (IF), $f_{IF} > \frac{BW_b}{2}$, then all the channels will be on one side of the nominal centre frequency, f_c , and all the spurious images will fall on the other side of f_c and are hence out-of-band. If the intermediate frequency is shifted by $f_{IF} > BW_b$ then all the $+3^{\text{rd}}$ distortion components will be out-of-

band (since they are shifted by 3 times as much). In practice, the distortion energy of the 3rd harmonics span 3 or more channels and so some energy still leaks in-band, therefore a further shift of half a channel is required giving f_{IF} as

$$f_{IF} = BW_b + \frac{BW_c}{2} \quad (4.3)$$

which in this case is a shift of $70 + 5 = 75$ MHz as shown in Figure 4.3. The third order product of channel 1 just misses the upper band edge.

Although the distortion has been removed, the band of interest is no longer in the $\Sigma\Delta$ noise null. To solve this problem the noise null is shifted to the new frequency. One way to do this is to use $\Sigma\Delta$ filters with complex coefficients, to shift the noise transfer function zeros around the unit circle to the new f_{IF} frequency [90]. However, here an alternate method that tunes both the noise and the input baseband signal to the new intermediate frequency is developed. The proposed scheme involves applying a frequency rotation of f_{IF} at the input to the quantiser and then reversing the rotation in the feedback path (Figure 4.4). The phase rotation is given by

$$X = \exp(j\delta) \times V \quad (4.4)$$

and

$$\delta = \frac{f_{IF} \times 2\pi}{f_s} n : \text{Mod}2\pi \in [-\pi, \pi). \quad (4.5)$$

From Equation 4.4, $x = (x_i + jx_q)$ and $v = (v_i + jv_q)$ are in Cartesian form. This way, the output signal is frequency shifted yet the $\Sigma\Delta$ filters still see the same baseband signal and therefore have no need for complex coefficients. The structure can be applied to I - Q based quantisers such as in [61], but is particularly suitable for polar

quantisation as shown in Figure 4.5, where the complex multiplication can be replaced by a simple addition (or subtraction) of the phase component ($v_\delta = v_\theta + \delta$).

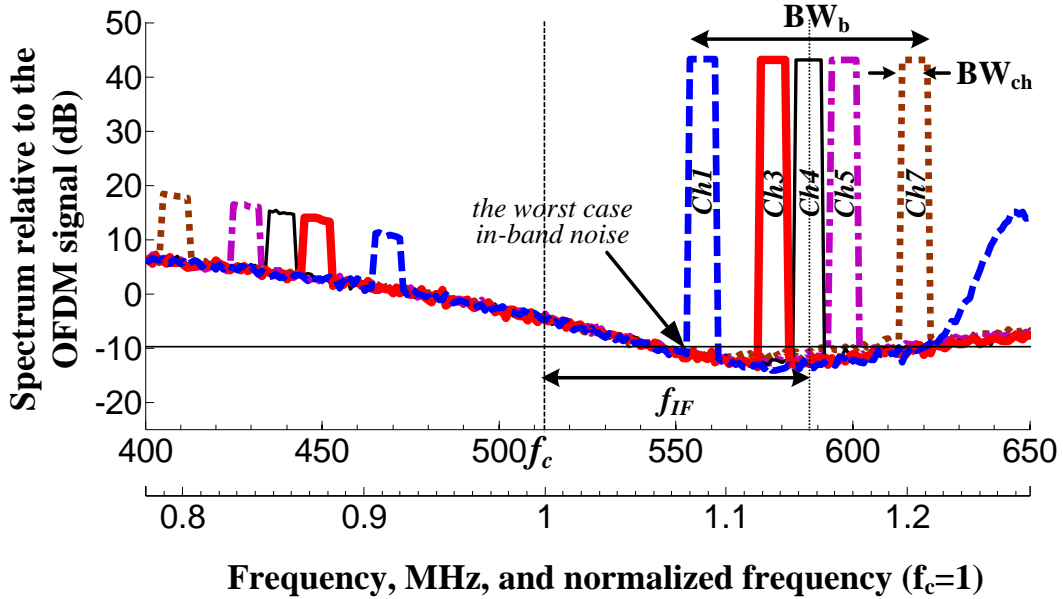


Figure 4.3: Simulated output spectrum at $f_{IF} = 75$ MHz. The distortion products are moved away from the band of interest and would be filtered out by the RF band-pass filter. $OSR_{RF} = 32$, quantisation = ‘joint’.

With the distortion products removed, the overall performance is determined by the noise null. The null is not as deep as the baseband signal would suggest due to other noises folding into band from the image and distortion products [90]. There is an improvement for all the channel positions, except the zero offset channel (channel 4) of the original baseband scheme of Figure 4.2. Overall, the noise is at least 52 dB below the carrier for all channel positions, an improvement of 11 dB on the original system of Figure 4.2 with image cancellation or an improvement 16.5 dB without image cancellation. Image cancellation is discussed in Chapter 5.

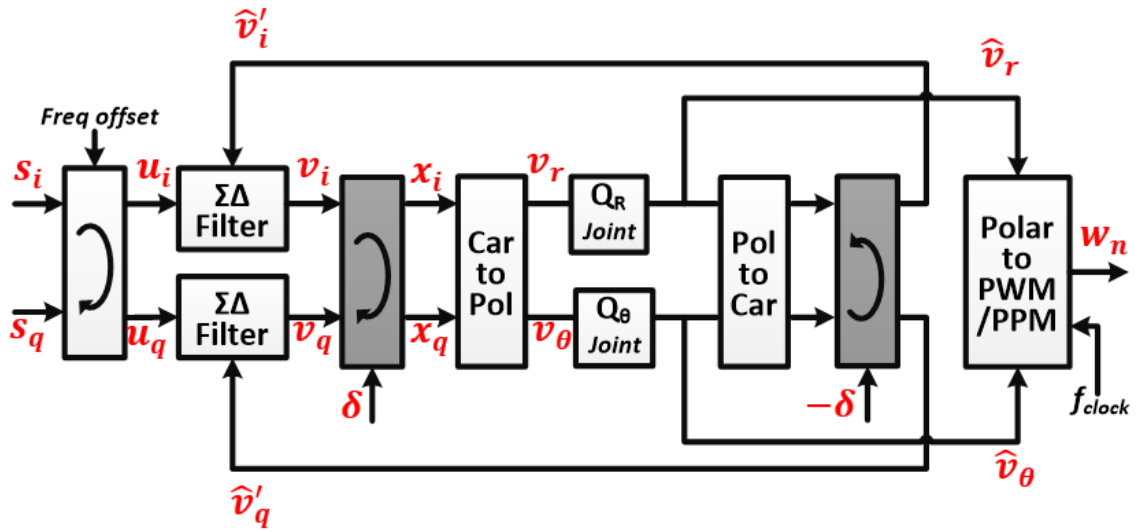


Figure 4.4: Proposed Cartesian $\Sigma\Delta$ upconverters with applied phase rotation & derotation in Cartesian format.

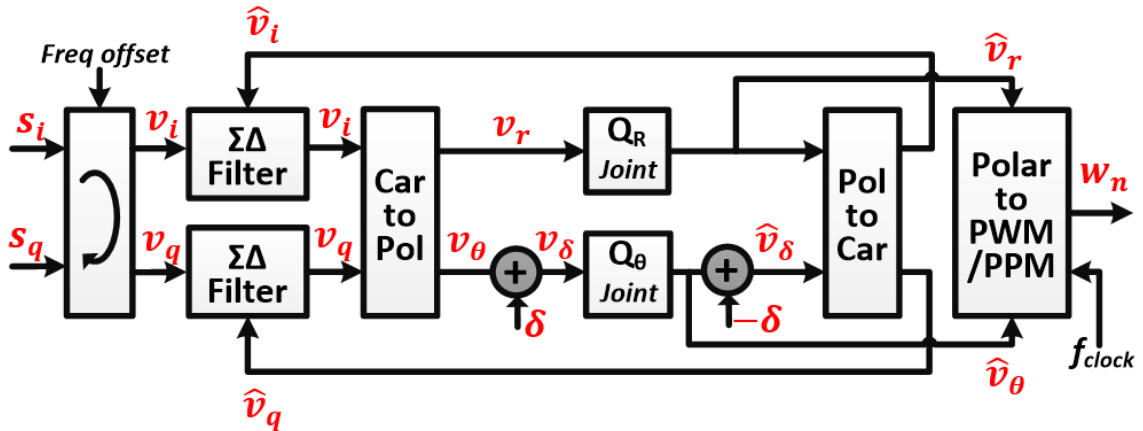


Figure 4.5: Proposed Cartesian $\Sigma\Delta$ upconverters with applied phase rotation & derotation in polar format.

4.5 Summary

All digital $\Sigma\Delta$ transmitters suffer from image and distortion products that generate adjacent channel interferences when the transmission is tuned away from the natural carrier frequency. This study shows that introducing a deliberate intermediate frequency shift equal to the transmission band bandwidth plus half of a channel bandwidth will move all distortion products out of band. A new frequency shift method involving phase rotators before and after the quantiser is described.

Although the application of an IF frequency shift, f_{IF} , will move the distortions out-of-band, the in-band noise nulls deteriorate compared to the non-shifted condition. Comparing the noise levels between Figure 4.2 and 4.3 (neglecting distortion products), there is degradation in noise floor of about 8 dB. This worsens as the IF frequency increases.

The next chapter will explain how the distortion products arise and considers techniques to cancel the image product and some of the noise enhancement cause by the IF shift.

Chapter 5

Proposed Image and Noise Cancellation

5.1 Introduction

In this chapter, the phenomenon of unwanted spectral components generated by the ‘Polar to PWM/PPM’ block of the proposed scheme is explained, followed by the solution to the distortion problem. The source of the unwanted spectral components was attributed to the generation of pulse width modulated signals and pulse position modulated signals when used to upconvert the polar signal to RF. The rectangular nature of the output PWM/PPM pulse generates a number of unwanted harmonics and distortion products such as image and 3rd harmonic which are the most dominant distortions. These distortions fold into the operating band. Therefore, image and noise cancellation using pre-distortion techniques is proposed so that all the operating bands can meet the spectrum mask requirements.

Section 5.2 describes how unwanted spectral components became apparent on the system. For more detail, Section 5.3 includes an improvement to the mathematical analysis of [79] for predicting the magnitude of the distortion products. Section 5.4 explains the use of a pre-distortion technique for image cancellation. Simulations and measurements of image cancellation applied to a multicarrier signal will be described in this section. Section 5.5 explains the use of a post-distortion technique for noise cancellation. Simulations and measurements of noise cancellation will also be described in this section. Section 5.6 is the summary.

5.2 Unwanted Spectral Components

Even though the proposed transmitter architecture is based on a $\Sigma\Delta$ modulation scheme which can suppress the quantisation noise, the ‘Polar to PWM/PPM’ block is not located inside the $\Sigma\Delta$ loop. Hence, unacceptable noise from the ‘Polar to PWM/PPM’ block output cannot be eliminated by the feedback mechanism. In this situation, the image and odd order harmonics ($\pm 3^{\text{rd}}$ harmonics, $\pm 5^{\text{th}}$ harmonics, etc.) are unwanted around the desired signal when the carrier frequency of the desired signal is offset. An analysis in [79] shows the PPM block is responsible for these distortions.

The output of the quantiser is a baseband signal of $[\hat{v}_r, \hat{v}_\theta]$ in polar format. It feeds the ‘Polar to PWM/PPM’ block which generates a pulsed square waveform with a number of quantised pulse widths and pulse positions which represents amplitude and phase respectively. A phase change ($\hat{\theta}$) will cause the pulse position within the nominal carrier period to change. This operation is achieved by swallowing or stuffing a pulse whenever the instantaneous phase moves from one phase quantisation level to another.

However, the loss or gain of a pulse can affect the amplitude of the signal in terms of the ratio of the duration of the positive-amplitude to the negative-amplitude of a square pulse

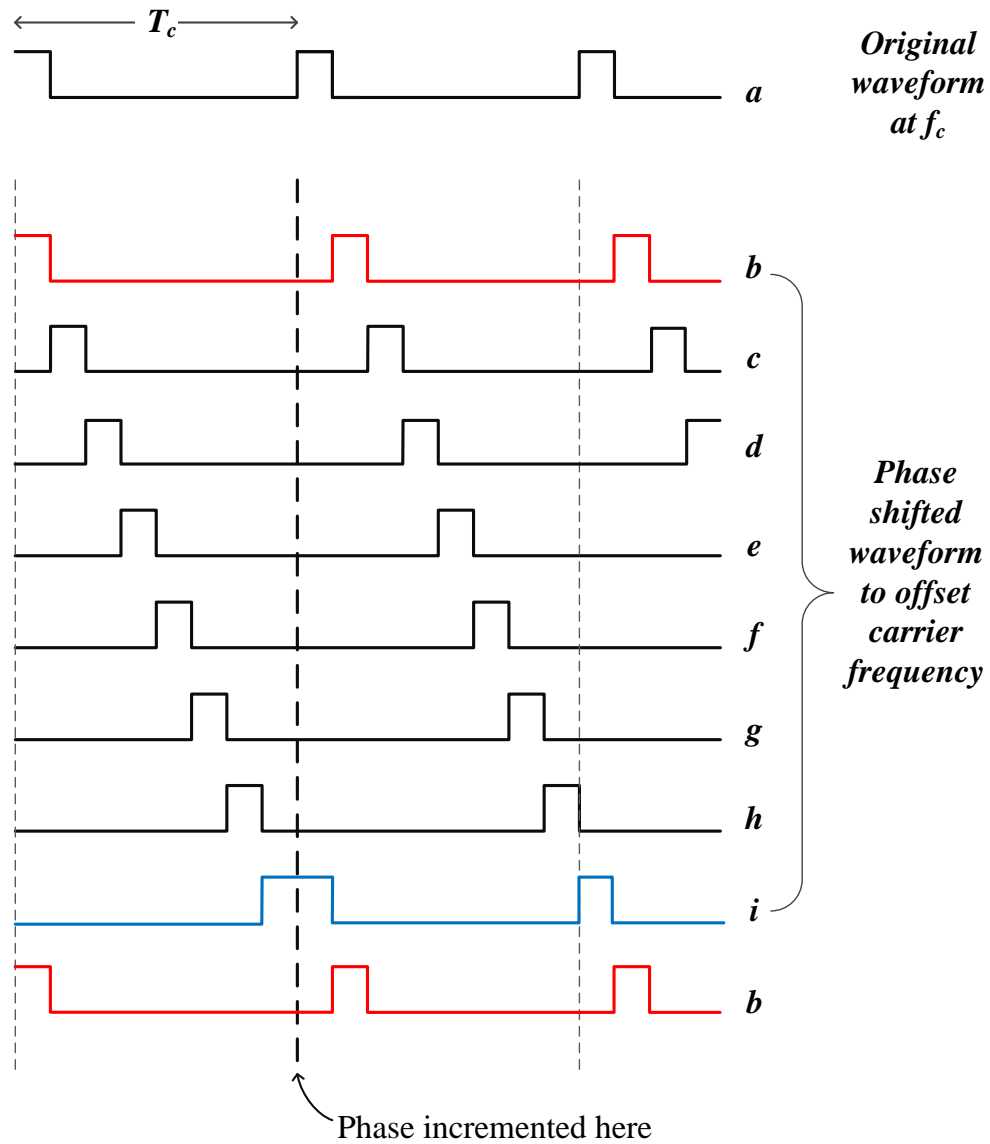


Figure 5.1: Phase shift waveform when the pulse change in a position [79].

(mark-space ratio). This process leads to AM distortion. When the pulse is high (logic '1') at the end of the carrier period, it will wrap around to the beginning of another

repeating pulse in the next period resulting in a wider high pulse. This phenomenon indicates the presence of an image and other harmonic components in the spectral domain. Figure 5.1 illustrates how an extended period of phase changes, such as caused by a frequency offset, causes harmonic production.

In Figure 5.1, an example of the phase shifted waveform process caused by a SSB input signal is explained. The phase is quantised into 8 quantisation levels and T_c corresponds to the period of the nominal carrier frequency, f_c . On the top, waveform-*a* is the original waveform at f_c ($=\frac{1}{T_c}$) with pulse width $\alpha = 1$. Waveform-*b* indicates a change in phase (a change in pulse position) in the 2nd period. When the phase is changed there is a change in the mark-space ratio between two consecutive pulses which lasts for one period (T_c). Waveform-*c* represents the next phase shifted waveform. In the remaining waveforms, the phase is incremented every second period to produce a SSB signal at $f_c + f_{ssb}$. Here f_{ssb} refers to the offset frequency, f_{offset} . The waveforms-*d*, *e*, *f*, *g*, and *h* indicate the constantly incrementing phase. Interestingly, at the 8th period, the waveform-*i* shows a double pulse width ($\alpha = 2$) where the high pulse of its first period joins the high pulse of the beginning of the second period. The wider high pulse is shown clearly at this waveform (line blue). After that, the waveform returns to waveform-*b* (red line) and the process is repeated.

5.3 Mathematical Analysis of Harmonic Distortion

A mathematical analysis is carried out to determine the harmonic distortion at the output of the ‘Polar to PWM/PPM’ block. The approach in [79] will be followed with modifications to enhance the analysis.

The mathematical analysis is based on a single SSB tone. Either an Upper Side Band (USB) or Lower Side Band (LSB) carrier is generated at frequency, $(f_c + f_{ssb})$ or $(f_c - f_{ssb})$ Hz respectively. The phase slope $\left(\frac{\partial\theta}{\partial t}\right)$ determines the side band frequency, f_{ssb} , where

$$f_{ssb} = \frac{1}{2\pi} \frac{\partial\theta}{\partial t} \quad (5.1)$$

therefore
$$\frac{\partial\theta}{\partial t} = 2\pi f_{ssb} \quad (5.2)$$

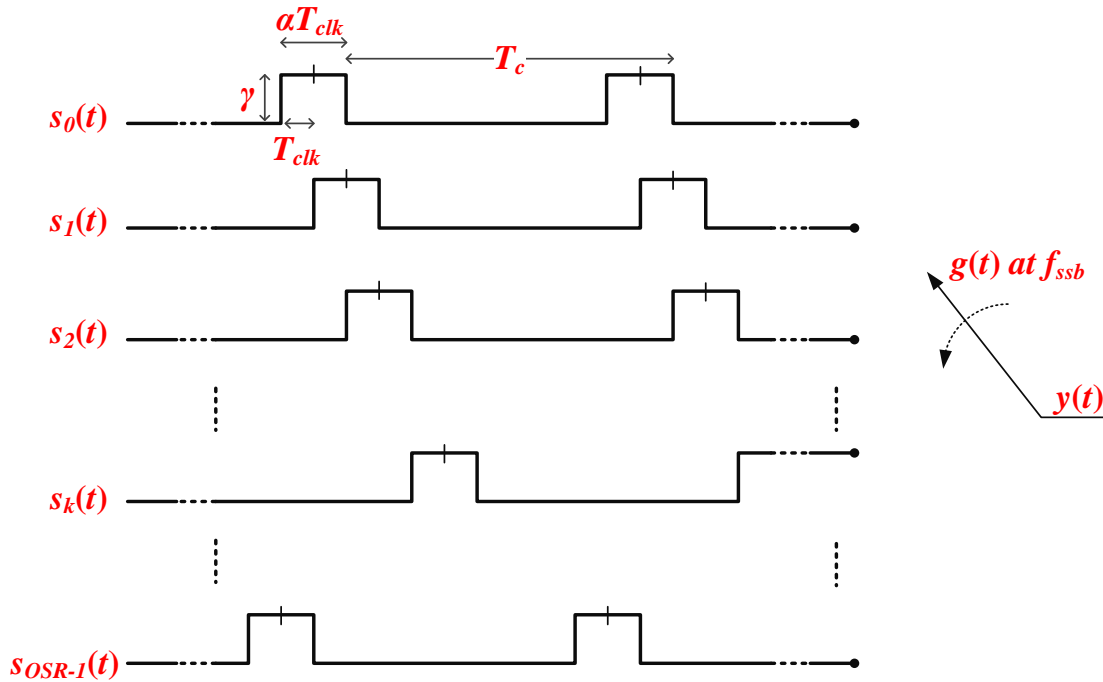


Figure 5.2: Phase shifted oscillators generate a SSB signal [79].

The phase linearly ramps up. After quantisation with step size, $\Delta\theta$, the ramp changes to a staircase signal with OSR_{RF} steps in 2π radians, given

$$\Delta\theta = \frac{2\pi}{OSR_{RF}} \quad (5.3)$$

Figure 5.2 illustrates SSB generation from a bank of phase-shifted oscillators. Each oscillator has an output of a quantised phase of $s(t)$ where $s_0(t)$ is the first quantised phase. The k^{th} oscillator has an output signal $s_k(t)$ with quantised phase shift of $k\Delta\theta$, where $k = 0, 1, \dots, (OSR_{RF} - 1)$. There are OSR_{RF} clock periods in each carrier signal period, where

$$T_c = T_{clk} \times OSR_{RF} \quad (5.4)$$

So, $s_1(t)$, for instance, is $s_0(t)$ delayed by T_{clk} . Therefore, the expression for the output signal $s_k(t)$ can be written by,

$$s_k(t) = s(t + kT_{clk}) \quad (5.5)$$

In the PWM/PPM process, the PWM maintains the pulse width constant (αT_{clk}) and the PPM controls the increment (or decrement) of the pulse position. Therefore, all oscillators have the same pulse width, αT_{clk} at frequency f_c .

In Figure 5.2, the output $y(t)$ is obtained from a switch which rotates at a constant speed of f_{ssb} rotations/sec. Each waveform, $s_k(t)$, is selected for a period by T_g . The switch operates in a counter clockwise direction to delay the signal by 2π radians in T_{ssb} ($= \frac{1}{f_{ssb}}$) seconds. The frequency of $y(t)$ is $(f_c - f_{ssb})$. The switch must rotate clockwise to give $f_c + f_{ssb}$ (USB).

T_g is the duration that each of the OSR_{RF} oscillators is connected (or gated) to the output. Hence,

$$T_g = \frac{T_{ssb}}{OSR_{RF}} \quad (5.6)$$

Figure 5.2 is functionally equivalent to Figure 5.3 which shows the generation of SSB signal from the input $s(t)$ and $g(t)$, so the mathematical analysis can be expressed in more detail.

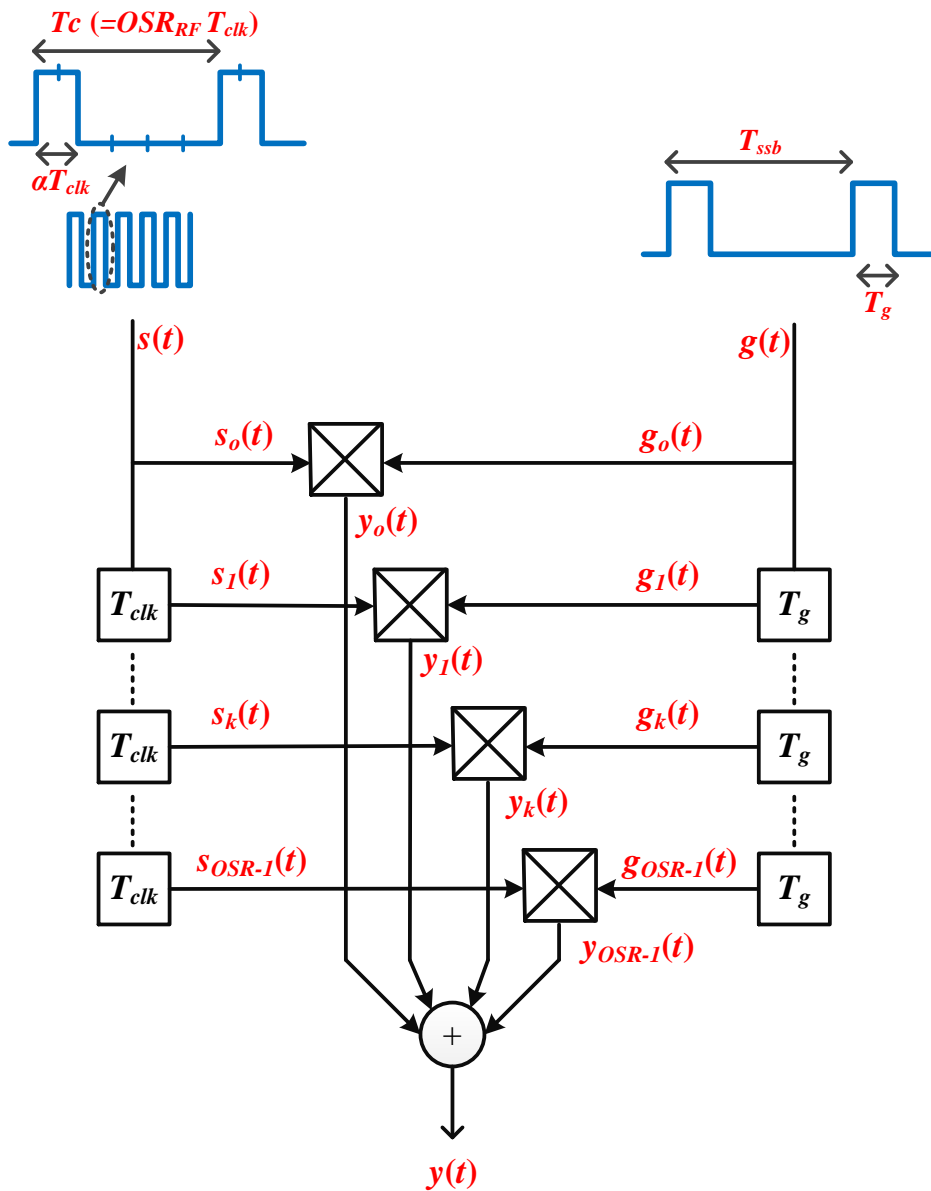


Figure 5.3: SSB generation for mathematical analysis [79].

Inputs $s(t)$ and $g(t)$ are single reference oscillators for generating the OSR phased waveforms of $s_0(t)$ and $g_0(t)$ respectively. The ' k^{th} ' delayed version of the input signals become $s_k(t)$ and $g_k(t)$ respectively as per Equation 5.5 for the carrier signal and Equation 5.7 for the gating waveform.

$$g_k(t) = g(t + kT_g) \quad (5.7)$$

The $g_k(t)$ gating waveform effectively selects each $s_k(t)$ output in turn. The output from the k^{th} gate is given by

$$y_k(t) = s_k(t) g_k(t) \quad (5.8)$$

and the total output $y(t)$ is the summation from all OSR_{RF} multiplexed output gates, derived as

$$y(t) = \sum_{k=0}^{OSR_{RF}-1} y_k(t) \quad (5.9)$$

To obtain the spectrum of $y(t)$, all operations must be transformed to the frequency domain using Fourier transform. In this case, $\tilde{Y}(f) = F\{y(t)\}$ is calculated. For simplicity, the derivation has been done in three distinct sections, they are: the derivation of $\tilde{S}(f) = F\{s(t)\}$, the derivation of $\tilde{G}(f) = F\{g(t)\}$, and the convolution of $\tilde{S}(f)$ with $\tilde{G}(f)$. Note that the expression in Equation 5.8 is a multiplication in the time domain that is equivalent to convolution in the frequency domain.

5.3.1 The Reference Carrier Signal $\tilde{S}_k(f)$

Since the reference carrier signal, $s_0(t)$, is a repeating pulse signal, then the properties of the discrete-time Fourier series method are used to calculate the spectrum [98]. Therefore,

$$\tilde{S}_0(f) = \sum_{n=-\infty}^{\infty} S_0(n)\delta(f - nf_c) \quad (5.10)$$

where

$$S_0(n) = \frac{\gamma \times \alpha T_{clk}}{T_c} \text{sinc}\left(\frac{n \times \alpha T_{clk}}{T_c}\right) \quad (5.11)$$

$S_0(n)$ is the Fourier series of pulse train of $s_0(t)$. From Equation 5.4, $T_c = T_{clk} \times OSR_{RF}$, the expression of Equation 5.11 now can be simplified and written as

$$S_0(n) = \frac{\gamma \times \alpha}{OSR_{RF}} \text{sinc}\left(\frac{n \times \alpha}{OSR_{RF}}\right) \quad (5.12)$$

The *sinc* function controls the amplitude of the series of delta function of $S_0(n)$ at the harmonics of f_c . Since $s_k(t)$ is a delayed version of $s_0(t)$ (see Figure 5.3), we can define $S_k(n)$ by using the time shifting property of the Fourier transform, by

$$S_k(n) = S_0(n)e^{\frac{j2\pi nk}{OSR_{RF}}} \quad (5.13)$$

Therefore, the spectrum of the delayed waveform and the delay waveform can be written as

$$\tilde{S}_k(f) = \sum_{n=-\infty}^{\infty} S_k(n)\delta(f - nf_c) \quad (5.14)$$

or

$$\tilde{S}_k(f) = \sum_{n=-\infty}^{\infty} S_0(n)e^{\frac{j2\pi nk}{OSR_{RF}}} \delta(f - nf_c) \quad (5.15)$$

5.3.2 The Gate Signal $\tilde{G}_k(f)$

The novel contribution to the analysis starts here. Previous work constrained the period of the SSB gating waveform to be an integer number of samples, so the formulae developed only apply to a few discrete frequencies [79]. This constraint will now be relaxed and the formulae will be valid for any value of f_{ssb} (f_{offset}). The analysis approach is described in Figure 5.4.

When the edge of a SSB gating waveform, $g_0(t)$, is not quantised on the sample grid, it experiences jitter. Figure 5.4(i) shows the desired input gating, $g_0(t)$; the signal and its spectrum is shown by the Fourier series of this repeating pulse $g_0(t)$ of period of T_{ssb} . $\tilde{G}_k(f)$ consists of harmonics of f_{ssb} ($= \frac{1}{T_{ssb}}$) weighted by a *sinc* function with nulls at $\frac{1}{T_g}$.

$$\tilde{G}_k(f) = \sum_{n=-\infty}^{\infty} G_k(m) \delta(f - mf_{ssb}) \quad (5.16)$$

where

$$G_0(m) = \frac{1}{OSR_{RF}} \text{sinc} \left(\frac{m}{OSR_{RF}} \right) \quad (5.17)$$

and the delayed version of $G_0(m)$ is

$$G_k(m) = G_0(m) e^{j \frac{2\pi mk}{OSR_{RF}}} \quad (5.18)$$

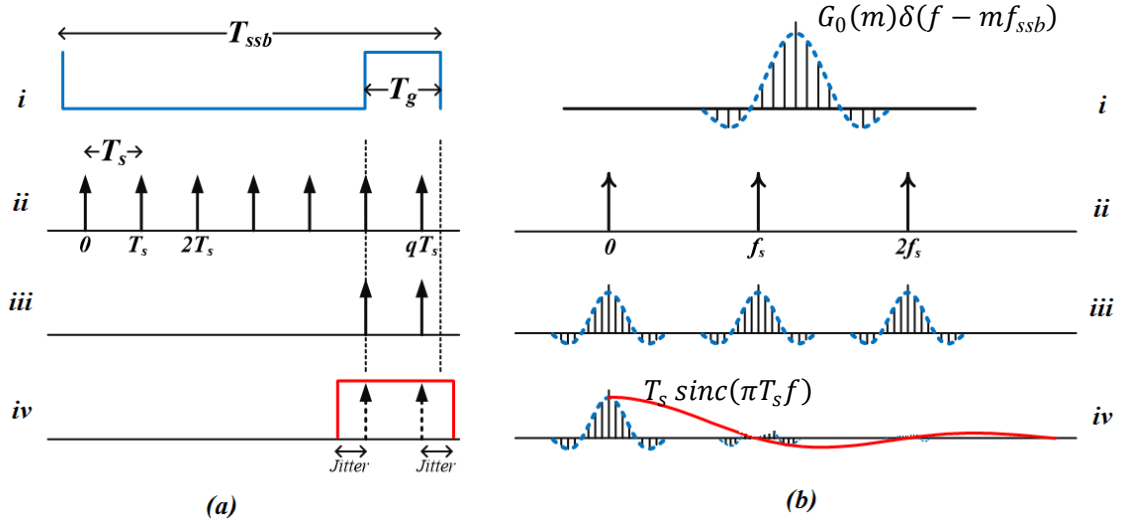


Figure 5.4: The gate signal generation. (a) in time domain, (b) in frequency domain, (i) input signal, (ii) sampling function, (iii) sample image, (iv) $\tilde{G}_0(f)$ output signal.

Figure 5.4(ii) shows the sampling function with period T_s (the sample period of the $\Sigma\Delta$) as a series of impulses, $\sum_{q=0}^{\infty} \delta(t - qT_s)$. The spectrum of the sampling function is also a series of delta functions $\sum_{p=0}^{\infty} \delta(f - pf_s)$. After sampling the gating signal $g_0(t)$ the waveform of Figure 5.4(iii) is obtained. Multiplication in the time domain is equivalent to convolution in the frequency domain, and so the sampled spectrum becomes:

$$\tilde{G}_k(f) = \sum_{p=-\infty}^{+\infty} \sum_{m=-\infty}^{+\infty} G_k(m) \delta(f - mf_{ssb} - pf_s) \quad (5.19)$$

The time domain samples are convolved with a square pulse of width T_s to get the jittered gating window shown in Figure 5.4(iv). In the frequency domain the repeating spectrum is now multiplied by $T_s \text{sinc}\left(\pi \frac{f}{f_s}\right)$; see the red *sinc* shape on Figure 5.4(b)(iv). Therefore, the total spectrum of the sampled gating signal is

$$\tilde{G}_k(f) = T_s \operatorname{sinc}\left(\pi \frac{f}{f_s}\right) \sum_{p=-\infty}^{+\infty} \sum_{m=-\infty}^{+\infty} G_k(m) \delta(f - mf_{ssb} - pf_s) \quad (5.20)$$

or

$$\tilde{G}_k(f) = T_s \operatorname{sinc}\left(\pi \frac{f}{f_s}\right) \sum_{p=-\infty}^{+\infty} \sum_{m=-\infty}^{+\infty} G_0(m) e^{\frac{j2\pi mk}{OSR_{RF}}} \delta(f - mf_{ssb} - pf_s) \quad (5.21)$$

5.3.3 The Convolution of $\tilde{S}_k(f)$ and $\tilde{G}_k(f)$

The reference carrier signal, $s_k(t)$, is now multiplied with the gating signal, $g_k(t)$, to get the intermediate output $y_k(t)$ (Equation 5.8). The convolution in the frequency domain sees the spectrum of $\tilde{G}_k(f)$ with all its sampling images imprinted on each harmonic, nf_c , of the carrier pulse spectrum $\tilde{S}_k(f)$. The convolution of $\tilde{S}_k(f)$ and $\tilde{G}_k(f)$ gives $\tilde{Y}_k(f)$ in Equation 5.23. Finally the total of the spectrum is $\tilde{Y}(f)$ is the sum of each gated phase spectrum of $\tilde{Y}_k(f)$.

Figure 5.5 describes the convolution that gives the spectra of $\tilde{Y}(f)$. Figure 5.5(a) is the series of carrier pulses with digital clock period T_c and with the Fourier transform that gives the harmonics at nf_c weighted by the *sinc* function of $S_0(n)\delta(f - nf_c)$ from Equation 5.10.

Figure 5.5(b) shows an example for the condition $OSR_{RF} = 8$ and $\alpha = 2$ (the pulse width is αT_{clk}). The zero crossing of the *sinc* function, z_c , is at

$$z_c = \frac{1}{\alpha \times T_{clk}} \quad (5.22)$$

or $\pm 4f_c$ for this example.

The spectrum of $\tilde{Y}_k(f)$ is given by the convolution

$$\tilde{Y}_k(f) = \tilde{S}_k(f) \otimes \tilde{G}_k(f) \quad (5.23)$$

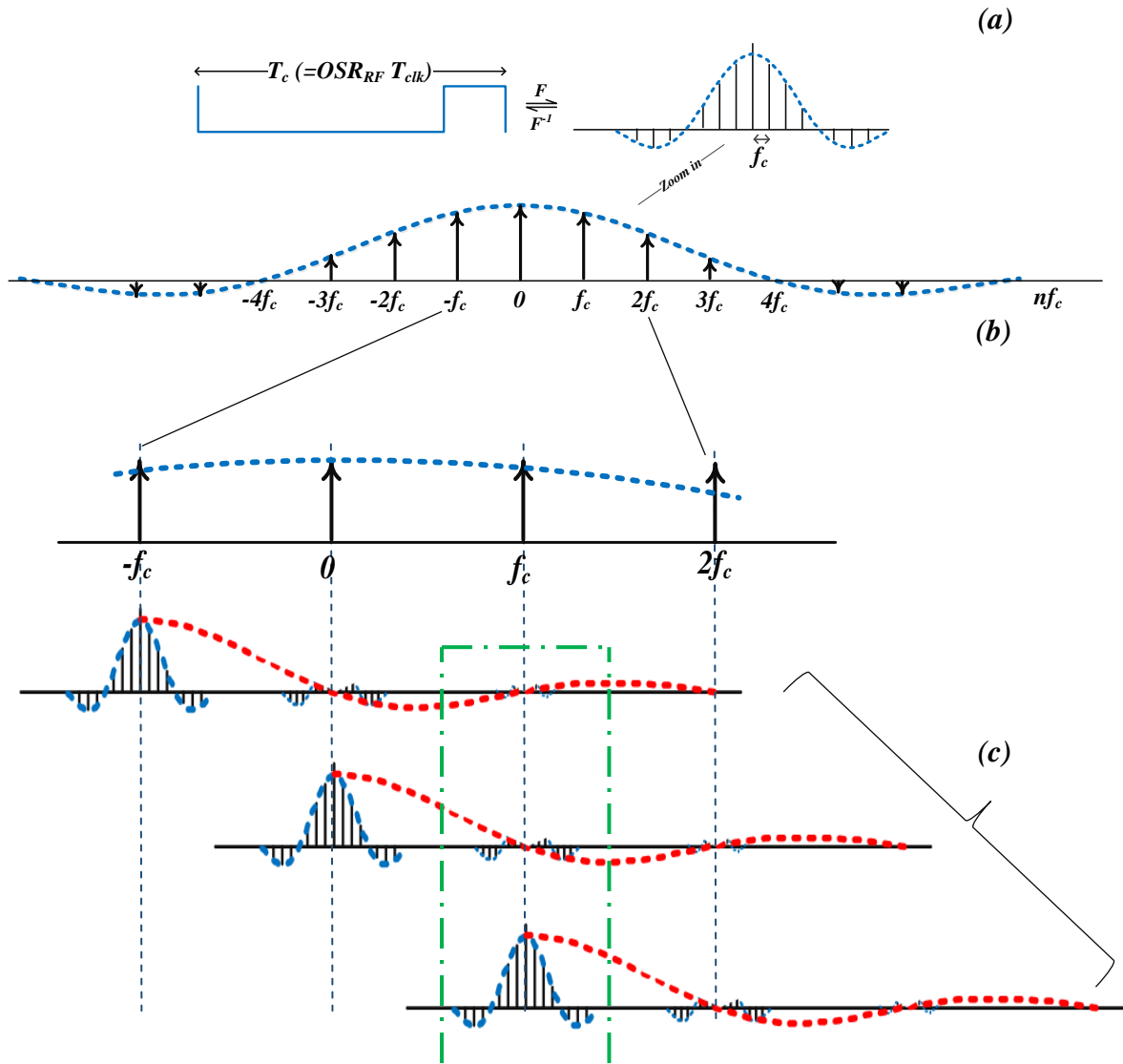


Figure 5.5: The convolution of $\tilde{S}_k(f)$ and $\tilde{G}_k(f)$ gives $\tilde{Y}_k(f)$. (a) $\tilde{S}_k(f)$, (b) zoom of $\tilde{S}_k(f)$ with $OSR_{RF}=8$ and $\alpha=2$, (c) Summation of $\tilde{G}_k(f - nfc)$ that form $\tilde{Y}(f)$.

Substituting Equation 5.15 and Equation 5.21 into Equation 5.23, as a result,

$$\begin{aligned} \tilde{Y}_k(f) = & \sum_{n=-\infty}^{\infty} S_0(n) e^{\frac{j2\pi nk}{OSR_{RF}}} \delta(f - nf_c) \otimes \\ & T_s \operatorname{sinc}\left(\pi \frac{f}{f_s}\right) \sum_{p=-\infty}^{+\infty} \sum_{m=-\infty}^{+\infty} G_0(m) e^{\frac{j2\pi mk}{OSR_{RF}}} \delta(f - mf_{ssb} - pf_s) \end{aligned} \quad (5.24)$$

Or after simplification

$$\tilde{Y}_k(f) = T_s \operatorname{sinc}\left(\pi \frac{f}{f_s}\right) \sum_{p=-\infty}^{\infty} \sum_{m=-\infty}^{+\infty} \sum_{n=-\infty}^{+\infty} S_0(n) G_0(m) e^{\frac{j2\pi(n+m)k}{OSR_{RF}}} \delta(f - nf_c - mf_{ssb} - pf_s). \quad (5.25)$$

where n , m , and p are the harmonic bin number in the spectrum at f_c , f_{ssb} and f_s respectively. The total $\tilde{Y}(f)$ spectrum is the sum of each $\tilde{Y}_k(f)$,

$$\tilde{Y}(f) = \sum_{k=0}^{OSR_{RF}-1} \tilde{Y}_k(f) \quad (5.26)$$

$$\tilde{Y}_k(f) = \sum_{k=0}^{OSR_{RF}-1} T_s \operatorname{sinc}\left(\pi \frac{f}{f_s}\right) \sum_{p=-\infty}^{\infty} \sum_{m=-\infty}^{+\infty} \sum_{n=-\infty}^{+\infty} S_0(n) G_0(m) e^{\frac{j2\pi(n+m)k}{OSR_{RF}}} \delta(f - nf_c - mf_{ssb} - pf_s) \quad (5.27)$$

Since $f_c = K f_s$ (see Equation 3.16) the images sit on top of each other (diagram shows $K = 1$). The signal of interest is sitting at f_c , and the images of interest are shown in the dotted green box in Figure 5.5(c). Moreover, Equation 5.27 can be simplified if the summation of k is implemented first. A harmonic is produced only when $n + m = i \times OSR_{RF}$ where n and m are the sample number harmonics at f_c and f_{ssb} respectively and i is

an integer. The exponential term sums to zero for all other combinations of n and m . Only when $m = (i \times OSR_{RF}) - n$, i.e $e^0 = 1$ the output becomes:

$$\tilde{Y}(f) = \frac{OSR_{RF}}{f_s} \sum_{p=-\infty}^{+\infty} \sum_{n=-\infty}^{+\infty} \sum_{m=-\infty}^{+\infty} S_o(n)G_o(n) \operatorname{sinc} \left(\pi \frac{(f - nf_c)}{f_s} \right) \delta(f - nf_c - mf_{ssb} - pf_s) \quad (5.28)$$

The basic amplitude of the harmonic is given by $\frac{OSR_{RF}}{f_s} S_o(n)G_o(n)$ and the delta function gives its position in the spectrum. The $\operatorname{sinc} \left(\pi \frac{(f - nf_c)}{f_s} \right)$ weighting indicates that the interest in the spectrum is around f_c . Therefore, $nf_c + pf_s = f_c$ gives $K(n - 1) = -p$. This will be substituted into Equation 5.28 that becomes

$$\begin{aligned} \tilde{Y}(f_c + mf_{ssb}) &= \frac{OSR_{RF}}{f_s} \sum_{p=-\infty}^{+\infty} \sum_{n=-\infty}^{+\infty} \sum_{m=-\infty}^{+\infty} S_o(n)G_o(n) \operatorname{sinc} \left(\pi \frac{((f_c + mf_{ssb}) - nf_c)}{f_s} \right) \delta(f - nf_c - mf_{ssb} - pf_s) \\ &= \frac{OSR_{RF}}{f_s} \sum_{p=-\infty}^{+\infty} \sum_{n=-\infty}^{+\infty} \sum_{m=-\infty}^{+\infty} S_o(n)G_o(n) \operatorname{sinc} \left(\pi \left(m \frac{f_{ssb}}{f_c} + (1 - n) \right) K \right) \delta(f - f_c - mf_{ssb}) \end{aligned} \quad (5.29)$$

The list below is a sample calculation that shows the location of the more dominant harmonics:

1. The first harmonic zone (f_c) is the location of the desired main SSB signal with:

$$n = 1, m = -1, p = K(n - 1) = 0.$$

$$\tilde{Y}(f_c - f_{ssb}) = \frac{OSR_{RF}}{f_s} S_o(1)G_o(-1) \operatorname{sinc} \left(-\pi K \frac{f_{ssb}}{f_c} \right) \quad (5.30)$$

$$\text{Relative main} = \frac{\tilde{Y}(f_c - f_{ssb})}{\tilde{Y}(f_c - f_{ssb})} = 1 \quad (5.31)$$

2. The negative harmonic zone ($-f_c$) is the image with:

$$n = -1, m = 1, p = K(n - 1) = -2K.$$

$$\tilde{Y}(f_c + f_{ssb}) = \frac{OSR_{RF}}{f_s} S_o(-1) G_o(1) \text{sinc} \left(-\pi K \frac{f_{ssb}}{f_c} + 2\pi K \right) \quad (5.32)$$

$$\begin{aligned} \text{Relative image} &= \frac{Y(f_c + f_{ssb})}{Y(f_c - f_{ssb})} \\ &= \frac{\text{sinc} \left(-\pi K \frac{f_{ssb}}{f_c} + 2\pi K \right)}{\text{sinc} \left(-\pi K \frac{f_{ssb}}{f_c} \right)} \\ &= (-1)^{2K} \left(\frac{-f_{ssb}}{2f_c + f_{ssb}} \right) \end{aligned} \quad (5.33)$$

3. The third harmonic zone ($f_c - 3f_{ssb}$) is the 3rd harmonic with:

$$n = 3, m = -3, p = K(n - 1) = 2K.$$

$$\tilde{Y}(f_c - 3f_{ssb}) = \frac{OSR_{RF}}{f_s} S_o(3) G_o(-3) \text{sinc} \left(-\pi K \frac{3f_{ssb}}{f_c} - 2\pi K \right) \quad (5.34)$$

$$\begin{aligned} \text{Relative 3}^{rd} \text{ harmonic} &= \frac{Y(f_c - 3f_{ssb})}{Y(f_c - f_{ssb})} \\ &= \frac{S_o(3) G_o(-3) \text{sinc} \left(-\pi K \frac{3f_{ssb}}{f_c} - 2\pi K \right)}{S_o(1) G_o(-1) \text{sinc} \left(-\pi K \frac{f_{ssb}}{f_c} \right)} \\ &= (-1)^{2K} \left(\frac{f_{ssb}}{3f_{ssb} + 2f_c} \right) \left(\frac{\sin \left(\pi K \frac{3f_{ssb}}{f_c} \right)}{\sin \left(\pi K \frac{f_{ssb}}{f_c} \right)} \right) \frac{1}{9} \left(\frac{\sin \left(\frac{3\alpha\pi}{OSR_{RF}} \right)}{\sin \left(\frac{\alpha\pi}{OSR_{RF}} \right)} \right) \left(\frac{\sin \left(\frac{-3\pi}{OSR_{RF}} \right)}{\sin \left(\frac{-\pi}{OSR_{RF}} \right)} \right) \end{aligned} \quad (5.35)$$

4. The negative third harmonic zone ($f_c + 3f_{ssb}$) is the -3^{rd} harmonic with:

$$n = -3, m = 3, p = K(n - 1) = -4K.$$

$$\tilde{Y}(f_c + 3f_{ssb}) = \frac{OSR_{RF}}{f_s} S_o(-3) G_o(3) \text{sinc} \left(\pi K \frac{3f_{ssb}}{f_c} + 4\pi K \right) \quad (5.36)$$

$$\begin{aligned} \text{Relative } -3^{\text{rd}} \text{ harmonic} &= \frac{Y(f_c + 3f_{ssb})}{Y(f_c - f_{ssb})} \\ &= \frac{S_o(-3) G_o(3) \text{sinc} \left(\pi K \frac{3f_{ssb}}{f_c} + 4\pi K \right)}{S_o(1) G_o(-1) \text{sinc} \left(-\pi K \frac{f_{ssb}}{f_c} \right)} \\ &= (-1)^{4K} \left(\frac{-f_{ssb}}{3f_{ssb} + 4f_c} \right) \left(\frac{\sin \left(\pi K \frac{3f_{ssb}}{f_c} \right)}{\sin \left(\pi K \frac{f_{ssb}}{f_c} \right)} \right) \frac{1}{9} \left(\frac{\sin \left(\frac{-3\alpha\pi}{OSR_{RF}} \right)}{\sin \left(\frac{\alpha\pi}{OSR_{RF}} \right)} \right) \left(\frac{\sin \left(\frac{3\pi}{OSR_{RF}} \right)}{\sin \left(\frac{-\pi}{OSR_{RF}} \right)} \right) \end{aligned} \quad (5.37)$$

Table 5.1: Comparison between simulation and calculation of the harmonics size ($K = 1$, $f_{ssb} = 64$ MHz, $OSR_{RF} = 32$, $f_c = 1024$ MHz).

Harmonic size (dB)	Odd quantisation $\alpha = 5$, $\hat{v}_r = 0.6002$		Even quantisation $\alpha = 6$, $\hat{v}_r = 0.7074$	
	Simulation	Calculation	Simulation	Calculation
Image	29.6533	30.3703	29.821	30.3703
3^{rd} harmonic	24.4384	24.9554	26.2643	26.5090
-3^{rd} harmonic	30.1255	30.5955	35.2057	32.1491

Table 5.1 shows the comparison between the simulation results of Figure. 3.10 and the calculation from Equations 5.33 (relative image), 5.35 (relative 3^{rd} harmonic) and 5.37 (relative -3^{rd} harmonic). Two scenarios for the odd quantisation and even quantisation are chosen for this comparison at values of $K = 1$, $f_{ssb} = 64$ MHz, $OSR_{RF} = 32$,

and $f_c = 1024$ MHz. The pulse width, α , is based on Table 3.1 which gives the expected pulse width for a given input signal amplitude. As can be seen the results are close. Agreement between simulation and calculation degrades as OSR_{RF} is reduced. Two reasons for this are the increasing noise floor that masks the signals and the $\Sigma\Delta$ action which oscillates between various pulse widths.

The analysis in this section only applies to a SSB tone with constant amplitude. For modulated signals with varying phase and amplitude, the high order products (3rd harmonic and above) become complex convolutions with smeared spectrum as per Figure 4.2 (for OFDM modulation). A different type of analysis is required for such signals.

5.4 Image Cancellation in a Multi-carrier Environment

When the signal is frequency offset, a number of distortions become visible in the spectrum as previously discussed in Sections 3.5 and 4.3. The distortion products of the image and 3rd harmonic are most dominant in the spectrum. Some of the distortions, the image for instance, can be cancelled by pre-distorting the input signal; however the 3rd harmonic is much more difficult to regenerate. This section demonstrates image cancellation by simulations and physical measurements. All simulations were performed in *MATLAB*®.

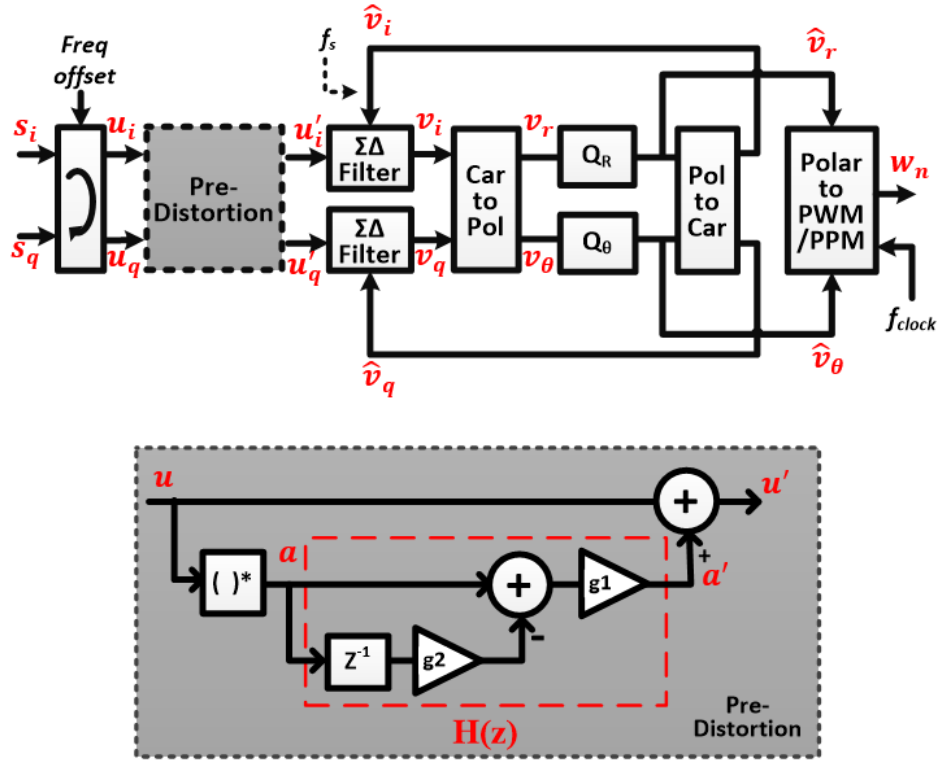


Figure 5.6: The proposed Cartesian $\Sigma\Delta$ architecture with the pre-distortion (top) and the pre-distortion coefficients for image cancellation (bottom).

A block diagram of the proposed Cartesian $\Sigma\Delta$ architecture with the pre-distortion unit is shown in Figure 5.6. The baseband input signal in complex I - Q form, $[u_i, u_q]$ is firstly pre-distorted resulting in $[u'_i, u'_q]$, which is the baseband input into the $\Sigma\Delta$ filter. The goal of the pre-distorter is to generate a $-ve$ image which will cancel the image generated by the 'Polar to PWM/PPM' block after the $\Sigma\Delta$. First the image is generated through the conjugate process, $a = u^*$. Then the image is scaled to the correct amplitude and phase given by Equation 5.33. Since the image magnitude depends on its offset frequency from the nominal f_c , the scaling is frequency dependent, and this is provided by a first order FIR filter, $H(z)$.

5.4.1 Derivation of Pre-distortion Coefficients

The key part to implementing the pre-distortion system into the proposed design, is to calculate the coefficients g_1 and g_2 .

The desired signal is at $f_c + f_{offset}$ (USB), and the image is at $f_c - f_{offset}$ (LSB). In terms of the baseband signal, these frequencies become $+f_{ssb} = +f_{offset}$ and $-f_{ssb} = -f_{offset}$.

The general transfer function of $H(z)$ is defined as

$$H(z) = \frac{A'(z)}{A(z)} = (1 - z^{-1}g_2) g_1 \quad (5.38)$$

The frequency response can be expressed by substituting $z = e^{j\omega T_s} = e^{j2\pi \frac{f_{ssb}}{f_s}}$. Therefore it can be substituted into Equation 5.38, to give

$$H(j\omega) = \left(1 - e^{-j2\pi \frac{f_{ssb}}{f_s}} g_2\right) g_1 \quad (5.39)$$

When $g_2 \cong 1$ this becomes a high pass filter, with an output that is dominated by an imaginary component that grows linearly with frequency. The relative image is given by $\frac{f_{ssb}}{2f_c - f_{ssb}}$ (from Equation 5.33). Therefore, the expression Equation 5.39 can be written

by

$$\left(1 - e^{-j2\pi \frac{f_{ssb}}{f_s}} g_2\right) g_1 = \frac{f_{ssb}}{2f_c - f_{ssb}} \quad (5.40)$$

If g_2 is selected to make the term in the parenthesis purely imaginary at the nominal f_{ssb} then

$$g_2 = \frac{1}{\cos(2\pi \frac{f_{ssb}}{f_s})} \quad (5.41)$$

now we can obtain a simplified value of g_1 , to give the correct scaling

$$g_1 = \frac{\frac{f_{ssb}}{2f_c - f_{ssb}}}{-j \tan(2\pi \frac{f_{ssb}}{f_s})} \quad (5.42)$$

By keeping g_1 and g_2 either real or imaginary the use of a full complex multiply is avoided.

5.4.2 Simulation Results

Using a pre-distorted signal at the input of the $\Sigma\Delta$ filter allows the formation of the cancelling image by the generation of a duplicate conjugate signal. There are two simulation scenarios based on the proposed model that have been discussed in Chapter 4. They are: image cancellation for baseband tuning and image cancellation for IF tuning.

A QPSK-modulated OFDM input signal was used to test the architecture. The OSR_{RF} is 16 and defines the sampling frequency of the $\Sigma\Delta$ modulation. The OFDM signal has 8 subcarriers rather than the normal 64, to limit the PAPR ratio to 9 dB, reduce simulation times, and meet memory requirements of the laboratory test equipment. It is anticipated that the performance would be similar to a WiFi signal with PAPR restricted to 9 dB. The signal was shifted by one channel to examine the resultant spectral images.

5.4.2.1 Image Cancellation for Baseband Tuning

The block diagram used is the proposed Cartesian $\Sigma\Delta$ in Figure 5.6. Figure 5.7(a) shows the baseband spectrum of the pre-distortion process. It shows the baseband input spectrum $U(f)$ shifted by $f_{ssb} = 30$ MHz. The complex conjugate of baseband $U(f)$ is the image $A(f)$. Both $A(f)$ and $U(f)$ have the same real part but with the imaginary parts

of equal magnitude and opposite signs. $A'(f)$ is the scaled frequency response when the transform function $H(z)$ is applied. The spectrum $U'(f)$ contains both the original signal and the scaled image. Figure 5.7(b) shows the spectra at various points of the Cartesian $\Sigma\Delta$ upconversion scheme. $V_{IQ}(f)$ and $\hat{V}_{R\theta}(f)$ are the baseband spectra, output from $\Sigma\Delta$ filters and quantiser respectively (Figure 5.6). $V_{IQ}(f)$ has a high noise floor that partially masks the image. After the quantiser, $\hat{V}_{R\theta}(f)$ has a much lower noise floor due to the $\Sigma\Delta$ suppression, and the image is clearly visible. Finally $W(f)$ is the RF spectrum after ‘Polar to PWM/PPM’ block in which it is shown that the image has been fully cancelled, however the 3rd harmonics are still present.

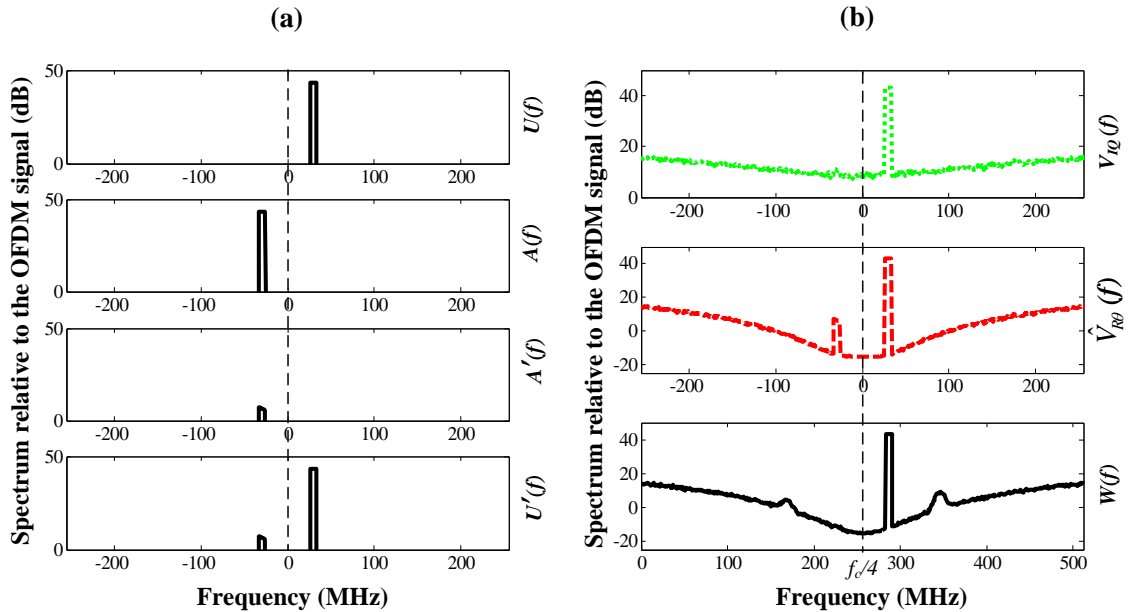


Figure 5.7: Image cancellation using baseband tuning with $OSR_{RF}=16$.
 (a) Spectrum at the pre-distortion unit. (b) Spectrum at $V_{IQ}(f)$, $\hat{V}_{R\theta}(f)$ and $W(f)$.

5.4.3.2 Image Cancellation for IF Tuning

Figure 5.8 (top) shows the block diagram scheme for image cancellation using Cartesian $\Sigma\Delta$ with baseband tuning. As for the first scenario (baseband tuning), the pre-

distorted signal is part of the input to the $\Sigma\Delta$ filter. However, the shaping is different because of the additional rotation of the IF frequency inside the $\Sigma\Delta$. The shaping should be for $f_{ssb} = f_{offset} + f_{IF}$ instead of $f_{ssb} = f_{offset}$ as used in the first scenario. An additional rotation of f_{IF} is applied to the pre-distorted input signal prior to image generation and spectral shaping, $H(z)$. This would produce the correct frequency response slope of the image prior to cancelling. The frequency shift is reversed prior to summing with the desired signal.

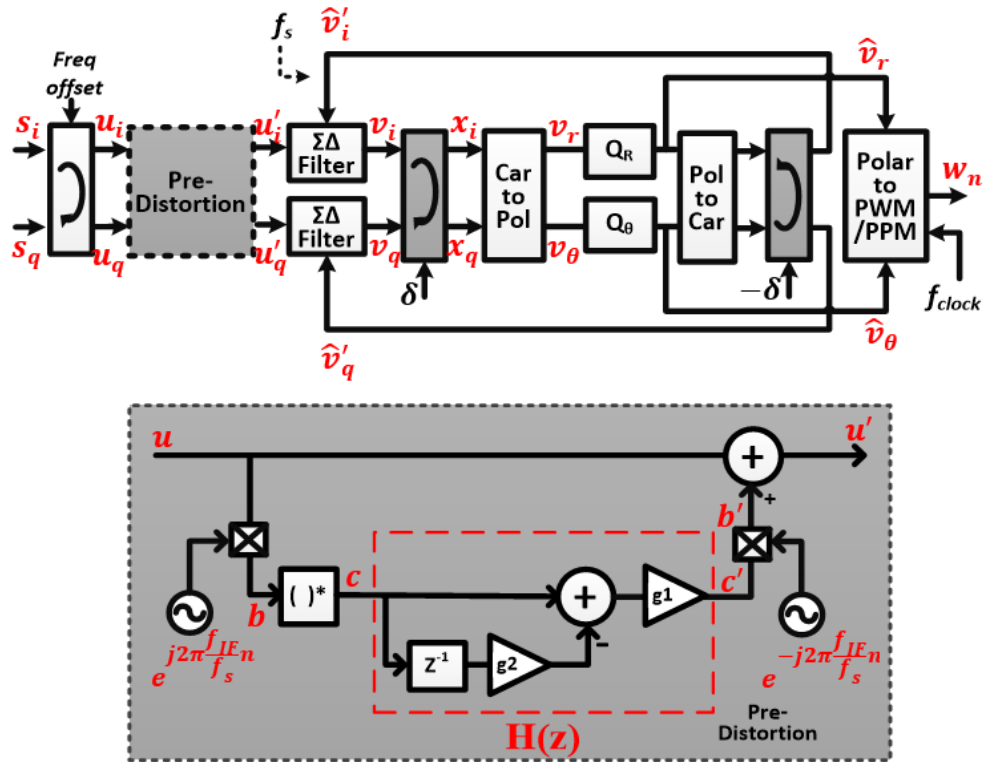


Figure 5.8: Pre-distortion for IF tuned Cartesian $\Sigma\Delta$ architecture (top). The pre-distorter architecture for image cancellation (bottom).

Figure 5.9 shows the spectra from the pre-distortion unit. For comparison purposes, there are three different spectrum plots corresponding to three different values of f_{offset} and f_{IF} . The frequency response of $U(f)$, $B(f)$, $C(f)$, $C'(f)$, $B'(f)$ and $U'(f)$ are

the spectra at points u , b , c , c' , b' and u' respectively from Figure 5.8. $U(f)$ is the input baseband, which includes any offsets, f_{offset} . When $f_{IF} = 0$, Figure 5.9(a) has the same outcome as the first scenario for baseband tuning. The complex coefficient, $e^{j2\pi\frac{f_{IF}}{f_s}n}$ is only active when f_{IF} is applied. Figure 5.9(b) shows the condition $f_{IF} = 50$ MHz and $f_{offset} = 0$ MHz. $U(f)$ shows the signal baseband; $B(f)$ shows the frequency shift of f_{IF} ; $C(f)$ shows the signal in the image position at $-f_{IF}$; $C'(f)$ shows the spectral shaping of the filter $H(z)$; $B'(f)$ shows the removal of f_{IF} which causes the image sit as $-2f_{IF}$; $U'(f)$ is the composite signal provided to the $\Sigma\Delta$. Figure 5.9(c) shows the combination of both f_{IF} and f_{offset} . In this way, the image enters the shaping filter at $f_{ssb} = f_{offset} + f_{IF}$ to give a relative image gain of

$$\frac{f_{ssb}}{2f_c - f_{ssb}} = \frac{f_{offset} + f_{IF}}{2f_c - (f_{offset} + f_{IF})} \quad (5.43)$$

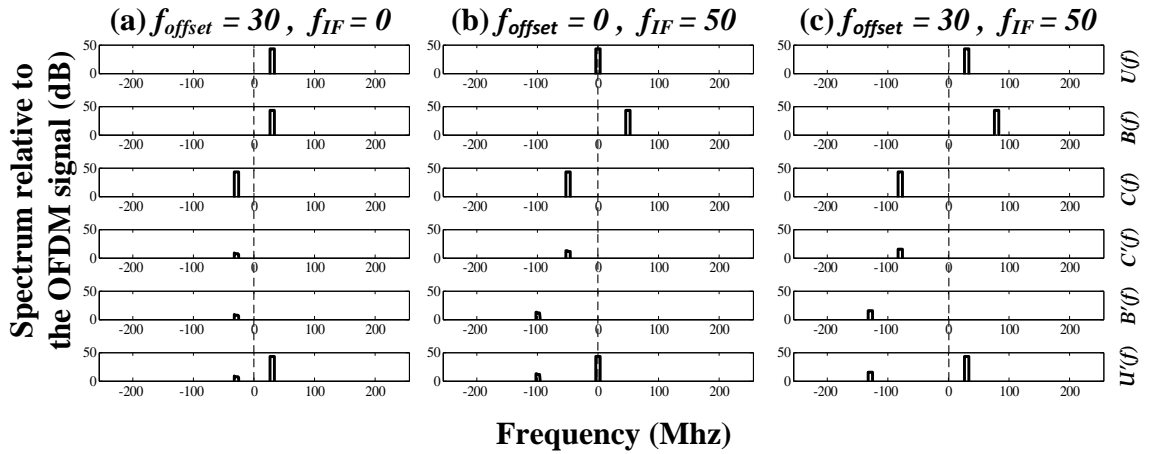


Figure 5.9: Spectrum at the pre-distortion unit for IF tuning with $OSR_{RF} = 16$. Three different f_{offset} and f_{IF} scenarios are compared.

Figure 5.10 shows the spectrum results with image cancellation applied as per the example scenarios of Figure 5.9. $V_{IQ}(f)$ is the spectrum after the $\Sigma\Delta$ filter and has the

shape of the input spectrum $U'(f)$ with a high noise floor. $X(f)$ is the spectrum after applying the f_{IF} rotation which moves the desired signal and image into the correct frequency location. $\hat{V}_{r\theta}(f)$ is the spectrum at the quantiser output and shows a reduced noise floor due to the $\Sigma\Delta$ action. $W(f)$ shows the spectrum of RF PWM/PPM signal with the image cancelled but the 3rd harmonics still present. Note: the PWM/PPM process increases the noise floor near the signal compare to $\hat{V}_{r\theta}(f)$ in case-*b* and case-*c*.

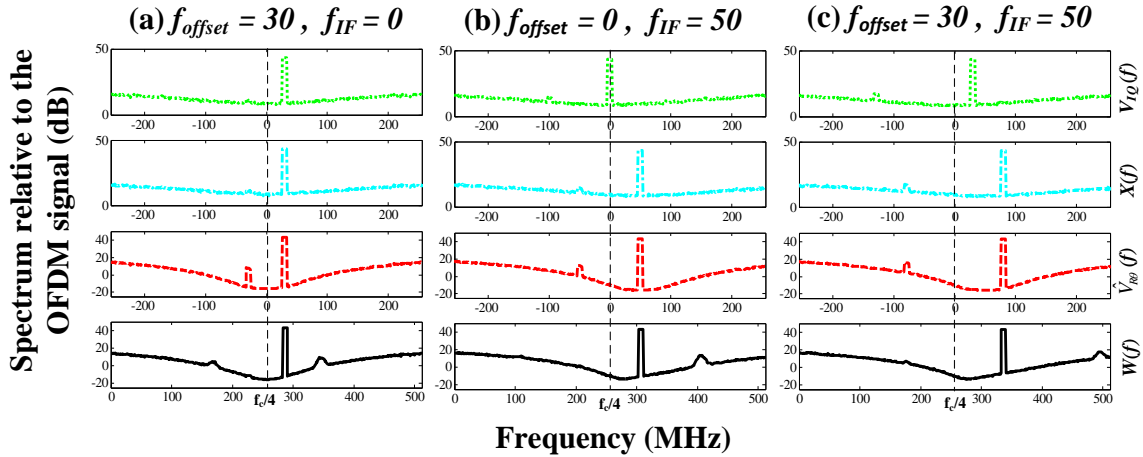


Figure 5.10: Image Cancellation for IF tuning with $OSR_{RF}=16$. The three different f_{offset} and f_{IF} scenarios are shown for comparison.

5.4.3 Measurement Results

The experimental setup for measurement is similar to the physical measurement setup procedure that was explained in Chapter 3 (Section 3.7).

Figure 5.11 shows the spectrum measurement for $OSR_{RF}=16$ and $f_{offset}=30$ MHz. The figure on the left shows that the image still appears on the spectrum (before image cancellation) whereas the figure on the right shows that the image no longer appears after image cancellation. Since $f_{ssb}=30$ MHz is positive, the desired signal is USB and the

image is LSB. Figure 5.12 shows the opposite of Figure 5.11 with the signal of interest at $f_{offset} = -30$ MHz. It is quite evident that the image can be cancelled from the band of interest, however the noise lumps at the extreme of the frequency spectrum are the 3rd order distortion, which remain.

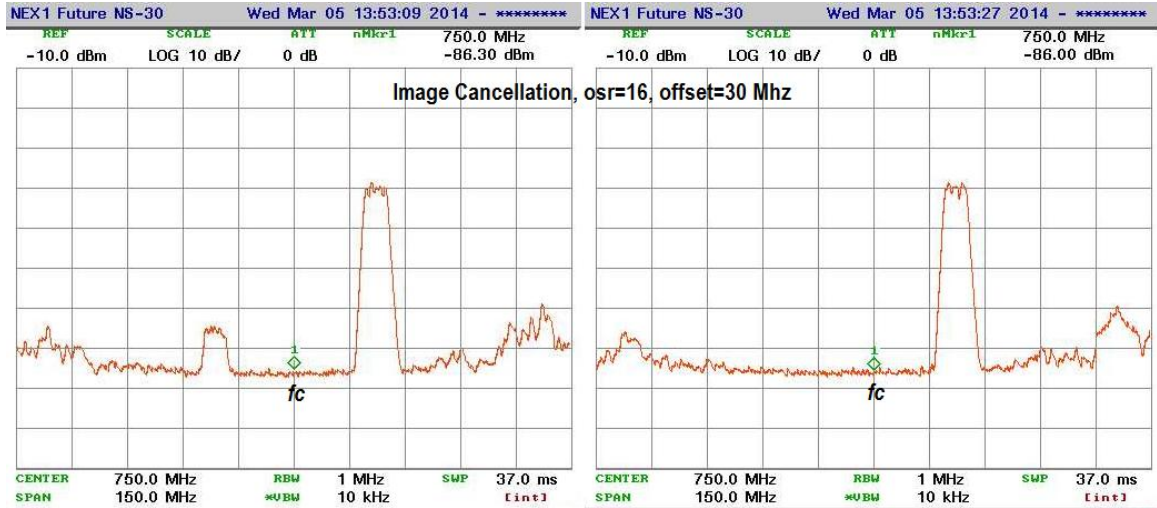


Figure 5.11: The desired signal (USB) and the image (LSB). Image cancellation, before (left) and after (right). $f_{offset} = 30$, $OSR_{RF} = 16$.

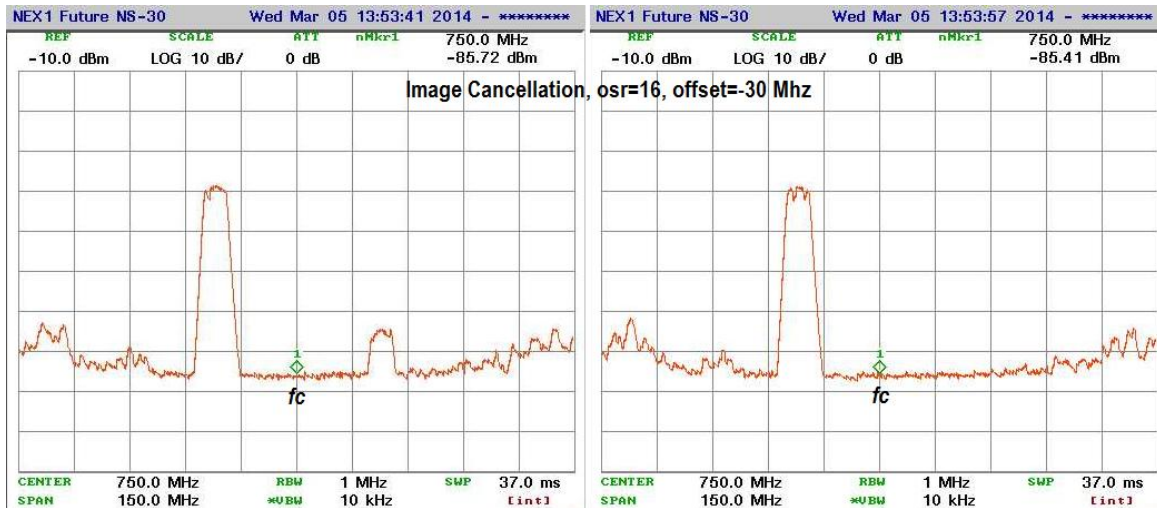


Figure 5.12: The desired signal (LSB) and the image (USB). Image cancellation, before (left) and after (right). $f_{offset} = 30$, $OSR_{RF} = 16$.

5.5 Noise Cancellation in a Multi-carrier Environment

The noise floor increase around the desired channel during f_{IF} application is now discussed. Although the image has been removed and other distortions have been moved away, the band of interest is no longer in such a deep $\Sigma\Delta$ noise null due to the action of the ‘Polar to PWM/PPM’ block. These noise (and distortion) components partially destroy the good in-band noise shaping performance of the $\Sigma\Delta$ filters. The noise floor around the band of interest increases significantly when applying large f_{IF} . The RF spectrum in Figure 5.13 describes the different offset frequencies f_{offset} at $f_{IF}=110$ MHz. It shows that the noise floor problem affects the area of the band of interest. The spectrum of the quantised $\Sigma\Delta$ feedback signal \hat{v}' (green dash line) shows the reference output spectrum frequency aligned with the PWM/PPM output RF signal (black). The RF spectrum should have the same noise shaping but has up to a 10 dB worse noise floor. The additional noise folds are from the image and other distortion products. The problem was also identified in [91] for a burst-mode PWM modulation and solved by adding a fractional delay in the feedback circuit. In this sub-section we cancel the image noise by generating an inverse copy using a post-distortion network after the quantiser.

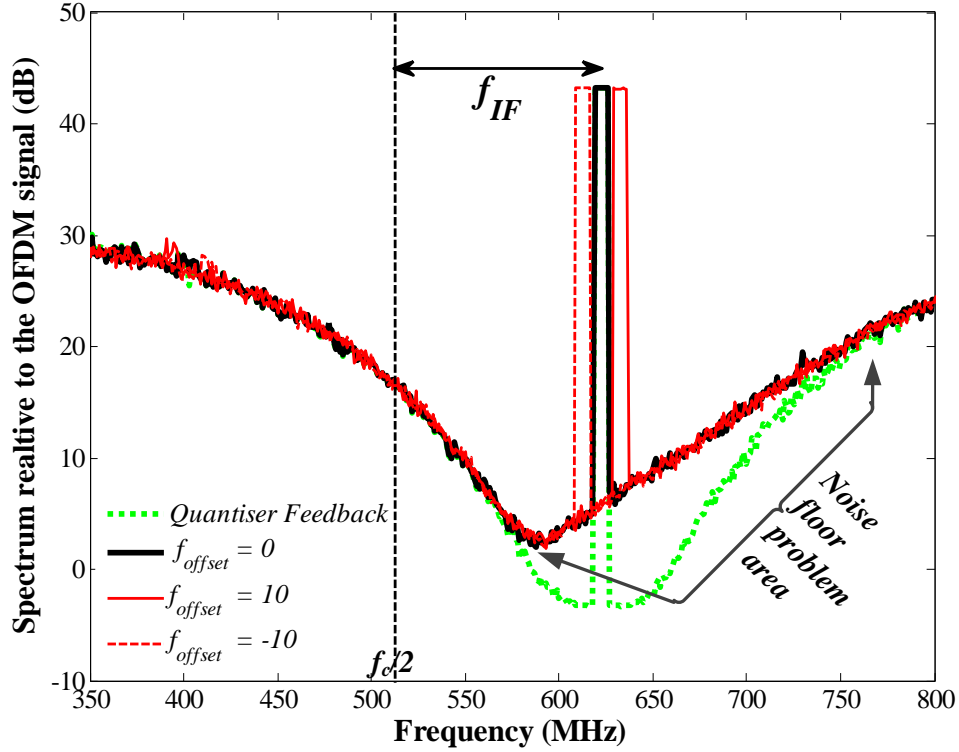


Figure 5.13: Noise floor problem around the band of interest for $OSR_{RF} = 4$.

Figure 5.14 shows the proposed scheme for IF tuning of noise cancellation. The post-distortion function unit is put at the output of the quantiser but before the $-\delta$ rotation in the feedback path. The post-distortion function unit is the same as that used in Section 5.4. The conjugation operation, $d = \hat{y}^*$ generates the image and the g_1 and g_2 network gives the correct frequency scaling. Applying the post-distortion unit in polar format is also possible.

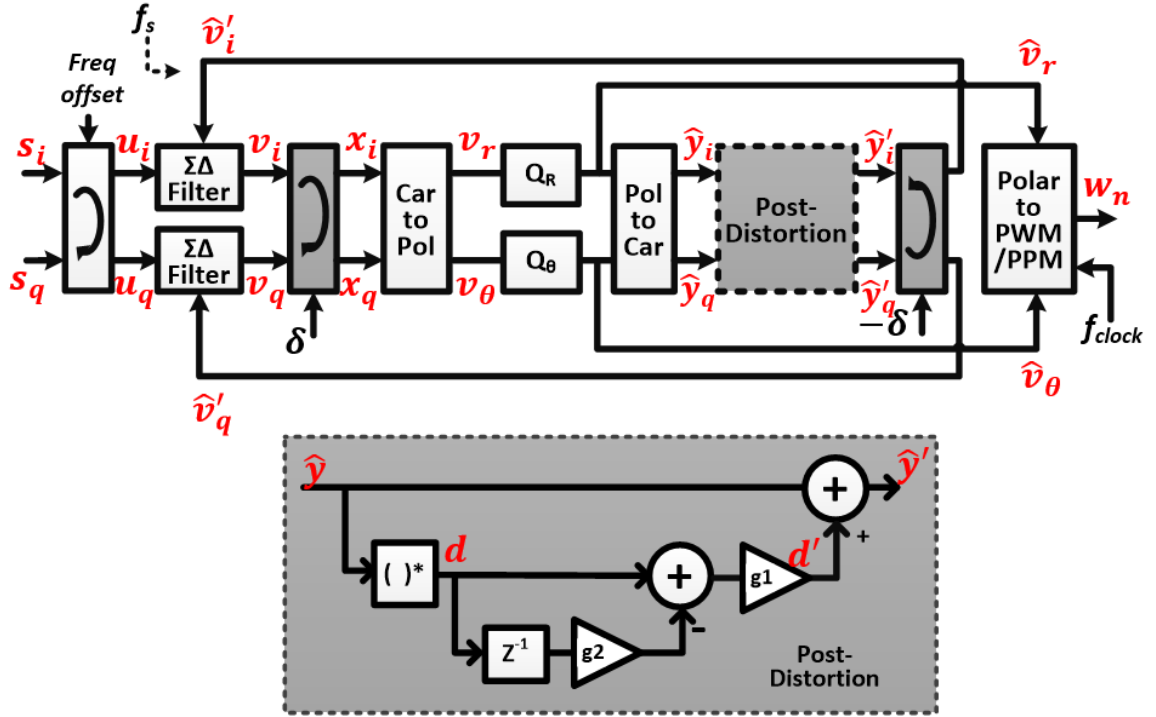


Figure 5.14: The proposed IF tuning with the post -distortion (top) and the post-distortion coefficients for noise cancellation (bottom).

Adding additional processing in the feedback is generally not a good idea from an implementation perspective. The post-distortion circuit increases the loop delay and reduces the maximum sample rate, f_s . However careful observation of the two processing blocks after the quantiser, shows that the input signal signals are quantised to $OSR_{RF} \times (\frac{OSR_{RF}}{2} + 1)$ possible values. Since there is one memory (z^{-1}) in the post-distortion unit then the combined ‘Polar-to-Cartesian’ and ‘Post-Distortion’ blocks can be implemented in a LUT with $(OSR_{RF} \times (\frac{OSR_{RF}}{2} + 1))^2$ entries, or just 144 entries for $OSR_{RF}= 4$.

5.5.1 Simulation Results

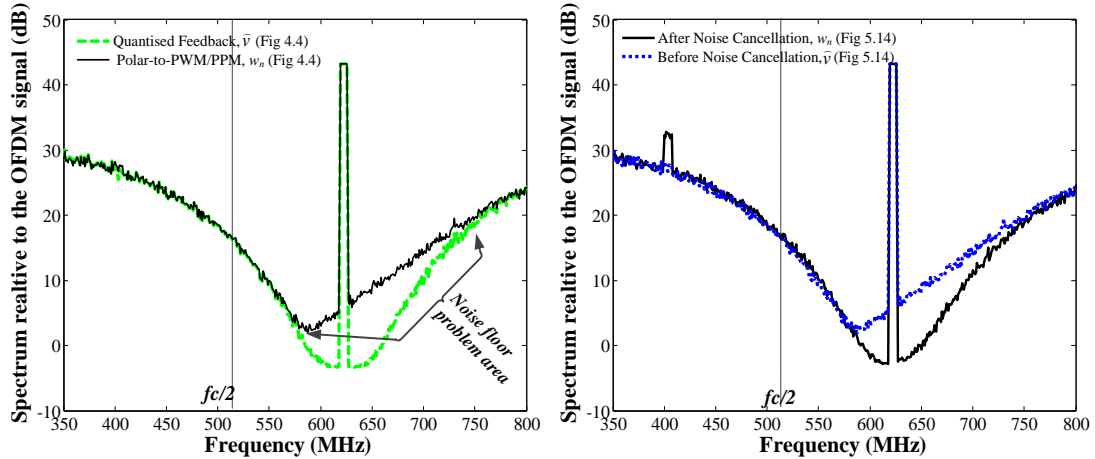


Figure 5.15: Noise cancellation for IF tuning for $OSR_{RF}=4$. The original spectrum before noise cancellation (left) and the spectrum after noise cancellation (right). The image is increased when the noise floor is cancelled (right black).

The simulation results are shown in Figure 5.15. In Figure 5.15 (left), the original spectrum before applying post-distortion noise cancellation shows that the spectrum of the ‘Polar to PWM/PPM’ output (black) has an increased noise floor around the band of interest. The signal image and other distortion products do not appear due to the high noise floor caused by coarse quantisation from the low over sampling ($OSR_{RF}=4$). Figure 5.15 (right), shows significant reduction in the noise floor (right black) which has a similar noise shape to the spectrum of the quantised $\Sigma\Delta$ signal, \hat{v} of Figure 4.4 (dash green). Interestingly, the \hat{v} signal after post-distortion of Figure 5.14 (dash blue) has a very similar noise shape of the ‘Polar to PWM/PPM’ spectrum before the noise floor is cancelled (left black). This is expected since it contains the inverse noise signal that will cancel the PWM to PPM generated image noise.

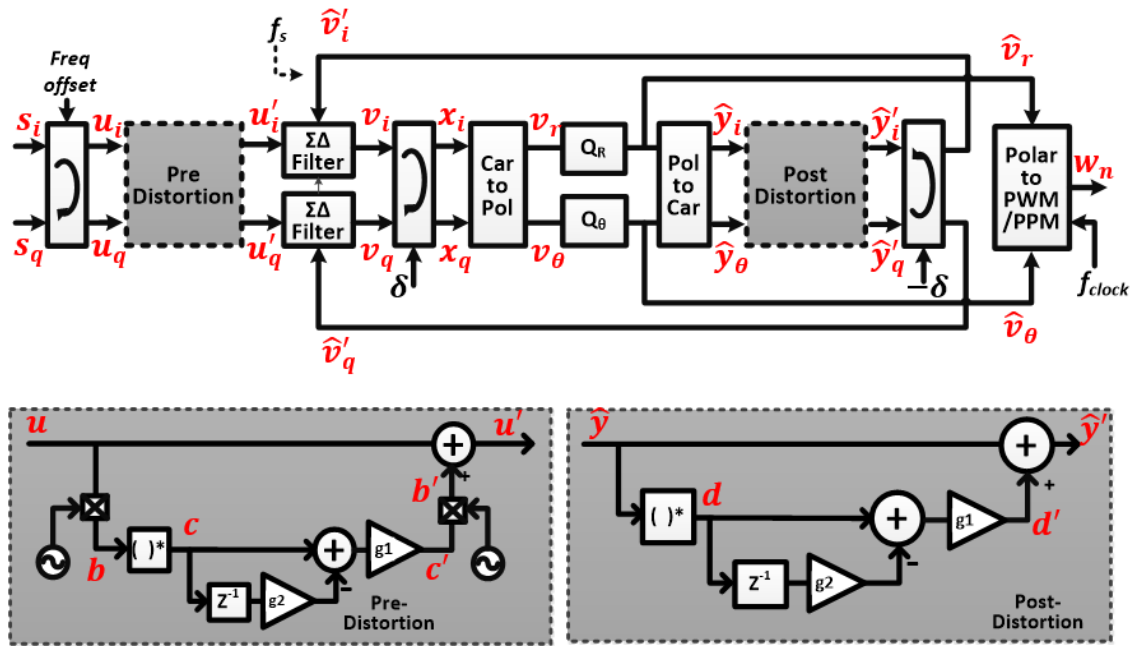


Figure 5.16: Image and Noise cancellation for IF tuning. Post-distortion for noise cancellation and pre-distortion for image cancellation.

An undesirable by-product of using post-distortion to cancel the image noise is a further increase in the signal image, since the signal also goes through to feedback post-distortion network. As can be seen in Figure 5.15 (right), the black spectrum shows the visibility of the image after noise cancelling. Therefore, the proposed scheme needs to have two distortion function units: post-distortion for noise cancellation and pre-distortion for image cancellation, see Figure 5.16.

In Figure 5.16, the first pre-distortion function unit is for image cancellation. It is put at the input to the $\Sigma\Delta$. The second post-distortion function unit is for noise cancellation. Figure 5.17 shows both the image and the noise floor have been cancelled allowing the spectrum to be located at the noise floor null.

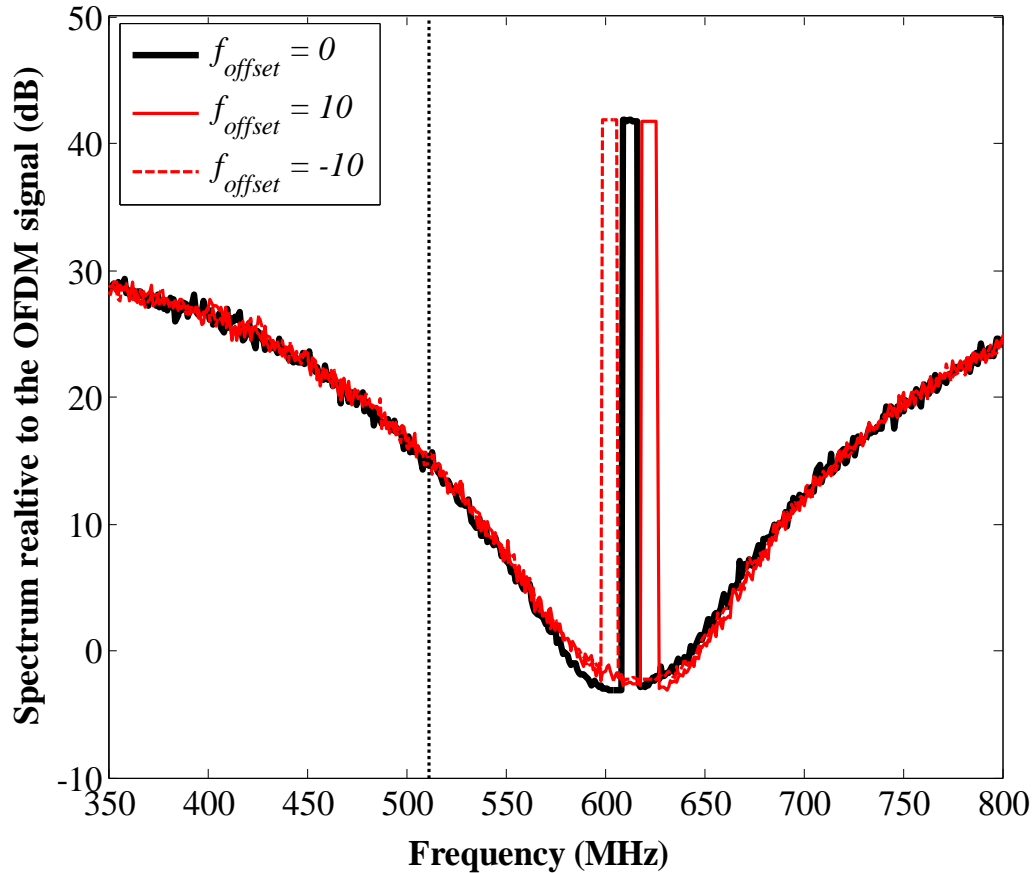


Figure 5.17: Spectrum of the image and noise cancellation for $OSR_{RF}=4$.

5.5.2 Measurement Results

The measurement setup follows a similar procedure to the other measurement schemes in this thesis. Figure 5.18 (left) shows the original spectrum in which the noise floor is high near the signal. Figure 5.18 (right) shows the spectrum with noise cancellation. It is evident that the noise floor is reduced and the signal band is in the $\Sigma\Delta$ noise null.

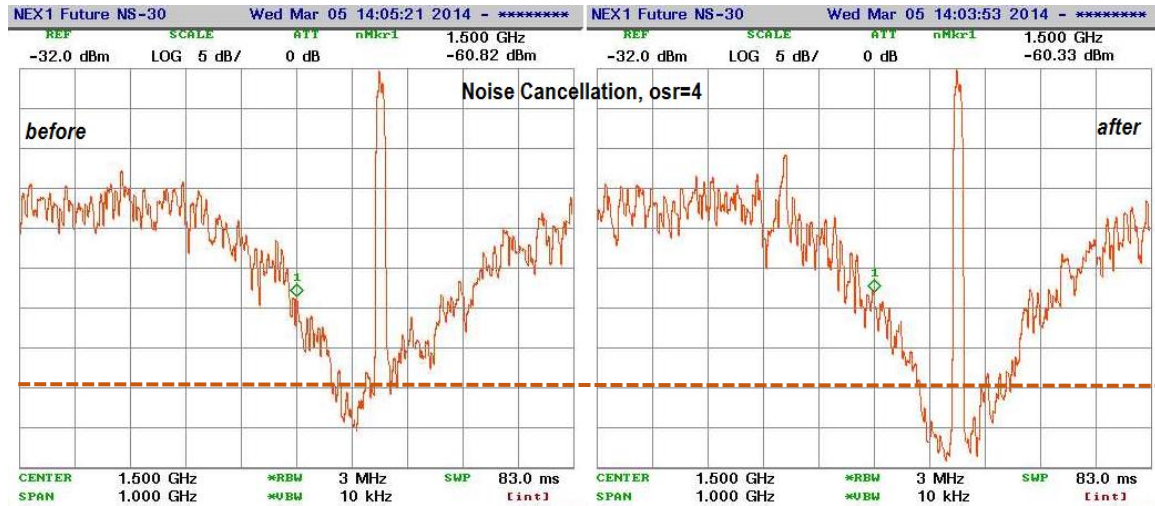


Figure 5.18: Measurement results of noise cancellation for IF tuning. $OSR_{RF}=4$. The marker is at the nominal carrier frequency, f_c .

5.5.3 Correction at Higher OSR

The previous sub section showed the image of the noise cancellation in an $OSR_{RF}=4$. Image cancellation system at high or OSRs is less effective because noise and distortion folding in-band from higher order products dominate. These products include the 3^{rd} 's and -3^{rd} 's which, can have similar or larger amplitudes to the image signal as indicated by Table 5.1 for an SSB tone. Figure 5.19 illustrates the problem for $OSR_{RF}=8$. These are only about 1 dB of improvement. The quantised feedback with noise cancellation shows only a small increase in noise over the ideal quantised feedback, indicating the inverse image noise is not large enough to completely cancel the noise generated in the 'Polar to PWM/PPM' block. Clearly there are other noise and distortion sources generated by the PWM/PPM process that need to be modelled to further improve the cancellation.

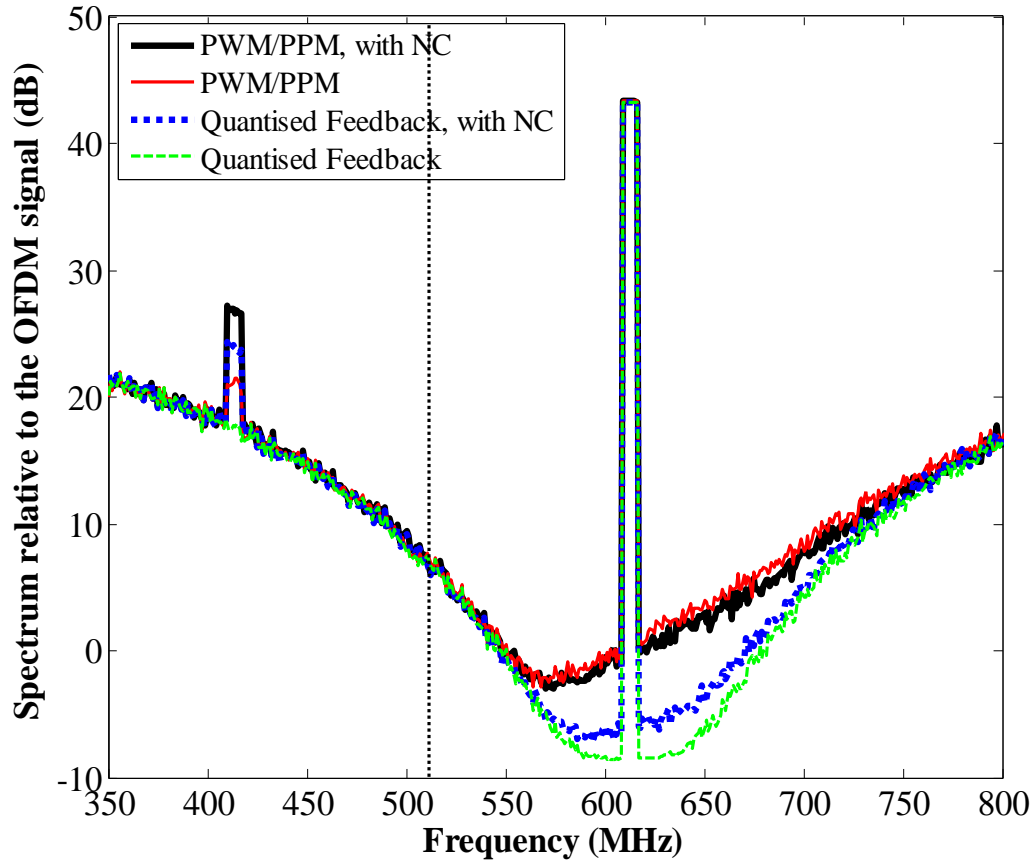


Figure 5.19: The spectrum with after and before noise cancellation (NC) for $OSR_{RF}=8$.

5.6 Summary

This section has identified the phenomenon of distortion problems that are generated by the ‘Polar to PWM/PPM’ block. The rectangular nature of the output PWM/PPM pulse generates a number of unwanted harmonics and distortion products such as the image and 3rd harmonics which are the most dominant. These distortions reduce the dynamic range of the operating band, therefore, image and noise cancellation by using pre-distortion technique is proposed so all the operating bands can meet the spectrum mask requirements.

In this chapter the mathematical expression from [79] has been modified to predict the amplitude and frequency of the distortion products from a SSB input signal at any offset frequency. With this mathematical analysis, the structure of the distortion is known. The location of the image and the $\pm 3^{\text{rd}}$ harmonic are established in this investigation. Image generation using pre-distortion is easy to predict since its location is exactly symmetric with the desired signal. However, the $\pm 3^{\text{rd}}$ harmonics are much more difficult to generate. They involve a complex generation function involving multiple convolutions, which is not in the scope of this thesis. ‘IF-tuning’ frequency shifts both the signal and the noise null together, but the final PWM/PPM processes generates an image of both the noise and signal, which results in a higher than expected noise floor and a spurious image. Image and noise cancellation are proposed to solve this problem.

The simulation and measurement results show that nulling the baseband channel is now possible, however it only works with $OSR_{RF}=4$. Even so, $OSR_{RF}=4$ will meet WLAN out-of-band specification (-40 dB ACP) over a bandwidth of 5% of the carrier frequency (30 MHz/600 MHz from Figure 5.1).

Chapter 6

Conclusion and Further Research

6.1 Conclusion

In this thesis, the focus was on a concept design for a low-power transmitter with good linearity and high efficiency. The work concentrated on the digital upconversion of modulated signals such as required for LTE and WLAN standards. A number of improvements were developed for the Cartesian $\Sigma\Delta$ upconverter architecture. The proposed scheme is potentially an all-digital and therefore low-cost solution for multi-standard SDR.

In the literature review of Chapter 2, traditional and switched-mode power amplifiers are studied. To support the idea of a Cartesian $\Sigma\Delta$ upconverter, the basic concepts of $\Sigma\Delta$ systems were investigated and the methodology for designing the $\Sigma\Delta$ filters explained. This is followed by an overview of transmitter architecture designs

suitable for today's modulation schemes. Key results from [31, 76, 79, 90], on which this work is based, were emphasized.

The improvement to the proposed Cartesian $\Sigma\Delta$ upconverter quantisation scheme is explained in Chapter 3. The first contribution is the development of the odd quantisation scheme which reduces quantisation noise, particularly at low signal levels. A constant phase reference is maintained whatever the pulse widths. An analysis of the noise and distortion products of the odd quantisation compared to the even quantisation schemes was investigated. It is shown that both schemes produce the same distortion products that increase with frequency offset. The odd quantisation scheme, however, has an improved SNR by approximately 2 dB. In both cases separate quantisers for amplitude and phase enable simple implementation. The work was extended to joint-quantisation, which uses both odd and even pulse widths and gives a 5 dB reduction in noise floor. The best quantiser for joint quantisation does the quantisation of the odd and even points separately and then selects the closest point to the input signal vector.

A key radio transmitter requirement is the ability to tune to different channels in the transmission band. Chapter 4 describes alternative tuning methods that do not require changing the clock frequency. Many digital $\Sigma\Delta$ -RF upconverters have poor performance when the carrier frequency is tuned away from the centre of the band. The offsetting of signals from the nominal carrier frequency position generates unwanted distortion products which are dominated by the image and 3rd harmonics. It is shown that these products can be moved out of band by the correct choice of intermediate frequency (f_{IF}). A novel technique for shifting both the signal and the noise null to the new frequency position is explained and performed. The new method involves additional phase rotators

before and after the quantiser. There is a reducing SNR with increasing offset that limits the amount of practical frequency shift.

In Chapter 5, the focus was on methods to eliminate noise and distortion products caused by the tuning process. Firstly the phenomenon of unwanted spectral components generated by the ‘polar to PWM/PPM’ block was analysed using a mathematical approach. The extension of the mathematical derivation in [79] achieved results over a continuous frequency range rather than at a few spot frequencies. The new mathematical approach enabled the derivation of a new pre-distortion function unit and post-distortion function unit that predicted the size of the image signal and the image noise components. Image cancellation and noise cancellation techniques are presented in order to solve the image problem. Measurements are made and compared with computations to test the reliability, accuracy and validity of the developed formulations.

6.2 Further Research

6.2.1 Third Harmonic Cancellation

Image generation by using pre-distortion is easily achieved since the image is exactly symmetric with the desired signal about the nominal carrier frequency. However, the $\pm 3^{\text{rd}}$ harmonics are much more difficult to generate in pre-distortion because the distortion is spread over a number of channels. Therefore, in future work, research should look at removing these distortion products with emphasis on the dominant harmonics such as $\pm 3^{\text{rd}}$ harmonics and $\pm 5^{\text{th}}$ harmonics. The cancellation scheme should consider

using the extended mathematical analysis in Chapter 5 with multi-carrier signals as a starting point.

6.2.2 FPGA Implementation

To demonstrate the schemes' viability, implementing a prototype in digital hardware using a Field-Programmable Gate Array (FPGA) is suggested. FPGA implementation can prototype the proposed structure. This part is important for finding an accurate power and efficiency estimation of the proposed transmitter.

6.2.3 Increased Power Outputs

To improve the applicability of the scheme, high output powers are needed. This includes developing a suitable SMPA scheme for interfacing to the FPGA. At this stage the lack of high speed high power switching devices makes this structure not suitable for traditional wireless communications. The output power of ~8 GHz high speed logic device driving 50 Ohms with a 1 Volt swing is $\frac{1}{50}$ Watt. When this is included with a coding efficiency of 8% for an OSR_{RF} of 8 [32] and an OFDM signal with a PAPR of 8 (9 dB) the RF output power is $\frac{1}{50} \times 0.08 \times \frac{1}{8} = \frac{1}{5}$ mW or -7 dBm. The efficiency would be small ($\ll 1\%$) because of the large FPGA power overhead. Output power must be increased to improve efficiency. With today's devices this can only be achieved at lower carrier frequencies, requiring lower speed devices. It might be possible to achieve carrier frequencies of the order of 10 MHz to 100 MHz using high power GaN devices to switch amps of current at sub-ns speeds. This is left for future work.

References

- [1] "Sustainable energy use in mobile communications," White Paper, Ericsson Inc., Aug. 21, 2007.
- [2] S. Vadgama, "Trends in Green Wireless Access," *FUJITSU Sci. Tech. Journal*, vol. 45, pp. 404-408, 2009.
- [3] D. W. Alan Solheim. (Mar. 19, 2014). *Microwave Backhaul Radios Meet The Evolving Traffic Challenge*. [Online] Available: <http://mobiledevdesign.com/learning-resources/microwave-backhaul-radios-meet-evolving-traffic-challenge>
- [4] K. Young Kyun and R. Prasad, "4G Roadmap and Emerging Communication Technologies," Artech House 2006, ISBN 1-58053-931-92006.
- [5] Y. Kim, B. J. Jeong, J. Chung, C.-S. Hwang, J. S. Ryu, K.-H. Kim, *et al.*, "Beyond 3G: vision, requirements, and enabling technologies," *IEEE Communications Magazine*, vol. 41, pp. 120-124, 2003.
- [6] E. Bohlin, J.-C. Burgelman, and C. R. Casal, "The future of mobile communications in the EU," *Telematics and Informatics*, vol. 24, pp. 238-242, Aug. 2007.
- [7] S. Frattasi, H. Fathi, F. H. Fitzek, R. Prasad, and M. D. Katz, "Defining 4G technology from the users perspective," *IEEE Network*, vol. 20, pp. 35-41, 2006.

REFERENCES

- [8] S. Frattasi, R. Olsen, and M. Sanctis, "Innovative Services and Architectures for 4G Wireless Mobile Communication Systems," in *Proc. of IEEE ISWCS*, Siena, Italy, 2005.
- [9] R. Bolla, R. Bruschi, F. Davoli, and F. Cucchietti, "Energy efficiency in the future internet: a survey of existing approaches and trends in energy-aware fixed network infrastructures," *IEEE Communications Surveys & Tutorials*, vol. 13, pp. 223-244, 2011.
- [10] B. T. Scheme, "LTE: the evolution of mobile broadband," *IEEE Communications Magazine*, p. 45, 2009.
- [11] M. Baker, "From LTE-advanced to the future," *IEEE Communications Magazine*, vol. 50, pp. 116-120, 2012.
- [12] T. Janevski, "5G Mobile Phone Concept," in *IEEE 6th Consumer Communications and Networking Conference (CCNC)*, 2009, pp. 1-2.
- [13] K. R. Santhi, V. K. Srivastava, G. SenthilKumaran, and A. Butare, "Goals of true broad band's wireless next wave (4G-5G)," in *2003-Fall 58th IEEE Conference on Vehicular Technology (VTC)*, 2003, pp. 2317-2321, vol.4.
- [14] Y. Wu, D. Zhang, H. Jiang, and Y. Wu, "A novel spectrum arrangement scheme for femto cell deployment in LTE macro cells," in *IEEE 20th International Symposium on Personal, Indoor and Mobile Radio Communications*, 2009, pp. 6-11.
- [15] P. Pirinen, "Co-channel co-existence study of outdoor macrocell and indoor femtocell users," in *Conference on European Wireless (EW)*, 2010, pp. 207-213.

REFERENCES

- [16] D. López-Pérez, A. Valcarce, G. De La Roche, and J. Zhang, "OFDMA femtocells: a roadmap on interference avoidance," *IEEE Communications Magazine*, vol. 47, pp. 41-48, 2009.
- [17] Y. Tokgoz, F. Meshkati, Y. Zhou, M. Yavuz, and S. Nanda, "Uplink interference management for HSPA+ and 1xEVDO femtocells," in *IEEE Conference on Global Telecommunications (GLOBECOM)*, 2009, pp. 1-7.
- [18] Z. Shi, M. C. Reed, and M. Zhao, "On uplink interference scenarios in two-tier macro and femto co-existing UMTS networks," *EURASIP Journal on Wireless Communications and Networking*, vol. 2010, p. 4, 2010.
- [19] (16 March 2011). *Mobile Broadband Access at Home-ITM, August 2008*. [Online] Available: www.femtoforum.org
- [20] (10 March 2011). *More than 50 billion connected devices*, Ericsson Inc. [Online] Available: <http://www.ericsson.com/res/docs/whitepapers/wp-50-billions.pdf>
- [21] J. Mitola and G. Q. Maguire, Jr. (1999), Cognitive radio: making software radios more personal. *IEEE Personal Communications*, pp. 13-18.
- [22] J. Vankka, *Digital synthesizers and transmitters for software radio*: Springer, 2005.
- [23] F. M. Ghannouchi, "Power amplifier and transmitter architectures for software defined radio systems," *IEEE Circuits and Systems Magazine*, vol. 10, pp. 56-63, 2010.
- [24] R. Schreier, G. C. Temes, and J. Wiley, *Understanding delta-sigma data converters*, vol. 74: IEEE press Piscataway, NJ, 2005.

REFERENCES

- [25] R. V. Nee and R. Prasad, *OFDM for wireless multimedia communications*: Artech House, Inc., 2000.
- [26] S. B. Slimane, "Reducing the Peak-to-Average Power Ratio of OFDM Signals Through Precoding," *IEEE Transactions on Vehicular Technology*, vol. 56, pp. 686-695, 2007.
- [27] T. Jiang and Y. Wu, "An overview: peak-to-average power ratio reduction techniques for OFDM signals," *IEEE Transactions on Broadcasting*, vol. 54, pp. 257-268, 2008.
- [28] P. Lavrador, T. R. Cunha, P. Cabral, and J. C. Pedro., "The linearity-efficiency compromise," *IEEE Microwave Magazine*, pp. 44-58, 2010.
- [29] H. Sjöland, C. Bryant, V. Bassoo, and M. Faulkner, "Switched-mode transmitter architectures," in *Analog Circuit Design*, ed: Springer, 2010, pp. 325-342.
- [30] P. Asbeck, G. Hannington, P. Chen, and L. Larson, "Efficiency and linearity improvement in power amplifiers for wireless communications," in *20th Annual Technical Digest on Gallium Arsenide Integrated Circuit (GaAs IC) Symposium*, 1998, pp. 15-18.
- [31] V. Bassoo, "A digital up-conversion architecture for future high efficiency wireless base stations," Ph.D. dissertation, Victoria University, Australia, 2010.
- [32] V. Bassoo, L. Linton, and M. Faulkner, "Analysis of Non-Uniform Polar Quantisers in a Sigma Delta Transmitter Architecture," *IEEE Transactions on Circuits and Systems I: Regular Papers*, vol. 59, pp. 3060-3070, 2012.
- [33] S. Sirmayanti, V. Bassoo, H. King, and M. Faulkner, "Sigma delta ($\Sigma\Delta$) architecture integration with digital pre-distortion to enhance optimal switch

REFERENCES

- mode power amplification (OSMPA) in FEMTO cell transceiver design," in *IEEE 8th International Conference on Information, Communications and Signal Processing (ICICS)*, Singapore, 2011, pp. 1-4.
- [34] S. Sirmayanti and M. Faulkner, "ΣΔ modulator for digital wireless architecture: A review," in *4th IEEE Makassar International Conference on Electrical Engineering and Informatics (MICEEI)*, 2014, pp. 83-87.
- [35] H. L. Krauss, C. W. Bostian, and F. H. Raab, *Solid state radio engineering*. New York: Wiley, 1980.
- [36] F. H. Raab, P. Asbeck, S. Cripps, P. B. Kenington, Z. B. Popovic, N. Pothecary, *et al.*, "Power amplifiers and transmitters for RF and microwave," *IEEE Transactions on Microwave Theory and Techniques*, vol. 50, pp. 814-826, 2002.
- [37] B. Razavi and R. Behzad, *RF microelectronics*, vol. 1: Prentice Hall New Jersey, 1998.
- [38] V. Paidi, S. Xie, R. Coffie, B. Moran, S. Heikman, S. Keller, *et al.*, "High linearity and high efficiency of class-B power amplifiers in GaN HEMT technology," *IEEE Transactions on Microwave Theory and Techniques*, vol. 51, pp. 643-652, 2003.
- [39] G. A. Rincon-Mora and R. Stair, "A low voltage, rail-to-rail, class AB CMOS amplifier with high drive and low output impedance characteristics," *IEEE Transactions on Circuits and Systems II: Analog and Digital Signal Processing*, vol. 48, pp. 753-761, 2001.
- [40] F. H. Raab, "Efficiency of Doherty RF Power-Amplifier Systems," *IEEE Transactions on Broadcasting*, vol. BC-33, pp. 77-83, 1987.

REFERENCES

- [41] L. R. Kahn, "Single-Sideband Transmission by Envelope Elimination and Restoration," in *Proceedings of the IRE*, vol. 40, pp. 803-806, 1952.
- [42] D. K. Su and W. J. McFarland, "An IC for linearizing RF power amplifiers using envelope elimination and restoration," *IEEE Journal of Solid-State Circuits*, vol. 33, pp. 2252-2258, 1998.
- [43] A. K. Mustafa and M. Faulkner, "Theoretical analysis of hole punch signal conditioning for high efficiency EER power amplifiers," *EURASIP J. Wirel. Commun. Netw.*, vol. 2010, pp. 1-13, 2010.
- [44] S. C. Cripps, *RF Power Amplifiers for Wireless Communications*, Second Edition (Artech House Microwave Library (Hardcover)): Artech House, Inc., 2006.
- [45] B. T. Thiel, S. Dietrich, N. Zimmermann, and R. Negra, "System architecture of an all-digital GHz transmitter using pulse-width/position-modulation for switching-mode PAs," in *Asia Pacific Microwave Conference (APMC)*, 2009, pp. 2340-2343.
- [46] D. A. Calvillo-Cortes, M. Acar, M. P. van der Heijden, M. Apostolidou, L. C. N. De Vreede, D. Leenaerts, *et al.*, "A 65nm CMOS pulse-width-controlled driver with 8Vpp output voltage for switch-mode RF PAs up to 3.6GHz," in *IEEE International Solid-State Circuits Conference Digest of Technical Papers (ISSCC)*, 2011, pp. 58-60.
- [47] F. M. Ghannouchi, S. Hatami, P. Aflaki, M. Helou, and R. Negra, "Accurate power efficiency estimation of GHz wireless delta-sigma transmitters for different classes of switching mode power amplifiers," *IEEE Transactions on Microwave Theory and Techniques*, vol. 58, pp. 2812-2819, 2010.

REFERENCES

- [48] B. Berglund, J. Johansson, and T. Lejon, "High efficiency power amplifiers," *Ericsson Review*, vol. 3, pp. 92-96, 2006.
- [49] M. F. Soltan, "High Efficiency Linear Power Amplifiers: Analysis, Linearization and Implementation," Citeseer, 2004.
- [50] S.-A. El-Hamamsy, "Design of high-efficiency RF class-D power amplifier," *IEEE Transactions on Power Electronics*, vol. 9, pp. 297-308, 1994.
- [51] A.S. Tripathi, et al., U.S. Patent No. 5,777,512 (7 July, 1998).
- [52] W. Heinrich, A. Wentzel, and C. Meliani, "Advanced switch-mode concepts using GaN: The class-S amplifier," in *International 18th Conference on Microwave Radar and Wireless Communications (MIKON)*, 2010, pp. 1-6.
- [53] S. Hori, A. Wentzel, M. Hayakawa, W. Heinrich, and K. Kunihiro, "A Watt-Class Digital Transmitter with a Voltage-Mode Class-S Power Amplifier and an Envelope Delta-Sigma Modulator for 450 MHz Band," in *IEEE Compound Semiconductor Integrated Circuit Symposium (CSICS)*, 2012, pp. 1-4.
- [54] A. Wentzel, S. Hori, M. Hayakawa, K. Kunihiro, and W. Heinrich, "Digital PA with voltage-mode topology using envelope delta-sigma modulation," *International Journal of Microwave and Wireless Technologies*, vol. 5, pp. 285-292, 2013.
- [55] S. Ralph, "Class-S Power Amplifier For Use In Mobile Phone Basestations " M. Eng. & Sci. thesis, Department of Electronic Engineering, National University of Ireland, Maynooth, 2007.
- [56] F. H. Raab, "Idealized operation of the class E tuned power amplifier," *IEEE Transactions on Circuits and Systems*, vol. 24, pp. 725-735, 1977.

REFERENCES

- [57] A. V. Grebennikov and H. Jaeger, "Class E with parallel circuit - a new challenge for high-efficiency RF and microwave power amplifiers," in *IEEE MTT-S International Microwave Symposium Digest*, 2002, pp. 1627-1630, vol.3.
- [58] M. Ozen, R. Jos, C. M. Andersson, M. Acar, and C. Fager, "High-Efficiency RF Pulsewidth Modulation of Class-E Power Amplifiers," *IEEE Transactions on Microwave Theory and Techniques*, vol. 59, pp. 2931-2942, 2011.
- [59] P. Colantonio, F. Giannini, G. Leuzzi, and E. Limiti, "On the class-F power amplifier design," *International Journal of RF and Microwave Computer-Aided Engineering*, vol. 9, pp. 129-149, 1999.
- [60] F. H. Raab, "Maximum efficiency and output of class-F power amplifiers," *IEEE Transactions on Microwave Theory and Techniques*, vol. 49, pp. 1162-1166, 2001.
- [61] M. Helaoui, S. Hatami, R. Negra, and F. M. Ghannouchi, "A novel architecture of delta-sigma modulator enabling all-digital multiband multistandard RF transmitters design," *IEEE Transactions on Circuits and Systems II: Express Briefs*, vol. 55, pp. 1129-1133, 2008.
- [62] C. A. Bouman, "Digital Image Processing," Lecture Notes, 2014.
- [63] I. H. H. Jorgensen, P. Pracny, and E. Bruun, "Hardware-Efficient Implementation of Half-Band IIR Filter for Interpolation and Decimation," *IEEE Transactions on Circuits and Systems II: Express Briefs*, vol. 60, pp. 892-896, 2013.
- [64] L. Jing, W. Xiao-Bo, and Z. Jin-Chen, "An improved area-efficient design method for interpolation filter of Sigma-Delta audio DAC," in *IEEE 10th International*

REFERENCES

- Conference on Solid-State and Integrated Circuit Technology (ICSICT)*, 2010, pp. 327-329.
- [65] L. Chen, Y. Zhao, D. Gao, W. Wen, Z. Wang, X. Zhu, *et al.*, "A decimation filter design and implementation for oversampled sigma delta A/D converters," in *Proceedings IEEE International Workshop on VLSI Design and Video Technology*, 2005, pp. 55-58.
- [66] L. Jing, L. Ran, Y. Ting, H. Zhiliang, and L. Bill Yang, "VLSI implementation of high-speed low power decimation filter for LTE sigma-delta A/D converter application," in *IEEE 9th International Conference on ASIC (ASICON)*, 2011, pp. 453-456.
- [67] N. R. Karnati, L. Kye-Shin, J. Carletta, and R. Veillette, "A power-efficient polyphase sharpened CIC filter for sigma-delta ADCs," in *IEEE 54th International Midwest Symposium on Circuits and Systems (MWSCAS)*, 2011, pp. 1-4.
- [68] E. Martens, A. Bourdoux, A. Couvreur, R. Fasthuber, P. Van Wesemael, G. Van der Plas, *et al.*, "RF-to-Baseband Digitization in 40 nm CMOS With RF Bandpass Delta-Sigma Modulator and Polyphase Decimation Filter," *IEEE Journal of Solid-State Circuits*, vol. 47, pp. 990-1002, 2012.
- [69] S. Abdollahvand, J. Goes, N. Paulino, B. Nowacki, and L. Gomes, "A Polyphase comb filter using interlaying multiplexers for high-speed single-bit Sigma-Delta modulators," in *Proceedings 18th International Conference Mixed Design of Integrated Circuits and Systems (MIXDES)*, 2011, pp. 216-220.

REFERENCES

- [70] T. Johnson and S. Stapleton, "Available load power in a RF class D amplifier with a sigma-delta modulator driver," in *IEEE Conference on Radio and Wireless*, 2004, pp. 439-442.
- [71] T. Johnson and S. P. Stapleton, "RF class-D amplification with bandpass sigma-delta modulator drive signals," *IEEE Transactions on Circuits and Systems I: Regular Papers*, vol. 53, pp. 2507-2520, 2006.
- [72] B. Francois, E. Kaymaksut, and P. Reynaert, "Burst mode operation as an efficiency enhancement technique for RF power amplifiers," in *URSI XXXth General Assembly and Scientific Symposium*, 2011, pp. 1-4.
- [73] S. Chi, P. Singerl, and C. Vogel, "Efficiency optimization for burst-mode multilevel radio frequency transmitters," *IEEE Transactions on circuits and systems-I*, vol. 60, pp. 1901-1914, July 2013.
- [74] K. Hausmair, C. Shuli, P. Singerl, and C. Vogel, "Aliasing-Free Digital Pulse-Width Modulation for Burst-Mode RF Transmitters," *IEEE Transactions on Circuits and Systems I: Regular Papers*, vol. 60, pp. 415-427, 2013.
- [75] P. A. J. Nuyts, B. Francois, W. Dehaene, and P. Reynaert, "A CMOS Burst-Mode Transmitter With Watt-Level RF PA and Flexible Fully-digital Front-End," *IEEE Transactions on Circuits and Systems II: Express Briefs*, vol. 59, pp. 613-617, 2012.
- [76] V. Bassoo and M. Faulkner, "Sigma-delta digital drive signals for switchmode power amplifiers," *Electronics Letters*, vol. 44, pp. 1299-1300, 2008.

REFERENCES

- [77] M. Nielsen and T. Larsen, "A transmitter architecture based on delta-sigma modulation and switch-mode power amplification," *IEEE Transactions on Circuits and Systems II: Express Briefs*, vol. 54, pp. 735-739, 2007.
- [78] S. P. Stapleton, "High efficiency RF power amplifiers using bandpass delta-sigma modulators," *Agilent Technologies, Inc*, pp. 1-22, 2003.
- [79] V. Bassoo, L. Linton, and M. Faulkner, "Analysis of distortion in pulse modulation converters for switching radio frequency power amplifiers," *IET Microwaves, Antennas & Propagation*, vol. 4, pp. 2088-2096, 2010.
- [80] R. Schreier and M. Snelgrove, "Bandpass sigma-delta modulation," *Electronics Letters*, vol. 25, pp. 1560-1561, 1989.
- [81] J. Keyzer, J. Hinrichs, A. Metzger, M. Iwamoto, I. Galton, and P. Asbeck, "Digital generation of RF signals for wireless communications with band-pass delta-sigma modulation," in *IEEE MTT-S International Microwave Symposium Digest*, 2001, pp. 2127-2130.
- [82] C. Jinsung, Y. Jounghyun, Y. Jinho, K. Jinguok, C. Jeonghyun, D. Kang, *et al.*, "A Delta Sigma-Digitized Polar RF Transmitter," *IEEE Transactions on Microwave Theory and Techniques*, vol. 55, pp. 2679-2690, 2007.
- [83] A. Frappe, B. Stefanelli, A. Flament, A. Kaiser, and A. Cathelin, "A digital DS RF signal generator for mobile communication transmitters in 90nm CMOS," in *IEEE Radio Frequency Integrated Circuits Symposium (RFIC)*, 2008, pp. 13-16.
- [84] A. Frappé, A. Flament, B. Stefanelli, A. Kaiser, and A. Cathelin, "An all-digital RF signal generator using high-speed modulators," *IEEE Journal of Solid-State Circuits*, vol. 44, pp. 2722-2732, 2009.

REFERENCES

- [85] V. K. Parikh, P. T. Balsara, and O. E. Eliezer, "All digital-quadrature-modulator based wideband wireless transmitters," *IEEE Transactions on Circuits and Systems I: Regular Papers*, vol. 56, pp. 2487-2497, 2009.
- [86] J. Keyzer, R. Uang, Y. Sugiyama, M. Iwamoto, I. Galton, and P. Asbeck, "Generation of RF pulsewidth modulated microwave signals using delta-sigma modulation," in *IEEE MTT-S International Microwave Symposium Digest*, 2002, pp. 397-400.
- [87] V. Bassoo, A. Mustafa, and M. Faulkner, "Distortion arising from polar to PWM/PPM conversion in an all digital upconverter for switching rf power amplifier," in *IEEE MTT-S International Microwave Symposium Digest*, 2009, pp. 1533-1536.
- [88] Y. Wang, "An improved Kahn transmitter architecture based on delta-sigma modulation," in *IEEE MTT-S International Microwave Symposium Digest*, 2003, pp. 1327-1330.
- [89] V. Bassoo, K. Tom, A. Mustafa, E. Cijvat, H. Sjoland, and M. Faulkner, "A Potential Transmitter Architecture for Future Generation Green Wireless Base Station," *EURASIP Journal on Wireless Communications and Networking*, vol. 2009, pp. 821-846, 2009.
- [90] H. Ruotsalainen, H. Arthaber, and G. Magerl, "A new quadrature PWM modulator with tunable center frequency for digital RF transmitters," *IEEE Transactions on Circuits and Systems II: Express Briefs*, vol. 59, pp. 756-760, 2012.

REFERENCES

- [91] H. A. Ruotsalainen, H. Arthaber, and G. Magerl, "Quantization noise cancelation scheme for digital quadrature RF pulse encoding," in *IEEE MTT-S International Microwave Symposium Digest*, 2013, pp. 1-4.
- [92] S. Sirmayanti, V. Bassoo, H. King, and M. Faulkner, "Odd-even quantisation and cartesian delta-sigma ($\Delta\Sigma$) Upconverters for Transmitter Design," in *IEEE International Conference on Communication Systems (ICCS)*, 2012, pp. 100-104.
- [93] S. Sirmayanti, V. Bassoo, H. King, and M. Faulkner, "OFDM performance with odd-even quantisation in Cartesian $\Delta\Sigma$ upconverters," in *6th Inter. Conference on Signal Processing and Communication Systems (ICSPCS)*, 2012, pp. 1-5.
- [94] S. Sirmayanti, V. Bassoo, and M. Faulkner, "Joint odd-even quantisation in cartesian delta-sigma (DS) upconverters," in *2013 AFRICON*, 2013, pp. 1-4.
- [95] R. Andraka, "A survey of CORDIC algorithms for FPGA based computers," in *proceedings of the 1998 ACM/SIGDA 6th international symposium on Field programmable gate arrays*, 1998, pp. 191-200.
- [96] S. Sirmayanti, V. Bassoo, H. King, and M. Faulkner, "Baseband tuning of Cartesian delta-sigma RF upconverters," *Electronics Letters*, vol. 50, pp. 635-637, 2014.
- [97] A. Corp. (Jan. 10, 2014). *Stratix V FPGAs: Built for Bandwidth*. [Online] Available:<http://www.altera.com/devices/fpga/stratix-fpgas/stratix-v/stxv-index.jsp>
- [98] E. C. Ifeachor and B. W. Jervis, *Digital signal processing: a practical approach*: Prentice Hall, 2002.